PERFORATED DIODE NEUTRON SENSORS

by

WALTER J. MCNEIL

B.S., Kansas State University, 2004

AN ABSTRACT OF A DISSERTATION

submitted in partial fulfillment of the
requirements for the degree

DOCTOR OF PHILOSOPHY

Department of Mechanical and Nuclear Engineering
College of Engineering

KANSAS STATE UNIVERSITY
Manhattan, Kansas
2010

Abstract

A novel design of neutron sensor was investigated and developed. The perforated, or micro-structured, diode neutron sensor is a concept that has the potential to enhance neutron sensitivity of a common solid-state sensor configuration. The common thin-film coated diode neutron sensor is the only semiconductor-based neutron sensor that has proven feasible for commercial use. However, the thin-film coating restricts neutron counting efficiency and severely limits the usefulness of the sensor. This research has shown that the perforated design, when properly implemented, can increase the neutron counting efficiency by greater than a factor of 4. Methods developed in this work enable detectors to be fabricated to meet needs such as miniaturization, portability, ruggedness, and adaptability. The new detectors may be used for unique applications such as neutron imaging or the search for special nuclear materials.

The research and developments described in the work include the successful fabrication of variant perforated diode neutron detector designs, general explanations of fundamental radiation detector design (with added focus on neutron detection and compactness), as well as descriptive theory and sensor design modeling useful in predicting performance of these unique solid-state radiation sensors. Several aspects in design, fabrication, and operational performance have been considered and tested including neutron counting efficiency, gamma-ray response, perforation shapes and depths, and silicon processing variations. Finally, the successfully proven technology was applied to a 1-dimensional neutron sensor array system.

PERFORATED DIODE NEUTRON SENSORS

by

Walter J. McNeil

B.S., Kansas State University, 2004

A DISSERTATION

submitted in partial fulfillment of the
requirements for the degree

DOCTOR OF PHILOSOPHY

Department of Mechanical and Nuclear Engineering
College of Engineering

KANSAS STATE UNIVERSITY
Manhattan, Kansas
2010

Approved by:

Major Professor
Douglas McGregor

Copyright

Abstract

A novel design of neutron sensor was investigated and developed. The perforated, or micro-structured, diode neutron sensor is a concept that has the potential to enhance neutron sensitivity of a common solid-state sensor configuration. The common thin-film coated diode neutron sensor is the only semiconductor-based neutron sensor that has proven feasible for commercial use. However, the thin-film coating restricts neutron counting efficiency and severely limits the usefulness of the sensor. This research has shown that the perforated design, when properly implemented, can increase the neutron counting efficiency by greater than a factor of 4. Methods developed in this work enable detectors to be fabricated to meet needs such as miniaturization, portability, ruggedness, and adaptability. The new detectors may be used for unique applications such as neutron imaging or the search for special nuclear materials.

The research and developments described in the work include the successful fabrication of variant perforated diode neutron detector designs, general explanations of fundamental radiation detector design (with added focus on neutron detection and compactness), as well as descriptive theory and sensor design modeling useful in predicting performance of these unique solid-state radiation sensors. Several aspects in design, fabrication, and operational performance have been considered and tested including neutron counting efficiency, gamma-ray response, perforation shapes and depths, and silicon processing variations. Finally, the successfully proven technology was applied to a 1-dimensional neutron sensor array system.

Table of Contents

List of Figures

List of Tables

Acknowledgements

I thank and recognize all of the individuals and organizations that offered support to this research effort, but more importantly to my professional development. In funding research it is difficult to predict which proposal is a winning concept. It requires patient people with an open mind to the ideas of the funding seekers. I give thanks to the folks at the Defense Threat Reduction Agency and the National Science Foundation, particularly those involved with contract DTRA-01-03-C-0051 and the NSF IMR-MIP grant, 2004, for accepting the honest and realistic concepts proposed by our group at the Semiconductor Materials and Radiological Technology (SMART) Laboratory without the need for outlandish ideas or exaggerated figures to gain attention in this competitive process.

The successes in this research came with much hard work and a commitment of time that most individuals would fear to attempt, and rightly so. To my closest family I acknowledge and thank for sharing my goals and accepting the priorities that I have set to try to achieve vastly more than others my age. Also, I thank them for respecting the lifestyle that I have chosen and enduring the hardships that it has projected onto them. You are the reason that I have come so far and without your encouragement I would have taken on far lesser challenges. To my extended family and those individuals that are still willing to call me a friend, I thank for their commitment despite my lack of presence.

Dedication

I dedicate this work to my parents Mark and Kathy McNeil as well as my loving wife Lisa.

Chapter 1

Introduction

Applications for radiation detection continue to demand smaller and more rugged sensors in both γ-ray (gamma-ray) and neutron detection. The neutron detection problem includes a lack of materials that may readily absorb neutrons and produce an effective observable signal. Perhaps the most common and useful neutron sensor design to this date has been the ^{3}He proportional counter. The simple design, composed of a gas chamber with a small diameter wire anode, has been implemented in nearly all branches of neutron detection applications. The scale of ^{3}He detector instruments ranges from large arrays covering many square meters at neutron scattering facilities down to hand-held units that utilize a single gas tube smaller than one's finger. Smaller, portable, detector systems are in very high demand today in the areas of national security and safety, and these systems have become a popular topic in the radiation detection community.

Gas-filled sensors prove useful in portable applications, but fall short in the property of ruggedness. They are typically sensitive to mechanical shock and their sensitivity to neutrons diminishes substantially as their size decreases. Also, the high voltage (usually over 1000 V) required to operate this type of sensor provides added challenges for the electronic designer tasked with reducing the size of the instrument. In addition to barely meeting the needs of a small portable instrument, there is a greater problem with the use of ^{3}He. Recently it has been realized in industry that the demand for neutron detectors has grown beyond the capacity to supply this rare gas. The limitation is not industrial production

capacity, but rather the abundance of the isotope throughout this planet. Rationing of ^{3}He by governing organizations has already begun, [1]. As a result, alternatives to ^{3}He neutron sensors are being researched aggressively.

Solid state devices show promise in rugged and miniaturized detection systems. Utilizing solid materials to absorb neutrons instead of a gas, smaller devices can be made while retaining good detection efficiency. Solid state sensors have proved successful for decades in detecting γ-ray and charged-particle radiation at room temperature. Unfortunately, a semiconductor material possessing properties to detect neutrons efficiently at room temperature has not yet been discovered. Many semiconductor materials possess the beneficial electronic characteristics for radiation detection. However, none contain isotopes having large neutron absorption cross sections.

An alternative solution to neutron absorbing semiconductor material exists. A high quality semiconductor device can be mated to another material that strongly absorbs neutrons. This type of device is commonly in the form of a thin-film coated semiconductor diode. The diode structure, when operated under reverse bias, allows for the use of common semiconductor materials, such as silicon, by reducing current and noise at room temperature. Such an arrangement establishes a sensor possessing the benefits of a solid-state electronic device, including low voltage operation, compact size, ruggedness and reliability. There are also beneficial parallels with the VLSI industry, such as reliable production in mass quantities and well-established fabrication processes.

As early as 1959, thin films of neutron absorbing material were applied to diode semiconductor devices to sense neutrons [2]. The thin neutron sensitive film converts neutrons into radiation that can be readily detected by the diode. The most successful implementations include converter materials of ^{10}B and ^{6}LiF, mainly due to the emission of secondary charged particle reaction products.

Conventional thin-film coated diode neutron sensors characteristically have low counting efficiency. Even though materials can be employed with efficient neutron absorption, detec-

tion efficiency is limited to roughly 4.5% [3]. The reactive film coating thickness is limited by reaction product self absorption, in which energy is lost before the reaction products reach the semiconductor diode. Because of low counting efficiency, this type of sensor is unable to compete with existing commercial neutron detection solutions.

With efficiency being one of the few drawbacks to the thin-film coated diode design, there have been efforts to break through the efficiency limit of the design by changing the device geometry. A change of surface morphology consisting of deep cavities protruding into a diode device allows neutron conversion material to be loaded into the sensing medium. This concept has been mentioned on occasion in the literature [4–7] and was, at least conceptually, believed to achieve greater neutron counting efficiency.

The first operational devices to prove this concept were fabricated by McGregor [8] and demonstrated a small, but definite, improvement in neutron counting efficiency. Further exploration of these microstructured devices is described in this text, including the development of a sensor that demonstrated 21% neutron counting efficiency. Chapter 2 describes the theory of operation and characteristics of thin-film and perforated diode neutron sensors. Chapter 3 describes the fabrication processes developed to produce simple planar diodes and perforated diodes of various forms. This description includes some testing of the quality of the diodes that were fabricated. Chapter 4 shows results in backfilling the microscopic cavities with enriched ^{6}LiF material. Chapter 5 contains results of testing the neutron sensors including response characteristics and counting efficiency. Chapter 6 presents the development and testing of a pixel-array system incorporating the novel perforated neutron sensors in the form of long narrow strips. Finally, chapter 8 concludes the work.

Chapter 2

Perforated Neutron Sensor Theory

Perforated diode neutron sensors operate on a similar principle as thin-film coated diode sensors. The sensor design relies on a solid neutron converter material to capture neutrons and eject charged particle reaction products into a diode sensor. Charged particles are detected through ionization within the depletion region of the diode structure. The conversion process is effective, but thin-film coated diode neutron sensors have limited intrinsic neutron counting efficiency. High counting efficiency is desired in portable survey instruments, as these devices are often used in low radiation fields where a radioactive source is relatively far away.

2.1 Thin-Film Neutron Sensor Efficiency

The operational characteristics of thin-film coated diode sensors have been studied in depth [3]. The intrinsic neutron counting efficiency of the thin-film design can be approximated by considering the probability of neutron absorption in the converter film and the probability of capturing charged particle reaction products in the diode sensor. Intrinsic neutron counting efficiency is defined as the number of neutrons counted by the sensor over the number of neutrons that pass through the sensor.

2.1.1 Neutron Absorption

Consider a monodirectional current of neutrons, such as a collimated beam of intensity I_0, normally incident on a thin-film of neutron absorber. The intensity, I, of the beam is attenuated through the film and is given as

$$I(x) = I_0 e^{-\Sigma_a x}, \tag{2.1}$$

where Σ_a is the macroscopic absorption cross section and x is a direction along the beam path. The fraction of beam absorbed by the film is then described by

$$F(t) = 1 - \frac{I(t)}{I_0} = (1 - e^{-\Sigma_a t}), \tag{2.2}$$

where t is the thickness of the absorbing film. The macroscopic absorption cross-section of ^{6}LiF for thermal neutrons is 57.51 cm^{-1}. The absorption fraction approximates the neutron absorption efficiency of the sensor. The absorption efficiency is then the best efficiency that the sensor could possibly achieve. Obviously, a sensor will not detect more neutrons than it has absorbed.

This basic exponential model assumes an un-collided flux, where only the absorption interactions are considered. In reality a neutron may scatter a number of times before it is absorbed with a final interaction in the film. The un-collided flux is not a bad approximation for neutron sensors at low neutron energies, typically below 10 eV. As long as the absorption cross-section in a material greatly dominates over the other types of interaction cross-sections, attenuation will also be dominated by the absorption.

2.1.2 Charged Particle Capture

Capturing reaction products emitted from the neutron absorber is just as important as absorbing neutrons. Often charged particle capture is overlooked in sensor design and analysis because of the more apparent neutron capture requirement. In most solids, heavy energetic charged particles are stopped within several microns of penetration, allowing efficient capture even within a shallow diode structure beneath the surface of a silicon wafer. However,

the short range of the charged particle reaction products in the solid conversion material becomes a critical part of thin-film sensor performance.

Energy Deposition from Charged Particles

When a particle is captured in a diode device, signal is generated by drifting the charge clouds formed from ionizing the diode material. The penetrating charged particle leaves a track of ionized charge as it deposits energy into the surrounding medium. The density of ionized charged is not linear as a function of penetration distance and is described by the Bragg ionization distribution. A software routine named SRIM (an acronym for the stopping and range of ions in matter) was used to simulate the average ionization per unit distance of the charged particle reaction products of ^{6}Li within silicon material, Fig. 2.1.

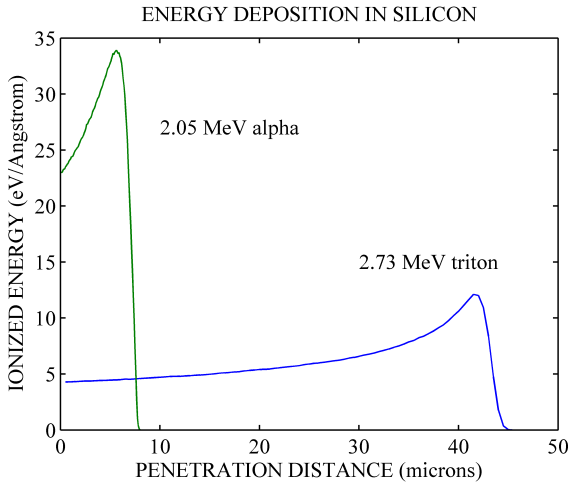

Figure 2.1: *Ionization in silicon of a 2.05 MeV alpha particle and a 2.73 MeV triton, simulated with SRIM.*

A neutron absorption reaction with ^{6}Li produces a 2.05 MeV alpha particle and a 2.73 MeV triton. In silicon the alpha particle looses all of its energy within a range of 9 microns while the triton range is nearly 45 microns. The shape of the ionization curve and the total range of the particles indicate how large a sensitive volume is necessary to capture the full energy of the particle and also the partial energy deposited when only capturing part of the particle track.

Charged Particle Capture Probability

In the thin-film coated diode design, a conversion film is deposited directly against a planar diode structure. Thus, charged particle reaction products born in the conversion film must escape the conversion material to enter the sensor material to produce an electrical signal. Greater energy captured in the sensor produces larger signal, which is advantageous for noise and background radiation discrimination. Low neutron counting efficiency of thin-film coated neutron sensors is primarily a consequence of inefficient particle capture. Conversion films must be made thin to allow charged particle reaction products to escape into the sensor. The reduced converter thickness then inhibits capturing a significant fraction of neutrons passing through.

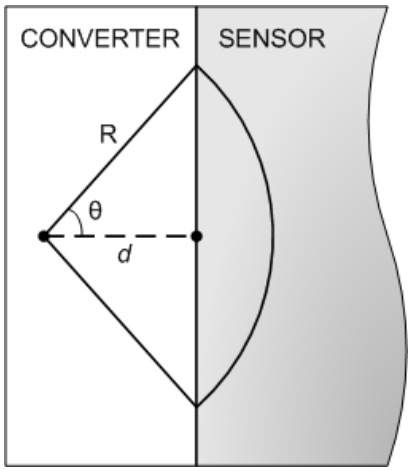

Figure 2.2: *The angle θ defined to represent a cone in which charged particles born in the converter material will be captured in the silicon sensor.*

The reaction products from thermal neutron interaction in the converter are emitted isotropically with both particles emitted in opposing directions. The probability that a charged particle will cross the interface plane between converter material and sensor material can then be described by a fractional solid angle,

$$\Omega_F = \frac{1 - \cos\theta}{2} \tag{2.3}$$

where θ is a cone angle formed between the range of the particle, R, just reaching the interface plane and the normal distance, d, to the interface plane from the point of neutron interaction in the conversion film, Fig. 2.2.

The fractional solid angle, Ω_F, varies from 0.5 to 0 as the distance, d, goes from zero to the range of the particle, R. Thus, neutron interactions farther from the film/detector interface experience a reduced probability of charged particle capture compared to interactions near the film/detector interface. Also, when the distance of neutron interaction from the sensor exceeds the range of the charged particle in the conversion film, the particle can no longer reach the sensor and neutron absorption will not register a signal. In ^{6}LiF material the range of the charged particle reaction products are 6 microns (alpha particle) and 33 microns (triton). With reaction product ranges on the order of microns, the film is too thin to absorb a large fraction of neutrons.

Counting Efficiency

In the referenced work [3], the efficiency of thin-film coated diode sensors is shown to differ for front-side and back-side incident thermal neutrons, due to neutron attenuation toward the particle sensor or away from the sensor, respectively. In the former case the interaction rate of neutrons very near the sensor reduces as film thickness increases. In the latter case where neutrons are attenuated away from the sensor, interaction rate near the sensor remains the same as film thickness increases. The result is an optimum film thickness for efficiency in the front irradiation configuration. The thermal neutron counting efficiency has been calculated as a function of thickness and is given in Fig. 2.3.

The maximum thermal neutron counting efficiency for a ^{6}LiF conversion film on a diode sensor is shown to be just less than 4.5% with the optimum film thickness around 26 microns for front-side irradiation. For back-side irradiation the efficiency may be slightly greater with film thickness at 26 microns and beyond.

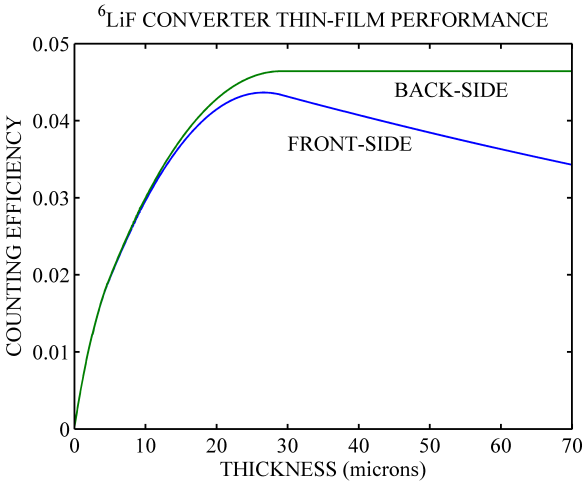

Figure 2.3: *Calculated intrinsic counting efficiency of ^{6}LiF thin-film coated device irradiated from the both the front and back side as a function of film thickness.*

2.1.3 Signal Generation

In diode devices, the signal forming volume is limited to the depletion region where a significant electric field is established. Thus, depth of the depletion volume is important for capturing the ionizing energy of the penetrating charged particle reaction products. Usually, it can be assumed that ionization occurring outside of the depletion region will not contribute significantly to signal due to prompt charge carrier recombination and low electric fields.

If the range of a charged particle reaction product in the sensor material is significantly greater than the depletion region depth, some ionization will occur outside of the active volume and a smaller signal pulse will result, Fig. 2.4. Material availability or the diode structure may limit the depth of depletion. However, applying reverse bias can extend the depletion depth and ensure that the full energy of the particle is captured in the active region of the sensor device, thus improving signal magnitude. The relation for the depletion width in a pn-junction diode is given by,

$$W_{dep} = \left[\frac{2\epsilon}{q}\left(\frac{1}{N_a}+\frac{1}{N_d}\right)(\phi_{bi}-V_a)\right]^{1/2}, \tag{2.4}$$

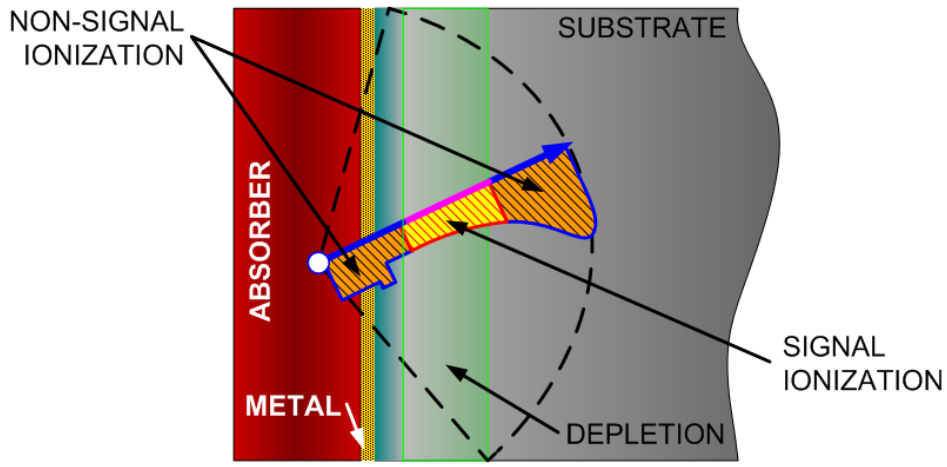

Figure 2.4: *Charged particle ionization contributing to signal (bright yellow) with a small depletion depth.*

where ϕ_{bi} is the built-in voltage of the diode and V_a is the bias applied. N_a is the acceptor concentration on the p-side of the semiconductor and N_d is the donor concentration on the n-side of the semiconductor. q is the charge of an electron and ϵ is the dielectric permittivity of diode material.

For low noise and minimal operating voltage, a self-biased device ($V_a = 0$) is ideal provided that the depletion region is deep enough to completely capture the ionization tracks. In a detection system, a self-biased sensor reduces the amount of supporting circuitry and electronic noise by eliminating the bias supply for the sensor.

Diode particle sensors are often fabricated with a shallow heavily doped side of the junction near the material surface. The other side of the junction is then lightly doped, Fig. 2.5. The heavily doped region is kept shallow in depth to minimize the dead layer that charged particles must cross before entering the depletion region. The lightly doped side of the junction provides a large depletion region necessary to completely capture long charged particle ionization tracks.

This asymmetrical type of diode structure is known as a one-sided abrupt junction, and the difference between impurity concentrations on either side of the junction may be several

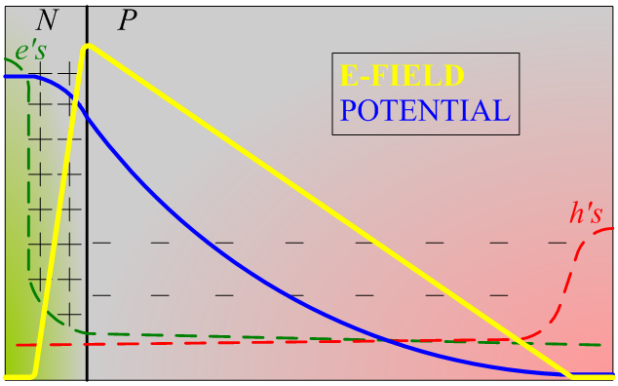

Figure 2.5: *Electric field and potential in a one-sided abrupt pn-junction. A high concentration of n-type impurities exist on the left side of the junction, thereby reducing depletion depth, while a low concentration of p-type impurities allow for a greatly extended depletion region on the right.*

orders of magnitude. Such a large difference in concentration often makes the depth of depletion into the heavily doped side of the junction negligible.

The signal formation process in a thin-film coated diode neutron sensor is depicted in Fig. 2.6. A single pulse will be formed when a neutron is absorbed, thereby, releasing charged particle reaction products, followed by the capture of one of the particles and the drifting of ionized charge through the depletion region.

2.2 Thin-film Sensor Neutron Response

When the conversion film on a coated diode is very thin compared to the range of the reaction products, the probability of capturing either charged particle can approach 100%. In addition, the probability of capturing nearly all of the charged particle energy in the diode is high. The two occurrences together cause the sensor to produce predominantly large signal pulses and few small signal pulses when exposed to a thermal neutron flux. A pulse height spectrum generated from many neutron counts forms a well-defined full energy peak for each particle. A thin-film device spectra was simulated for a ^{6}LiF film roughly half a micron thick and is shown in Fig. 2.7.

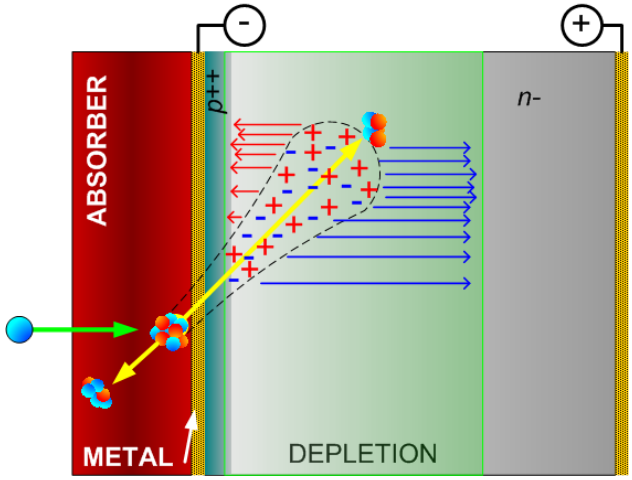

Figure 2.6: *Thin-film sensor operation considering a single neutron absorption, ionization from the captured charged particle, and motion of the mobile charge carriers within the depletion region.*

The distinct spectral features provide a clear representation of particle capture characteristics in the device. On the other hand, a neutron sensor with such a thin film has low neutron counting efficiency. The great charged particle capture probability comes at the expense of low neutron absorption probability. For normal incidence, the absorption efficiency of a 0.5 micron film of ^{6}LiF is only 0.3%, determined from the un-collided attenuation approximation, Section 2.2, and assuming 100% charged particle escape probability.

For best efficiency, the film thickness should be comparible to the range of the long range particle in the conversion material. However, as the film thickness approaches the range of the charged particle, the charged particle capture probability approaches zero away from the interface. Also, shorter lengths of charged particle tracks protruding into the diode deposit less energy per event. The result is a larger quantity of signal pulses formed with less signal magnitude. As the thickness of a conversion film grows toward the optimum thickness of 26 microns, the low energy side of the spectral peaks stretch out toward lower energies. Each spectral peak then transforms into a shelf rather than a peak, resulting in the spectrum of Fig. 2.8.

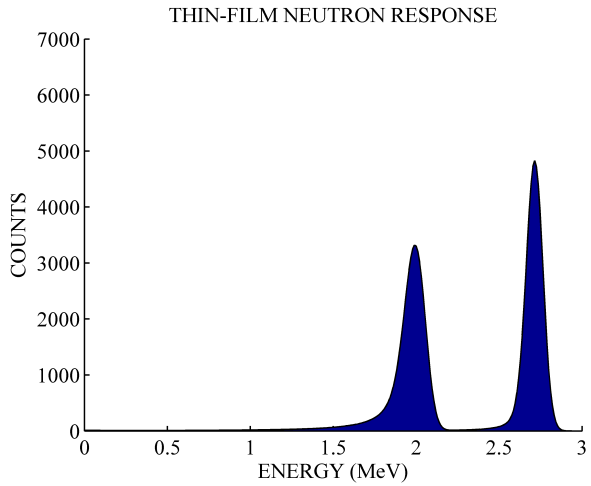

Figure 2.7: *Simulated pulse height spectrum from a 0.5 micron thick conversion film of* ^{6}LiF*. Charge particle reaction products from* ^{6}Li *consist of a 2.05 MeV alpha particle and a 2.73 MeV triton.*

The optimum thermal neutron detection efficiency for a 26 micron thick film device was shown to be 4.5% from Fig. 2.3. The thick film device produces a significant number of low-energy counts in the spectrum. In a practical scenario, a lower level discriminator (LLD) setting will be used to discriminate low level noise and small signal pulses from background radiation. With low energy neutron pulses present in the spectrum, efficiency will suffer with increased LLD, much more so than the thin film spectral response, Fig. 2.7.

2.3 Thin-film Sensor Gamma-ray Discrimination

Utilizing a low-Z sensor material can minimize the probability of a γ ray interaction in the sensor. Silicon is a common diode substrate material and has one of the lowest Z-numbers of the semiconductors. The γ-ray interaction coefficient in silicon is plotted in Fig. 2.9.

Discriminating γ rays with a LLD setting becomes difficult when their signal magnitude approaches that of the charged particle reaction products from neutrons. Neutron signals below the LLD setting are lost and neutron counting efficiency suffers. Signal is formed from γ-ray interactions through ionization from a photo-electron, Compton electron, or

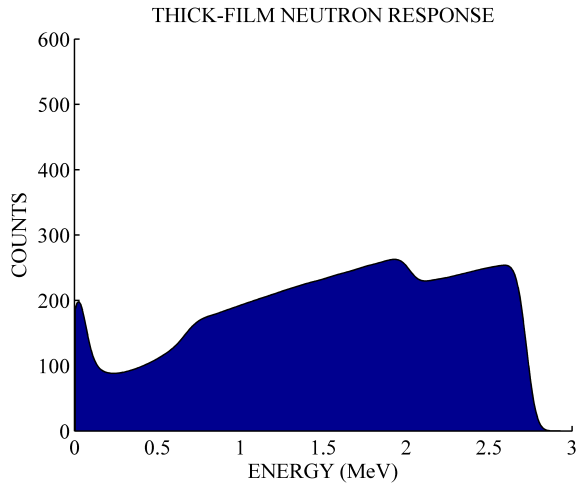

Figure 2.8: *Simulated pulse height spectrum from a 26 micron thick ^6LiF conversion film.*

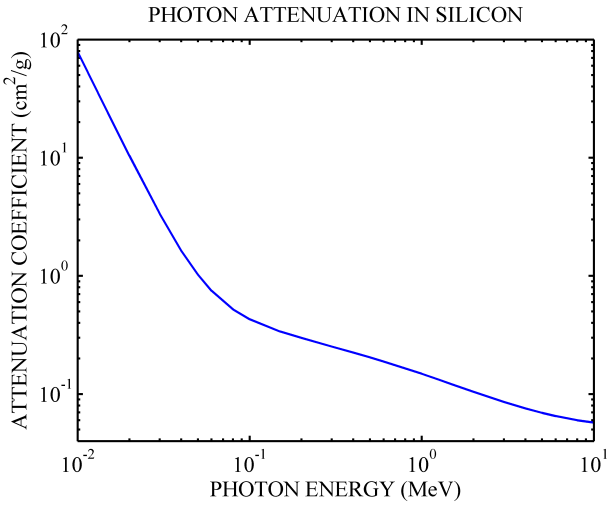

Figure 2.9: *Attenuation coefficient for gamma rays in silicon. The data was gathered from the web resource: http://physics.nist.gov.*

particles from pair production. Energetic electrons have a lower specific ionization and a much greater range in silicon compared to the charged particle reaction products from neutron interactions.

Consider the simulation results of 662 keV electrons in silicon, Fig. 2.10, as calculated with the CASINO software set. CASINO is an acronym derived from the term "monte CArlo SImulation of electroN trajectory in sOlids" and is distributed freely. The simulation

shows the expected trajectory distribution from energetic electrons in silicon material 1.2 mm by 1.2 mm. The energy of 662 keV is characteristic of γ-rays emitted from cesium-137, a common radioisotope.

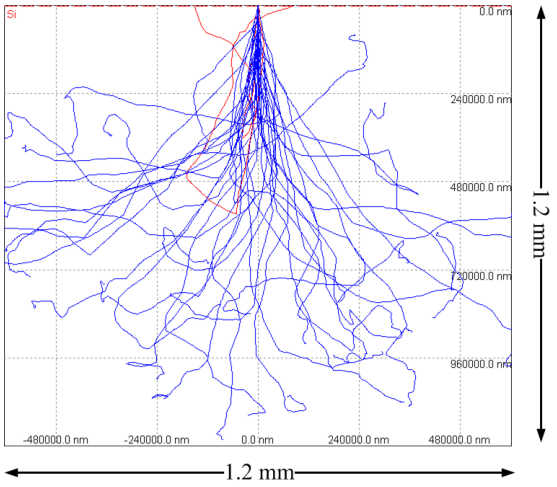

Figure 2.10: *Electron tracks simulated with Casino from 662 keV electrons in silicon material 1.2 mm x 1.2 mm.*

From the simulation it is conceivable, however unlikely, that an electron will be contained within a slab of silicon only 350 microns thick to deposit its full energy. The likelihood is even less for a 50 micron deep depletion region required to capture the total energy of a triton reaction product. The small signal forming volume of the diode depletion region suppresses γ-ray pulses to the lower end of the pulse height spectrum near the noise floor because little energy is deposited by the energetic electrons in the small volume. The repressed magnitude of the pulses allows lower level discrimination to be implemented more effectively.

2.4 Perforated Neutron Detector Efficiency

Introducing deep cavities into a diode and backfilling the trenches with neutron sensitive material can have a profound affect on neutron counting efficiency in comparison to the thin-film coated device. Similar to thin-film analysis, theoretical performance of the perforated neutron sensor can be broken down into categories of neutron absorption, charged particle

capture probability, and signal formation. Each step in the detection process is affected by the physical dimensions of the filled cavities protruding into the semiconductor material.

2.4.1 Neutron Absorption Efficiency

Filling the microscopic trenches with neutron conversion material forms columns of neutron absorber within the diode structure. The space between the trenches allows charge particle reaction products to be captured in the diode sensor to form a signal. For normally incident neutrons the column depth becomes the absorption thickness. To compare neutron absorption between the thin-film design and the perforated design consider a trench 100 microns deep filled with ^{6}LiF material. The optimum neutron counting efficiency of 4.5% is achievable with a ^{6}LiF film 26 microns thick, although absorption efficiency is 14% for that film thickness. If columns of absorbing material can be made 100 micrometers deep, then absorption can be increased to 44% along a column as shown in Fig. 2.11. Similarly, 82% absorption could be achieved along columns with depths of 300 microns.

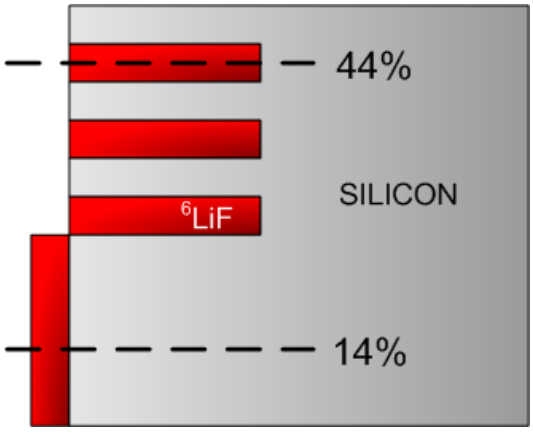

Figure 2.11: *Neutron attenuation in a ^{6}LiF film 26 microns thick and also a trench 100 microns deep.*

With multiple trenches in a sensor, an area coverage factor should be taken into account. Neutrons will not be captured between the columns. With the thin film configuration, 100% of the area is covered with absorber. Long straight trenches having a width of 50 microns

and inter-spaced at 50 microns would have an area coverage of 50%. With an area coverage of 50% and an absorption factor of 44% along the 100 micron deep columns, the neutron absorption efficiency becomes 22%. This perforated geometry then offers more than 1.5 times the absorption efficiency of the optimal thin-film coated diode geometry.

2.4.2 Charged Particle Capture Improvement

In the thin-film coated design, charged particle capture probability reduced significantly when film thickness was increased to improve efficiency. With a perforated structure, charged particle capture probability can be retained with increasing trench depth. Small lateral trench dimensions relative to the charged particle range in the conversion material allow charged particles to be captured between trenches. Neutron absorption and charged particle capture probability are then effectively de-coupled, unlike the thin-film coated case. In the thin-film geometry charge particle capture suffers greatly when film thickness is increased to gain greater neutron absorption efficiency.

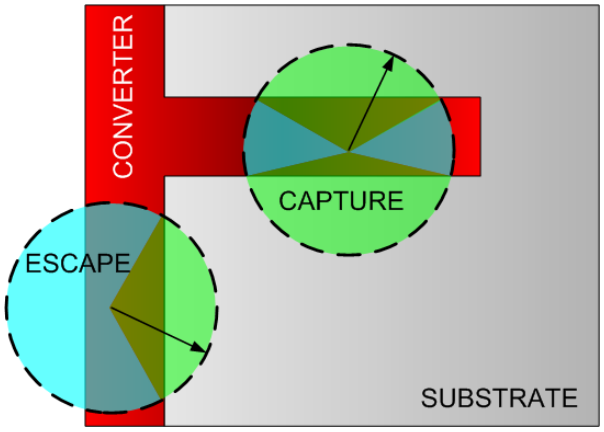

Figure 2.12: *Charged particle capture improvement from a thin-film coating to a deep trench of similar thickness. The green solid angles represent the probability of capturing charged particles emitted isotropically from some location in the conversion material (red).*

In an absorbing column there is a solid angle of escape toward the sides of the column where signal may be formed. A two-dimensional diagram, Fig. 2.12, shows a comparison

between charged particle capture in the thin layer on top of a device compared to a column within the device. The width of the column matches the thickness of the film. In the column two large solid angles of capture into the sensor exist. The thin film geometry has only one significant solid angle toward the sensor. Thus, the perforated geometry offers greater neutron absorption efficiency and greater charged particle capture probability than the thin-film coating geometry.

Computational Analysis of Charged Particle Capture

To quantify the charged particle capture probability in perforated geometries a routine was constructed in MatLab to simulate both neutron absorption in the conversion film and charged particle capture from a round column of ^{6}LiF conversion material 30 microns in diameter and 100 microns deep. The routine is provided in Appendix A. Random values from an exponential distribution were generated through importance sampling along a Z-axis to represent the depth of interaction in the conversion material. Fig. 2.13 shows the result of the interaction depth sampling portion of the routine based on the cross-section of ^{6}LiF. A histogram was produced from a large number of sampled depths to confirm an attenuating type of behavior.

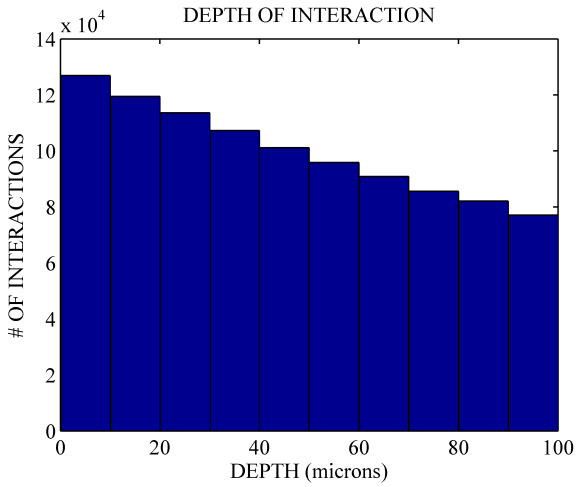

Figure 2.13: *Randomly generated neutron interaction depths in ^{6}LiF sampled from an exponential distribution.*

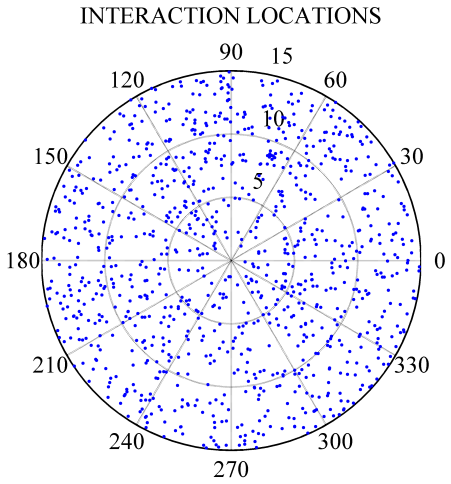

Figure 2.14: *Randomly generated neutron interaction locations in lateral, x and y, dimensions within a circle 30 microns in diameter.*

Interaction location coordinates were generated randomly within the diameter of the round column utilizing a cylindrical coordinate system. A polar angle was sampled randomly from a uniform distribution of angles between 0 and 2π, while the radial position is sampled from a distribution representing the increased differential area of a pie-wedge with increasing radius. This method was confirmed to produce a uniform distribution throughout the circular cross-section of the column. A plot shows the randomized interaction locations in the x-y plane, Fig. 2.14.

The randomized coordinates of polar angle, radial position, and depth, where combined to produce a number of neutron absorption locations in a 3-dimensional space within the cylinder of conversion material. With neutron interaction locations established, the next step is to consider charged particle emission from those locations. Random polar and azimuthal angles were sampled in spherical coordinates from a uniform distribution of π and 2π radians to represent the directional components of a trajectory of one charged particle. The proper behavior in sampling was confirmed with a histogram of the sampled angles shown in Fig. 2.15. With an equal probability of emission in any direction, the randomized values of many angles should be distributed evenly.

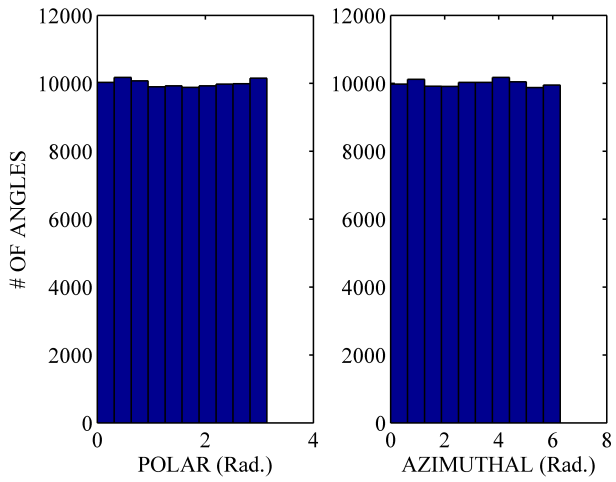

Figure 2.15: *Polar and azimuthal angle sampling.*

A termination point of one of the charged particle reaction products was determined by projecting the particle range in the conversion material along its randomly sampled direction. The same projection was made in the opposite direction using the other reaction product range. The charged particle origin and termination points were then plotted in 3-space with an outline of the column of conversion material, Fig. 2.16.

A count was considered if the termination point of either charged particle had: a z-value greater than zero and a radial value from the center-line of the column greater than the column radius, or a z-value greater than the column depth. The number of counts were divided by the number of neutron interactions to obtain the charged particle capture probability for the geometry.

Another simulation was created to consider the straight trench design 30 microns wide and 100 microns deep. The resulting interaction plot is shown in Fig. 2.17. In the straight trench simulation the coordinate system for interaction locations remained Cartesian. The logical counting routine for this case was the same as the round trench simulation in the z-direction. However in the y-direction, any y-component of particle termination beyond the width of the trench registers a count.

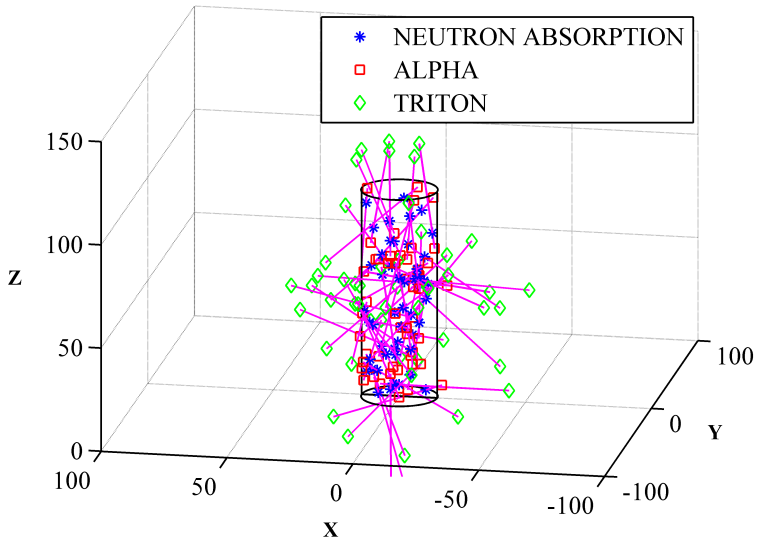

Figure 2.16: *A 3-dimensional map of neutron interactions and charged particle termination points, simulating a circular column of* ^{6}LiF *conversion material 30 microns in diameter and 100 microns deep.*

The straight trench model was easily transferred to a sinusoid geometry by replacing the side-walls of the trench with a sine wave function. The characteristic dimensions of the sine wave in this case were taken from the analysis performed by Solomon [9] in finding an optimal geometry for uniform angular response with perforated diode neutron sensors. With the sinusoid trench design, no longer could the y-component be utilized alone to verify if it was beyond the column dimensions. The y-component in this case had to be greater than the column wall y-component at a similar location in the x-dimension.

To compare the performance between these different trench patterns, simulations were run with a great number of interaction events, or histories. Each simulation was run several times to ensure that statistical variation in the calculated charged particle capture probability was within +/- 0.1%.

To determine counting efficiency, a critical dimension of 30 microns was used to describe the geometry of the trench as well as the spacing between trenches. A square lattice structure was assumed for hole trenches. The product of charged particle capture probability (CPCP),

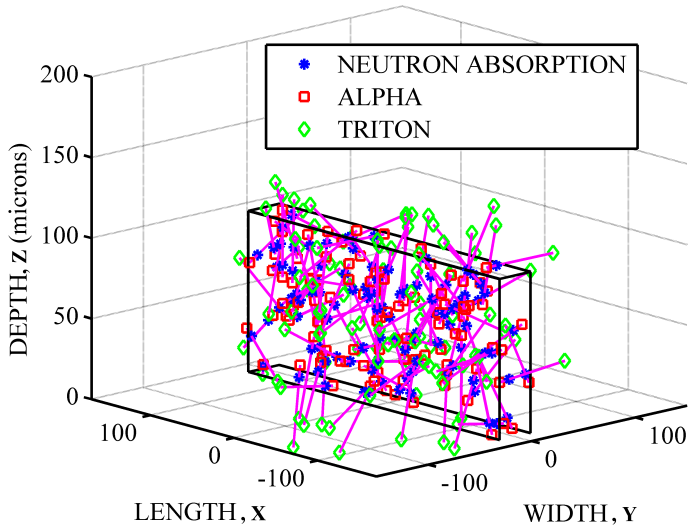

Figure 2.17: *Interaction locations and charged particle destinations with a straight column of* ^{6}*LiF 30 microns wide and 100 microns deep.*

neutron absorption factor, and the area coverage factor gives an approximation of thermal neutron counting efficiency. Simulated efficiencies are tabulated for each of the sensor designs including the optimal thin-film coated sensor design, Table 2.1.

The round column design demonstrates the greatest charged particle escape probability, because escape from the column is probable in all lateral directions. The narrow portions of the sinusoid in addition to the curved regions at its peak and valley result in a slight advantage in charged particle capture over the straight trench. Particle capture probability is directly related to signal magnitude and thus signal-to-noise ratio. Therefore the hole design may be considered more robust by providing the largest signals, despite being less efficient than the other trenched geometries.

In the efficiency approximation it is assumed that signal formation from those charged particles terminating anywhere within the sensor volume is 100%. This approximation may be relatively simple, and ideally, one should include the minimal detectable energy level or the lower level discriminator setting in the calculation. Therefore, values for efficiency

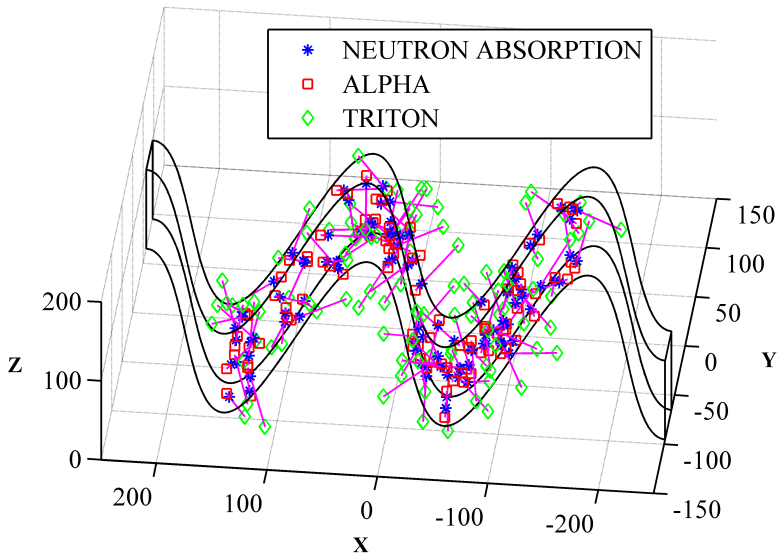

Figure 2.18: *Interaction locations and charged particle destinations with a sinusoid column of* ^{6}*LiF 30 microns wide along the y-direction and a period of 200 microns.*

Design	Abs	Area Cov.	CPCP	Efficiency
Thin-Film	0.139	1.00	0.333	0.046
Hole	0.437	0.20	0.870	0.109
Straight	0.437	0.50	0.656	0.164
Sinusoid	0.437	0.50	0.781	0.195

Table 2.1: *Approximate neutron counting efficiency of various detector geometries including a 26 micron thick film-coating and 100 micron deep trench structures.*

represented here should be considered optimistic. Regardless, the analysis provides an accurate relative performance comparison of the different perforated device designs.

2.4.3 Signal Generation

With a reaction product range in excess of 40 microns in silicon, trench spacing made less than 30 microns may begin to degrade signal generation. The signal generated by a perforated neutron sensor will be characteristic of the device geometry and the design of trenches employed. Trench shape, size, and inter-trench spacing affect the energy captured

from the charged particle reaction products and will also affect the pulse height spectrum output by the sensor.

2.5 Perforated Sensor Neutron Response

The perforated neutron sensor design has been studied in depth by Shultis and McGregor [10–13]. In this work a Monte Carlo type simulation of neutron capture and charged particle transport was executed, including the task of tracking the energy deposition of charged particles within the semiconductor material. A spectral response for straight trench and round hole geometries were considered. Translating the particle energy deposition directly into a pulse height spectrum makes the assumption that electronic signal formation in the sensor after energy is deposited is 100% effective and any amount of ionization in the silicon produces a proportionately representative electronic signal.

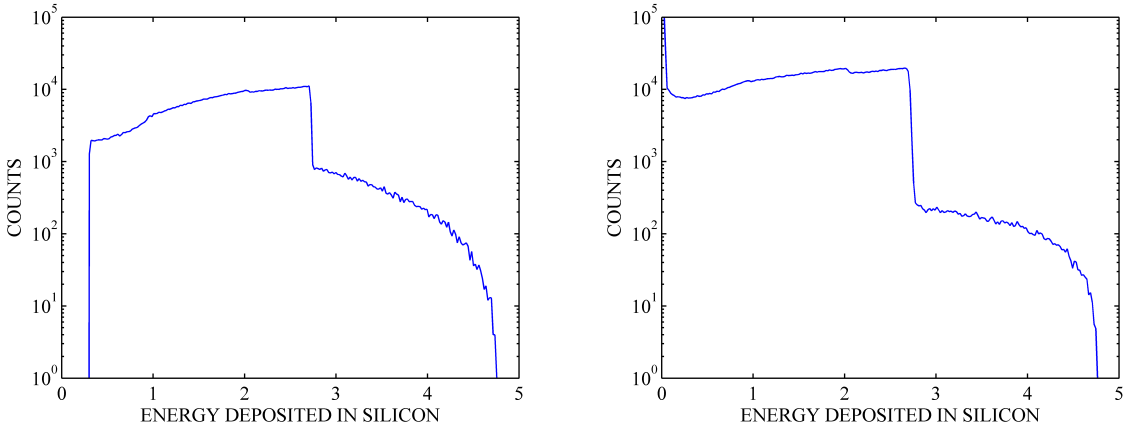

(a) Hole pattern 30 micron diameter on a 60 micron square pitch.

(b) Straight trench Pattern 30 micron wide on a 60 micron pitch.

Figure 2.19: *Theoretical pulse height spectra of 100 micron deep perforated patterns. Courtesy of Prof. Kenneth Shultis (a) and Steven Bellinger (b).*

The response from the hole pattern, Fig. 2.19(a), shows reduced counts at the low end of the spectrum just above the LLD cut-off at 300 keV. Reduced low energy counts are

due to the high probability of charged particle escape from the thin circular columns. A small ridge is present at the alpha particle total deposited energy of 2.05 MeV, and a large sharp cut-off is present at the triton particle total energy of 2.73 MeV. In addition, a tail protrudes toward higher energy that is attributed to the low, but certain, probability of capturing combined energy from both particles simultaneously.

The response for the straight trench pattern, Fig. 2.19(b), is similar to the hole pattern. There is a less pronounced reduction of counts in the low-energy part of the spectrum, due to lower charged particle capture probability. Counts in the lower part of the spectrum are with respect to noise discrimination, however the straight trench design has over twice the neutron absorption due to larger area coverage of the absorber.

2.6 Perforated Sensor Gamma-ray Discrimination

Fig. 2.20 is an overlay of several electron tracks on top of a perforated device structure. The electron tracks were simulated with the CASINO software tool utilizing electrons of 662 keV to simulate the photo-electric absorption of a γ ray from ^{137}Cs. There is a low probability of an energetic electron track being contained within the device. In addition, the trenches in the silicon remove part of the signal forming volume and further repress signal magnitude. Repression of γ-ray pulse magnitude greatly compliments the neutron response of the perforated neutron detector by moving γ-ray pulses to the lower-energy part of the spectrum where neutron counts are reduced.

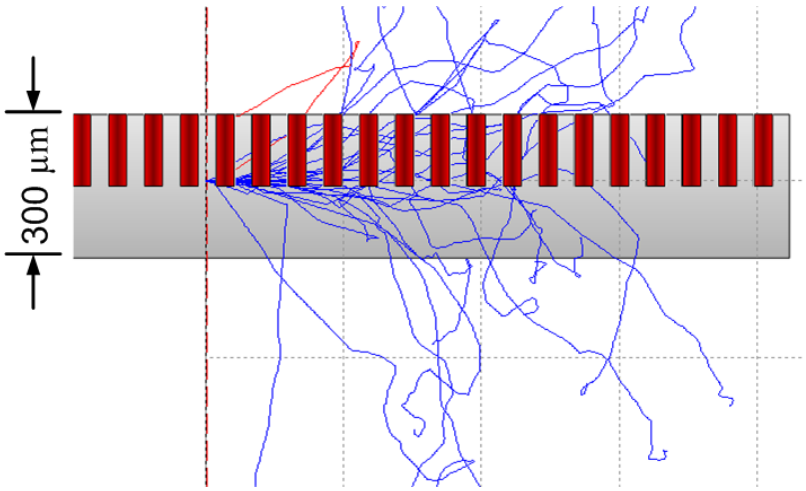

Figure 2.20: *Perforated silicon device with an overlay of 662 keV electron ionization tracks.*

Chapter 3

Perforated Diode Development

Thin-film coated diode neutron sensors were fabricated independently from prior work to set a standard for the exploratory perforated diode fabrication processes. The first part of this chapter describes silicon fabrication processes utilized to produce high quality planar pn-junction diodes. The remainder of the chapter describes the development of processes to construct the perforated diodes. Diode quality was measured by its leakage current characteristics. Performance as particle sensors and neutron sensors are discussed in the following chapters.

3.1 Planar Diode

The diodes constructed and compared in this work were 5.5 mm in diameter with a metal ring around their perimeter. The metal ring is an electrical contact and has a slightly enlarged pad, on which probing and bonding connections were made. The large window within the ring allows charged particle reaction products to pass through without being attenuated by the metal layer. The backside of the device utilizes a monolithic metal contact. On a wafer the diodes are centered 7 mm apart. When diced from the wafer, a 7 mm x 7 mm square device results with a circular active region in the center, Fig. 3.1.

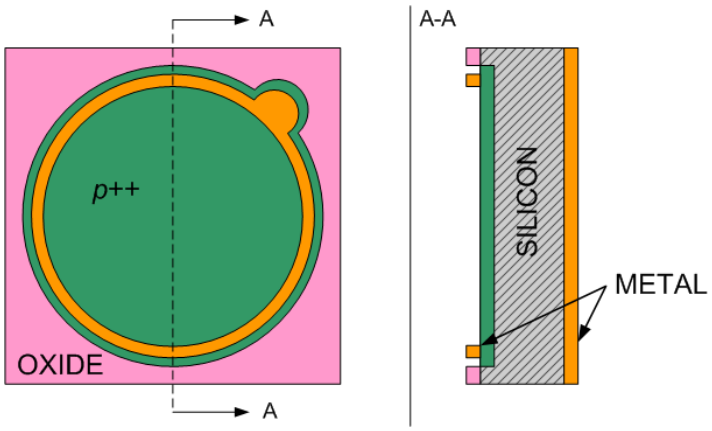

Figure 3.1: *The geometry of the planar diode designed for particle sensing.*

3.1.1 Fabrication Process

Prime grade, double-side polished, n-type silicon wafers of 1-10 kOhm-cm resistivity were selected as substrates for this work. A standard wafer cleaning procedure consisted of the piranha solution followed by the BakerClean^{TM} solution. The piranha is a mixture of hydrogen peroxide and sulfuric acid that is heated and aggressively attacks organic materials.

BakerClean^{TM} is mixed with water and a small amount of hydrogen peroxide and is followed by a quick de-ionized water rinse and an oxide strip in a buffered oxide etch (BOE) solution. The BakerClean^{TM} solution acts similarly to the well known RCA clean [14], providing particulate removal in addition to trace-metal oxidation and removal. The entire cleaning process is listed by step in Table 3.1.

Name	Chemical	Ratio	Temp.	Time
Rinse	H_2O	100%	Room	Any
Piranha	H_2O:H_2SO_4:H_2O_2	1:1:1	90-100 (°C)	10 (min.)
Rinse	H_2O	100%	Room	Any
Bakerclean	H_2O:Baker:H_2O_2	20:5:1	70-80 (°C)	10 (min.)
Rinse	H_2O	100%	Room	Any
BOE	H_2O:HF:NH_4F	18:5:12	Room	10 (sec.)
Rinse	H_2O	100%	Room	Any

Table 3.1: *Wafer cleaning process.*

The chemical cleaning process can be executed with hot-plates and beakers. A preferred method utilizes more advanced systems found in industry including filtered recirculation baths with sonic generators to scrub the wafer surface during processing. The wafer cleaning process in all cases was performed just before the next processing step to avoid wafer contamination while in storage. A wafer spin-rinse-dryer (SRD) was used to dry wafers after cleaning.

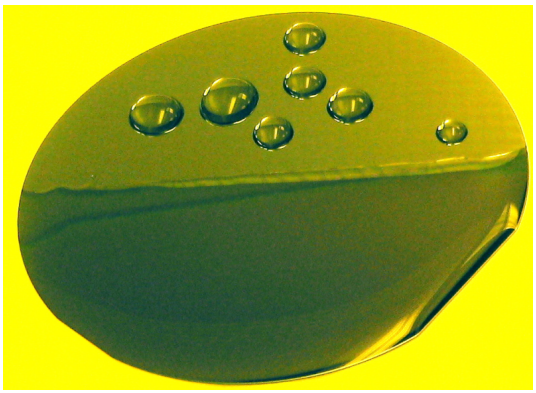

Figure 3.2: *A clean silicon wafer half-coated with a silicon oxide. Water is retained on the oxide surface whereas only large droplets of water remain on the bare silicon surface.*

During the wafer cleaning procedure, BOE steps remove residual oxide films. The hydrophobic nature of silicon indicates when an oxide layer is removed from the surface. Clean silicon dioxide holds water against the wafer surface causing water to slowly sheath away, even when blown with dry nitrogen. Water will bead on bare silicon and falls off the wafer readily, Fig. 3.2.

Oxidation Process

Immediately following the wafer clean, a thermal wet oxidation is executed for 70 minutes at 1100 °C with a water bubbler temperature held at 96 °C. This oxide forms the diffusion mask for a phosphorus diffusion process. To minimize thermal shock, the wafers were held at the mouth of the oxidation furnace for 5 minutes before being pushed into the furnace at roughly 0.5 inches per minute. Before loading the wafers, a gradual temperature gradient

was configured in the furnace that gradually increased to roughly 650 °C mid-way through the furnace, Fig. 3.3.

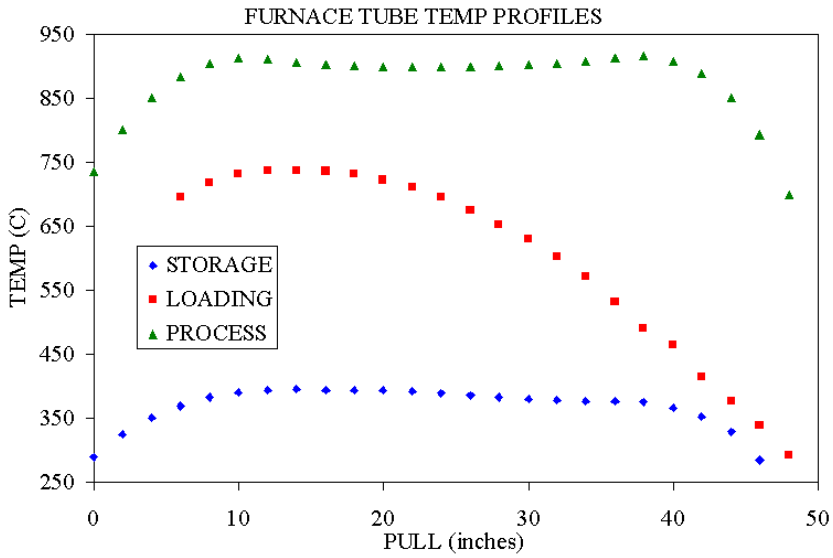

Figure 3.3: *Temperature profiles for various furnace operations. The gradient profile for wafer loading is shown in red.*

With wafers loaded, a uniform thermal profile was set at the process temperature of 1100 °C. Wafers were loaded with dry oxygen flow to inhibit nitride growth and prevent uncontrolled growth from stray moisture in the air. When the furnace temperature stabilized, gas-flow was switched from dry O_2 to wet O_2 by diverting the oxygen through a heated bubbler of de-ionized water. The wet O_2 configuration was held for a duration of 2.5 hours. Afterwards, the gas flow was changed back to dry O_2 and the thermal profile of the furnace was changed to the loading gradient profile. The wafer boat was removed just as it was loaded, except with the reverse order of procedures. The entire furnace process is depicted in Fig. 3.4.

The photoresist used to pattern diffusion windows in the oxide was purchased from AZ Electronic Materials, grade nLof2035. Resist was spun onto the wafer at 5500 rpm and baked at 100 °C in an oven for 30 minutes. Resist was then applied in the same manner to the opposite side of the wafer and baked again for the same duration.

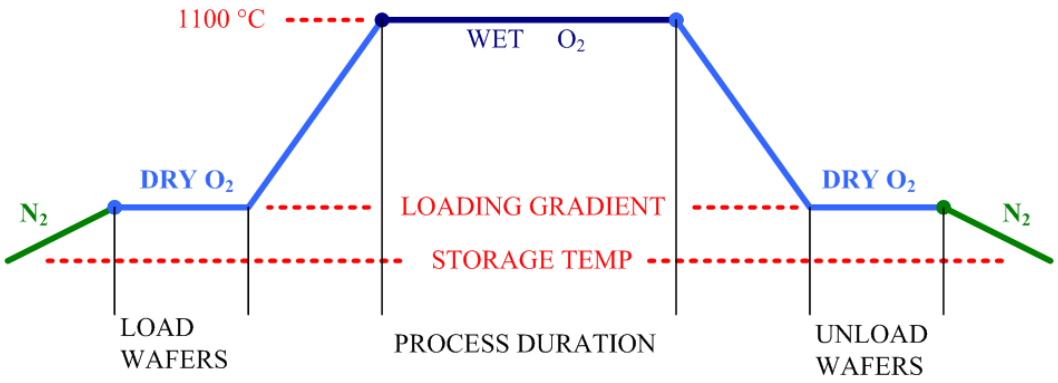

Figure 3.4: *A process diagram for the thermal oxidation procedure.*

The diffusion mask pattern was aligned (centered on the wafer) before exposure in the mask aligner. The wafer was then flipped over and a flood exposure (no pattern) was performed. For each side the exposure time was 3.3 seconds. A second oven bake for 30 minutes took place before the wafer was developed in a solution of MIF300, also purchased from AZ Electronic Materials. Just short of 2 minutes in solution, the pattern appeared on one side of the wafer while the photoresist remained completely covering the other side, Fig. 3.5. Photomasks were designed with the L-Edit software package.

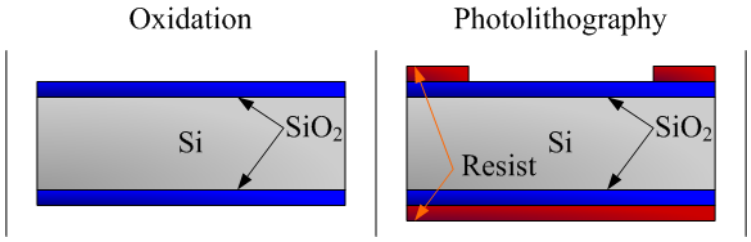

Figure 3.5: *Cross-sectional view of a wafer segment after oxidation (left) and after lithographic patterning (right).*

After patterning diffusion windows in the photoresist a buffered oxide etch (BOE) was executed for 12 minutes to transfer the pattern into the oxide layer, Fig. 3.6. Bare silicon appeared in the pattern and was confirmed to behave as hydrophobic. The photoresist was removed with an AZ Electronic Materials product called Kwik Strip. With the solution at

90 °C, resist was removed in roughly 10 minutes. After stripping resist, hydrophobic action is not observable on the wafer. An invisible residue is left from the stripping solution even after rinsing in propanol and de-ionized water. Only after a wafer clean will the hydrophobic action of bare silicon be observed.

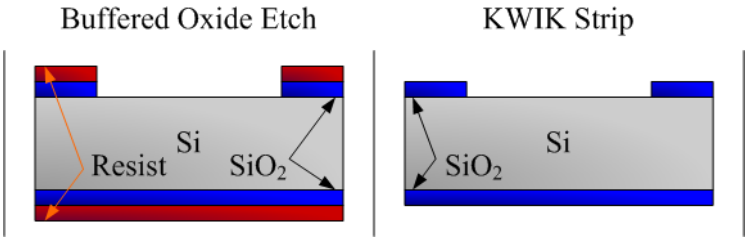

Figure 3.6: *Cross-sectional view of a wafer segment after the buffered oxide etch, BOE, (left) and after the KWIK-strip photoresist removal process (right).*

The standard wafer cleaning process was executed and the hydrophobic behavior of silicon was confirmed. With a pattern in the oxide layer on the wafer, water would initially cling to the entire wafer surface. With a short burst of dry nitrogen, the water would recede quickly from the silicon dots exposed from etching through the oxide layer. Further drying was then necessary to remove the water completely. Immediately after the cleaning process, the wafer was loaded into the phosphorus diffusion furnace. The phosphorus diffusion will establish a thin n-type layer just beneath the exposed silicon surface. With the oxide mask in place, the diffusion layer will only form within the windows of the oxide pattern, Fig. 3.7.

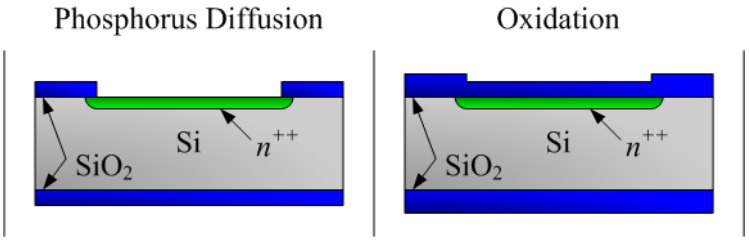

Figure 3.7: *Cross-sectional view of a wafer segment after the n-type phosphorus diffusion (left) and after the second oxidation process (right).*

Phosphorus Doping Process

A phosphorus diffusion was implemented utilizing Saint Gobain Ceramics planar diffusion source products (PDS® products) PH-950 source wafers. Wafers were loaded with the same procedures as in the oxidation process, except with nitrogen gas flowing. After loading the wafers with nitrogen gas-flow, the furnace was brought to a process temperature of 950 °C, where it was held for 2 hours before cooling back down to the temperature profile suited for wafer removal, Fig. 3.8. After diffusion, a thin glass layer resulting from the process was removed from the wafer surface with a buffered oxide etch step for a 2 minute duration. After this "deglaze" step, hydrophobic action could be visually confirmed.

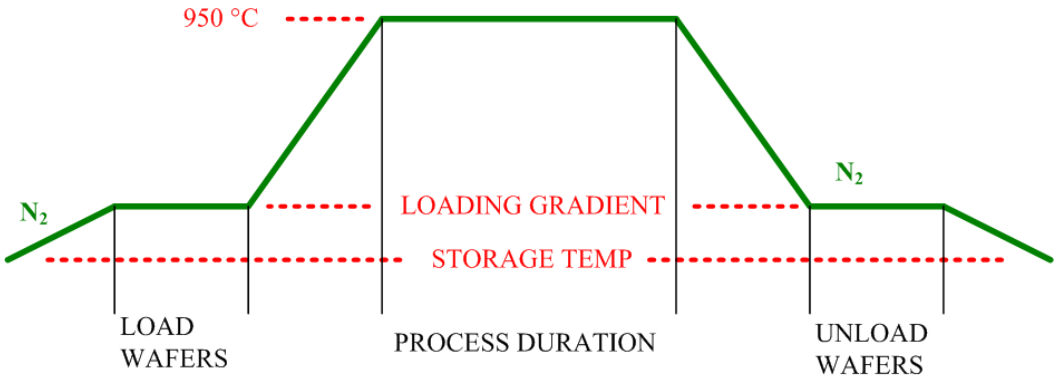

Figure 3.8: *Process flow chart for phosphorus solid-source diffusion.*

A second oxidation was performed after the diffusion process, Fig. 3.7. This oxidation process was carried out exactly as the first oxidation. The same photolithography procedure was also repeated after this oxidation. However, this photolithography step was performed on the opposite side of the wafer in preparation for boron diffusion, Fig. 3.9. This diffusion pattern was aligned to the pattern on the other side of the wafer using an infrared light source and infrared optics installed on the mask aligner. The diffusion windows were etched into the oxide layer and the resist was stripped, just as done previously on the other side of the wafer. After patterning, a third wafer cleaning process was executed to prepare for a boron diffusion process.

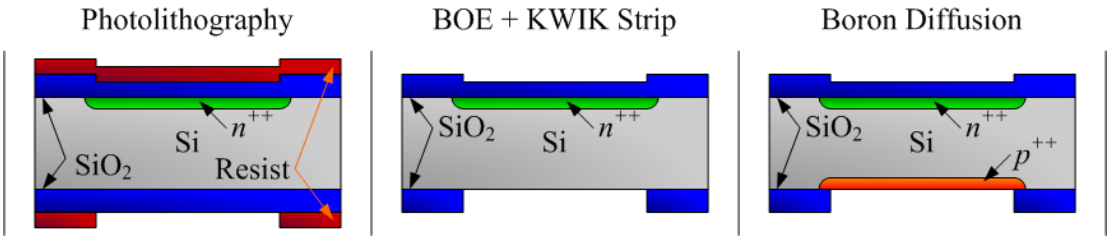

Figure 3.9: *Cross-sectional view of a wafer segment showing lithographic patterning (left), the BOE oxide removal (middle), and the p-type boron diffusion (right).*

Boron Doping Process

Saint Gobain solid-source diffusion wafers, grade BN-975 were used to diffuse boron into the surface of the wafers. The wafer boat was loaded into the furnace as in the oxidation process, but with oxygen and nitrogen flowing. After loading, the temperature was elevated to uniform profile of 800 °C and held for 20 minutes, allowing temperature to stabilize in the furnace tube. Hydrogen gas was then injected for 2 minutes. After hydrogen injection, both hydrogen and oxygen were shut off and the temperature was ramped up to 900 °C. This process temperature was held for 2.5 hours before cooling the furnace to the loading gradient for wafer removal, Fig. 3.10.

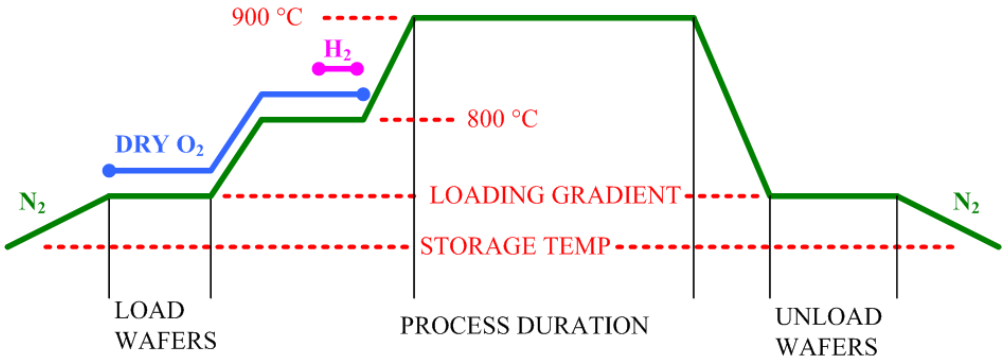

Figure 3.10: *Process flow chart for boron solid-source diffusion.*

As with the phosphorus diffusion process, a buffered oxide etch (BOE) step was performed for two minutes to remove a residual glass film left on the silicon. However, silicon

boride remains on the surface and an oxidation process is required for complete removal. A dry oxygen environment at a temperature of 800 °C for 20 minutes oxidized the boride and allowed the BOE to remove this layer in less than one minute. Hydrophobic behavior was confirmed after this low-temperature oxidation (LTO) process and the quick BOE. The BOE oxide removal was postponed until just before metal deposition so that the silicon remained encapsulated and protected up to that point.

Metal Deposition

Patterning photoresist for metal lift-off, the UV exposure time was reduced to 2 seconds and the develop time was extended to 3.5 minutes to establish undercut in the resist. A quick BOE stripped the thin oxide film left from the LTO process in the previous step. Immediately after, the wafer was loaded into an e-beam evaporator, Fig. 3.11, and placed under vacuum.

Figure 3.11: *Typical evaporation apparatus and geometry. Wafers load into the top of the chamber while the source material rests in a small crucible at the bottom of the chamber.*

The evaporator utilized a cryo-pump to achieve ultra-high vacuum and took a couple of hours to reach a level on the order of 10^{-6} Torr. A barrier layer of titanium was evaporated to a thickness of 400 Angstroms before switching to aluminum. An aluminum film was

evaporated to a thickness of 2000 Angstroms. After 30 minutes with periodic agitation in Kwik strip, the metal layer on top of the resist was released from the wafer. Another similar lift-off process was repeated to establish the metal contacts on the opposite side of the wafer, Fig. 3.12. After the second lift-off, a propanol rinse was the final chemical process for the wafer.

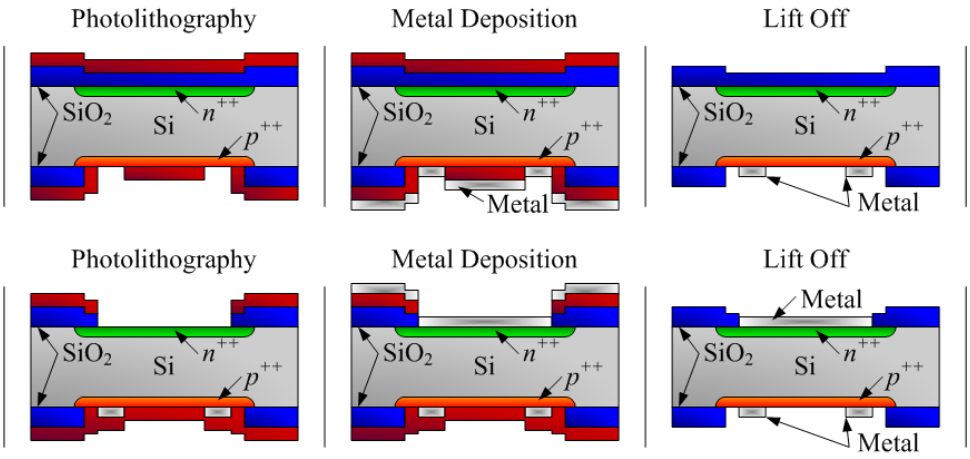

Figure 3.12: *Cross-sectional view of the front-side metal deposition with lift off (top), and the back-side metal deposition with lift off (bottom).*

3.1.2 Leakage Current Test

Diode leakage current was tested with a Keithley voltage/current measurement instrument (model 237). The measurement required a light-tight environment because the large area diodes produced substantial current when exposed to light. Also, to minimize noise in the measurement, a Faraday shield was needed to surround the diode and probing apparatus from electromagnetic interference. A custom testing station was constructed to solve the noise and light problem, Fig. 3.13. Special bends were made at the lid/base interface to ensure a light-tight fit. Adhesive-backed foam was used to make a soft seal on overlapping parts. To assist with electro-magnetic shielding, a conductive connection was made continuously between lid and base by removing all of the paint around the mating edges and then lining the base with a copper mesh sleeve around a foam rubber cord.

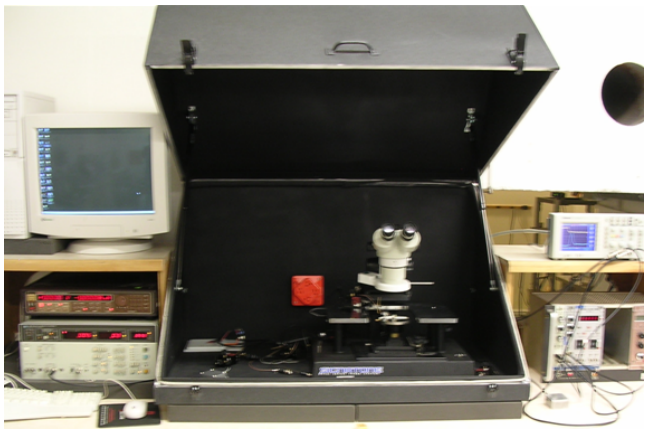

Figure 3.13: *Probe station light-tight Faraday shield box.*

3.1.3 Planar Diode Leakage Current

Voltage was swept across the device from a small forward bias to a significant reverse bias, and current was recorded throughout the range. It is common practice to plot the current as a function of voltage to produce an I-V curve. As a part of validating the planar diode fabrication processes, I-V curves were collected from many diodes on a wafer and plotted together.

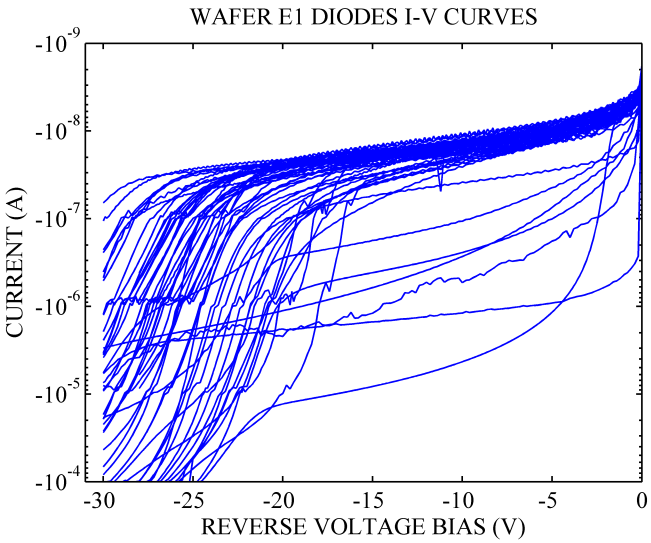

Figure 3.14: *Reverse bias leakage current from a wafer of fabricated planar diodes.*

It can be concluded from the plot, Fig. 3.14, that the fabrication process described in the previous section is a successful recipe for achieving low leakage current in reverse bias. The plot shows the majority of planar diodes demonstrating less than 100 nano-Amps of current beyond 10 volts of reverse bias. A few diodes do not follow the trend and show much greater leakage current. Some diodes, uncharacteristic of the average, had leakage current exceeding one micro-amp at 10 volts of reverse bias. A break-down mechanism is apparent by a sharp bend in the curves, where current increases more readily with greater reverse bias. There is great variability in the break-down of these diodes. Some diodes broke down as low as -16 volts where others broke down beyond -25 volts. Commonly, diode operation as a particle sensor requires less than 10 volts of reverse bias.

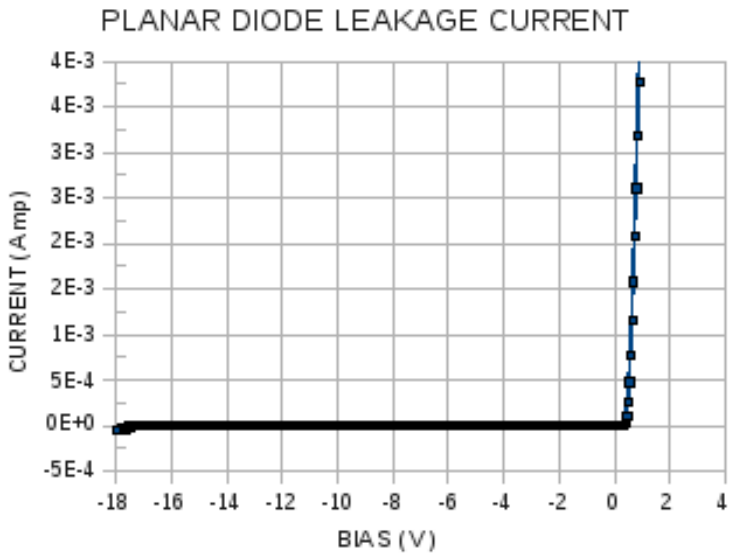

Figure 3.15: *Broad scale I-V curve of a typical planar diode fabricated as described in the previous section.*

Diode leakage current was shown to be repeatedly less than 100 nano-amps, but this does not confirm the rectifying behavior one expects from a diode device. With a full bias sweep including forward bias and reverse bias, current rectification can be revealed. One of the diodes from the previous plot was re-plotted on a broad linear scale to demonstrate the

extreme difference in forward and reverse bias behavior, Fig. 3.15. With less than 1 volt of forward bias, significant current flows through the diode. Alternatively, with reverse bias the diode current is rectified and exhibits orders of magnitude less current flow. Current remains very low with increasing reverse bias until some form of break-down begins to occur, in this case at -17 volts.

3.1.4 Streamlined Fabrication Process

The amount of work involved to execute the entire planar diode fabrication process was substantial. A single furnace process took the majority of a work day. Fabricating a few wafers of diodes took a minimal commitment of two weeks. A table of process steps (Table 3.1.4) shows the daily schedule of process flow. Also, discovering any defects in photolithography meant that a strip and rework was necessary. Reworking photolithography steps was commonplace to ensure a good product yield.

The time that it took to fabricate diodes was difficult to manage. It became clear that the research effort would benefit greatly if the fabrication process could be shortened. Thus, methods for saving time in processing were investigated. Considering the diode design and processing steps, there were many aspects that could be removed or combined to compress the fabrication schedule.

Day	Procedures
1	Wafer clean + Oxidation mask
2	Photolith diffusion mask + Window etch
3	Wafer clean + Phosphorus diffusion
4	Wafer clean + Oxidation mask
5	Photolith diffusion mask + Window etch
6	Wafer clean + Boron diffusion + LTO
7	Photolith lift-off mask
8	Evaporate contacts + Lift-off
9	Photolith lift-off mask
10	Evaporate contacts + Lift-off

Table 3.2: *Planar diode fabrication process flow.*

The phosphorus diffusion on the backside of the wafer was eliminated from the process. The only negative result of this change was a reduction of forward bias current. The metal/semiconductor interface on the back-side of the device without the heavily doped n-type layer became a Schottky contact, but did not interfere with the pn-junction on the other side of the wafer. The Schottky contact on the back-side enters a rectifying state only when the pn-junction diode was in the forward bias condition. The forward bias condition is not used for particle detection.

Another time-saving alteration came from performing both metal lift-off processes together. The photoresist patterns were developed on both sides of the wafer in the same photo-lithographic step. Here, two alignments were performed after the resist was applied to both sides of the wafer. Afterwards, an evaporation was executed on each side of the wafer consecutively.

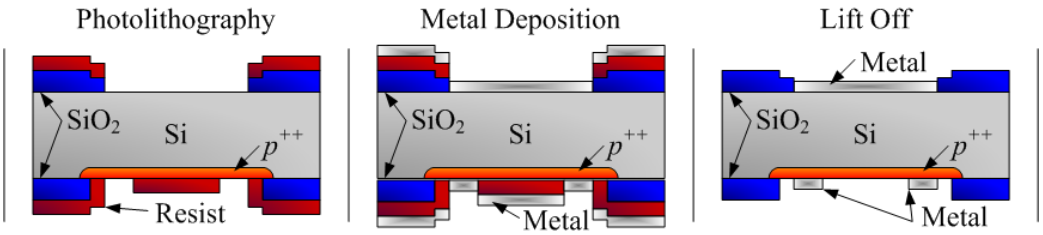

Figure 3.16: *Cross-sectional view of a double-side resist pattern (left), double-sided metal deposition (middle), and lift off (right).*

With the two major processing changes, the fabrication schedule was improved drastically. The modified process flow, Table 3.1.4, shows only five days of processing. The processing schedule was cut in half and productivity was increased in other areas of the research effort.

3.2 Perforated Diode: Piercing Design

The metal ring electrode in the diode design provides direct access to the diode such that energetic charged particles do not attenuate through metal layers. This window also makes

Day	Procedures
1	Wafer clean + Oxidation mask
2	Photolith diffusion mask + Window etch
3	Wafer clean + Boron diffusion + LTO
4	Photolith double-side lift-off mask
5	Evaporate + Evaporate + Lift-off

Table 3.3: *Modified planar diode fabrication process.*

the silicon surface accessible for trenches to be etched without having to etch through the metal contact. Without risking damage to the diode contact, the diode could be tested before and after a trench etching process was executed.

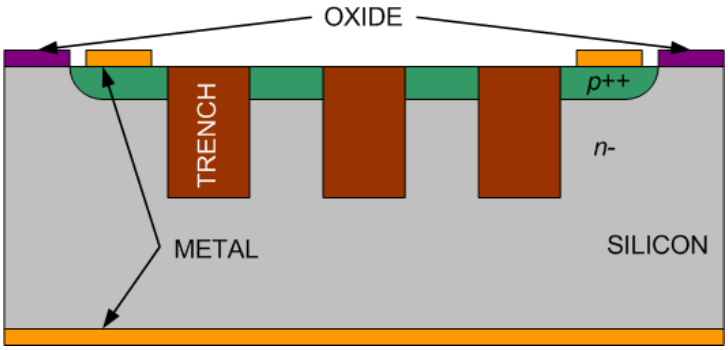

Figure 3.17: *Piercing trench design of a perforated diode.*

Etching deep holes into the diode surface causes trenches to pierce through the shallow p-type diffusion layer while extending deep into the depletion region. This "piercing" structure is depicted in Fig. 3.17. A photolithographic technique was developed specifically for the plasma etching process used to form high aspect ratio trenches in the silicon. Much work was involved to insure that the side-walls of the photoresist patterns were vertical and straight. Tapering resist sidewalls result in unwanted side-wall roughness in the trenches.

A reliable etching process was developed by Blake Rice [15] that produced smooth-walled, 30 micron deep holes, also 30 microns in diameter, utilizing an Oxford Instruments Plasmalab 100 system, Fig. 3.18. The plasma etching process involved cycling between SF_6 and C_4F_8 process gasses to both etch and deposit material, respectively. The chamber

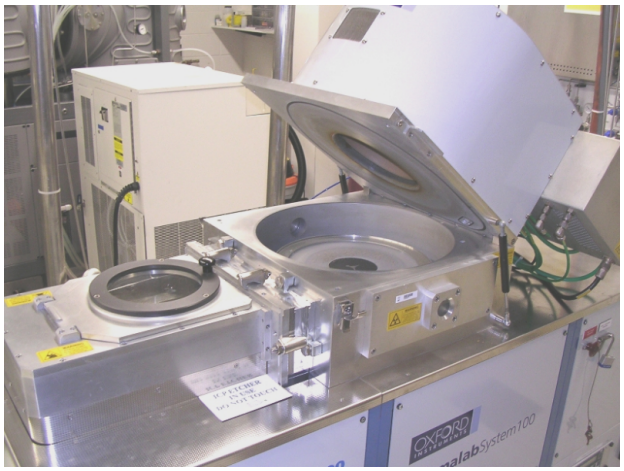

Figure 3.18: *The ICP-RIE plasma etching system used in forming the microstructured trenches in this work.*

pressure was held at 30 milliTorr while the wafer was held at 10 °C and helium backing pressure was held at 10 milliTorr. The etching configuration was executed with 900 Watts of ICP power, 35 Watts of RF power, and 80 sccm of gas-flow for 15 seconds per cycle. Meanwhile, the deposition configuration was executed with 800 Watts of ICP power, 15 Watts of RF power, and 60 sccm of gas-flow for 8 seconds per cycle. The process duration lasted over 1 hour to achieve 30 micron deep holes. Once complete, the photoresist mask was removed and leakage current was tested.

3.2.1 Leakage Current

The leakage current observed with the etched diodes changed substantially from the original planar configuration. The leakage before etching was around 30 nanoamps at a reverse bias of 10 volts, representative of a typical planar diode. On the other hand, with roughly 5000 holes etched into the surface of the diode, leakage current increased to around 9 microamps. The leakage current curves are shown in Fig. 3.19.

At nearly 10 microamps, the leakage current was too great for reliable operation as a radiation sensor. The leakage current in this case was desired to be less than 1 microamp to maintain acceptably low electronic noise. The etching process caused physical damage to

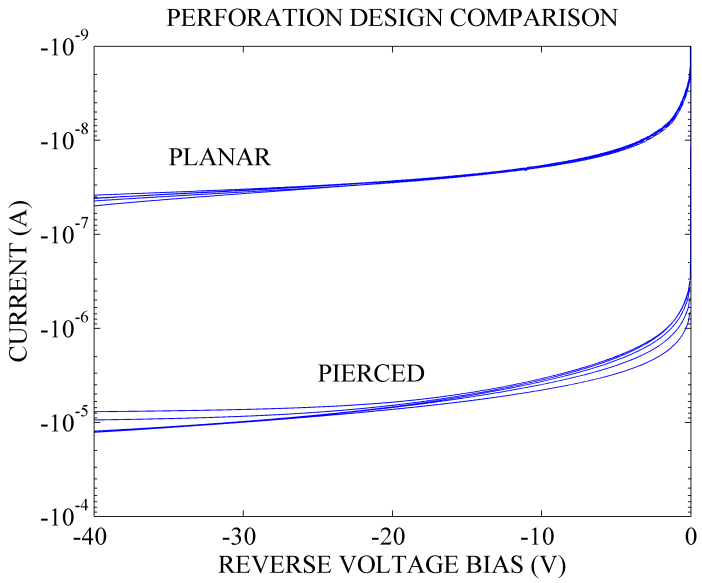

Figure 3.19: *Leakage current resulting from piercing perforated diodes compared to its planar diode counter-part.*

the sidewall surfaces or perhaps contaminated the silicon material. Exposed surfaces are a weakness in maintaining electrical properties of high resistivity semiconductor devices and often become a path of lower resistance than the bulk material. Semiconductor surfaces are also commonly a source of greater carrier generation and recombination, due in part by reduced carrier lifetimes. Regardless, the leakage current became unmanageable with this perforated design.

3.3 Selective Window Design

The proximity of the etched surfaces to the junction interface was considered to be detrimental in the piercing design. The greatest electric field in a pn-junction diode is located at the junction interface. Thus, a new design was considered that separated the etched surfaces from the junction interface, Fig. 3.20. The spacing between the two entities was achieved by patterning windows in the shallow diffusion layer such that holes could be etched through the windows without piercing the junction.

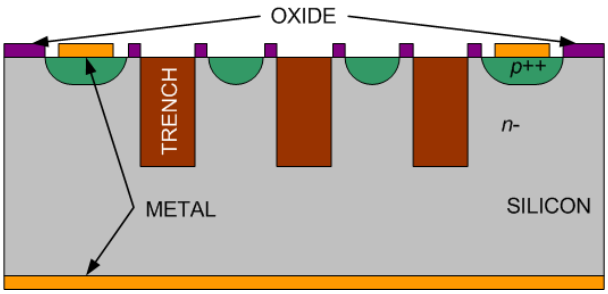

Figure 3.20: *The selective window design of perforated diode.*

A new photomask was designed to replace the existing diffusion mask. The new photomask included round dots within the diffusion area. These dots were 42 microns in diameter and replicated the pattern of the plasma etching mask, which utilized 30 micron dots. When the two patterns were aligned, a 6 micron buffer space existed between the diffusion pattern and the etch pattern.

3.3.1 Fabrication Process

The diode fabrication process to produce this selective window design was unchanged from previous work until the trench etching step. The only modification included the use of a new diffusion mask for boron diffusion. Implementing this method meant aligning the plasma etching mask pattern to the device structure much more precisely than before. In addition to the tight alignment, the plasma etching process had to be modified to remove the oxide layer left from the selective diffusion process. The device structure resulting from fabrication is shown in Fig. 3.21.

3.3.2 Theoretical Consideration

The etched surfaces of the trench side walls experience a reduced electric field in the selective window design due to the rounding of the diode diffusion layer and the space between the side wall and the junction interface. Electric field lines spread away from the junction interface toward the trenched surface and reduce the vertical component of the electric field

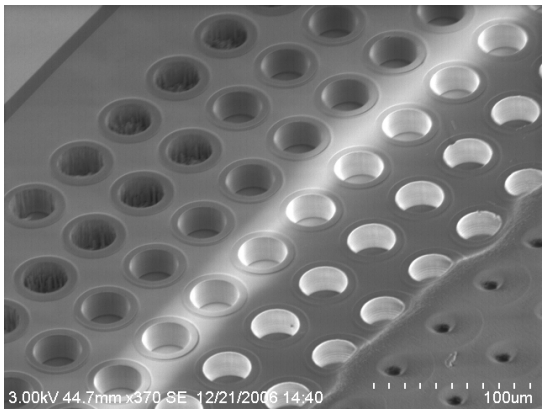

Figure 3.21: *A perforated diode surface utilizing the selective window design.*

near the compromised sidewall surfaces of the trenches. The Silvaco TCAD package was used to compare the vertical electric fields distributed within the piercing design and the selective design implementing a few microns of buffer spacing. The vertical electric field distribution was obtained, Fig. 3.22, for the piercing and selective window geometry.

A significant difference between the two designs is evident near the trench sidewall at the top of the structure. In the piercing model with 5 volts reverse bias, the peak electric field along the sidewall was determined to be -1560 V-cm^{-1}. This peak electric field is located within the purple region of the colormap. In the selective model it is clear that the greatest electric field only reaches the light-blue regime. The peak electric field along the sidewall in the selective geometry was determined to be -800 V-cm^{-1}, nearly half that of the piercing design.

In the piercing design the trench sidewall connects both poles of the diode in a direct fashion. Thus, the questionable etched surface may provide a more conductive path between the two poles of the pn-junction. In the selective design there is no direct connection between the etched surface and the p-type layer. Charge carriers injected from the p-type layer must travel some distance across the buffer spacing before reaching the less resistive trench wall.

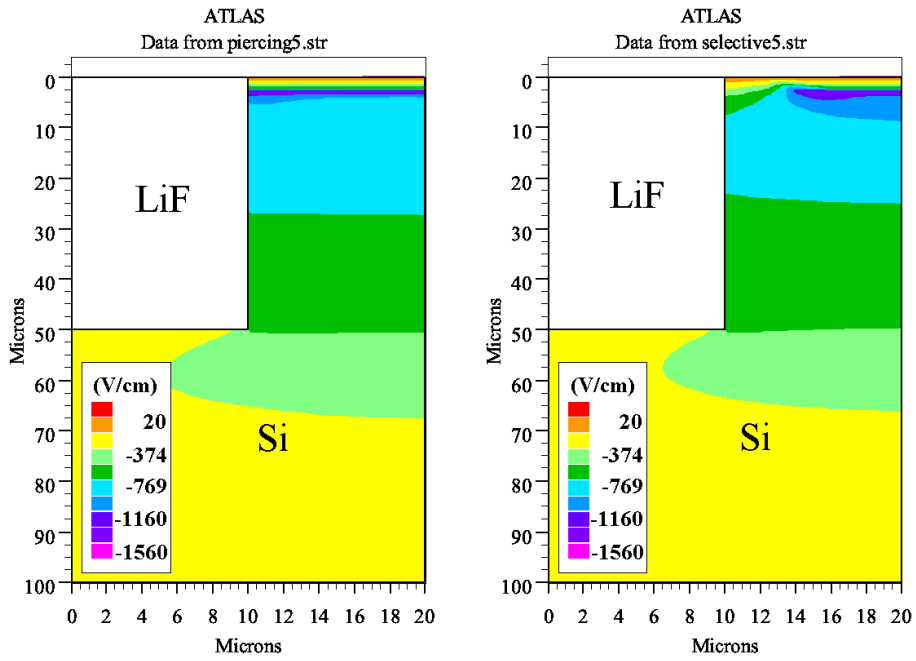

Figure 3.22: *Vertical component of electric field distributed within the piercing design (left) and the selective design (right), modeled with the Silvaco TCAD software package.*

3.3.3 Leakage Current

The selective window design improved the leakage current substantially over the previous piercing design. At 10 volts reverse bias, slightly less than 1 microamp of leakage current was observed, Fig. 3.23. Nearly an order of magnitude less leakage current is realized in this selective design compared to the piercing method of perforating a silicon diode.

3.4 In-Hole Oxidation Design

In further pursuit of reducing leakage current in the perforated diode structure, a surface passivation process was considered. Passivation provides a clean surface termination by growing an oxide layer on the questionable surfaces within the trenches, Fig. 3.24. Thus a thermal oxidation was implemented in conjunction with the selective window fabrication steps.

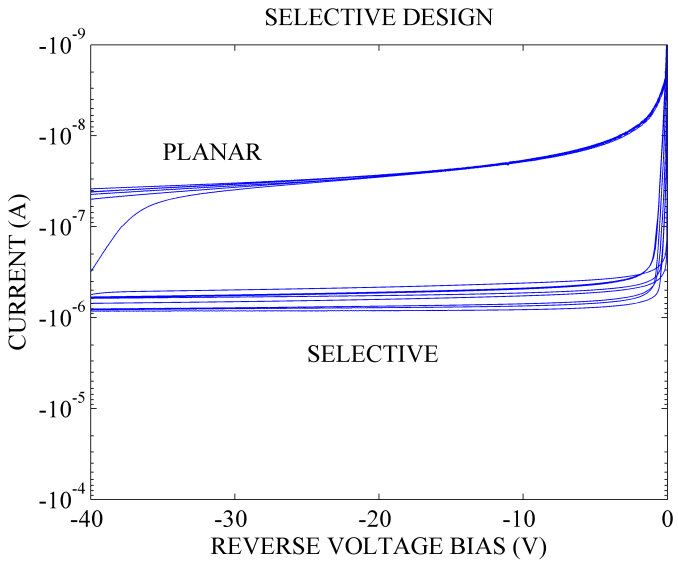

Figure 3.23: *Leakage current measured from the perforated diode selective diffusion design.*

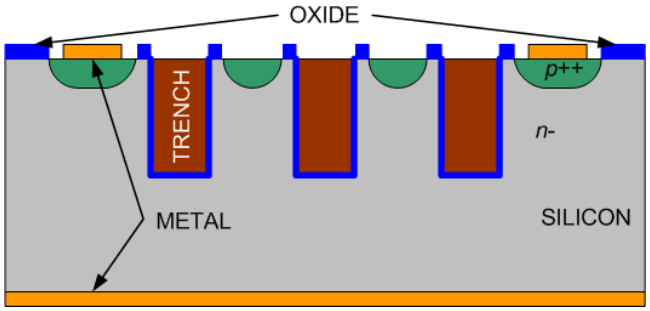

Figure 3.24: *The in-hole oxidation design of perforated diode.*

Growing a thermal oxide after etching the holes presented an incompatibility with the selective window fabrication process. The thermal oxidation cannot be performed after a metal film is deposited. Metal contacts cannot withstand the oxidation environment and diode failure is inevitable.

3.4.1 Fabrication Process

The in-hole oxidation device structure was constructed by patterning and depositing metal contacts after etching the trenches and growing the passivating oxide. Patterning pho-

toresist for metal lift-off over the deep trenches was challenging. Filling the trenches with photoresist was considered, but deemed undesirable because removal would be difficult or even impossible.

It was observed that thick photoresist, AZ 2070, would bridge over the microscopic holes. This left mostly void space within the holes and resist could be removed easily. The resist-bridge process was fairly repeatable over the small diameter holes. With the added thickness of resist however, the resist-bridge process was only useful for coarse alignments. Any alignment less than 5 microns was difficult to achieve repeatedly and often came with little success.

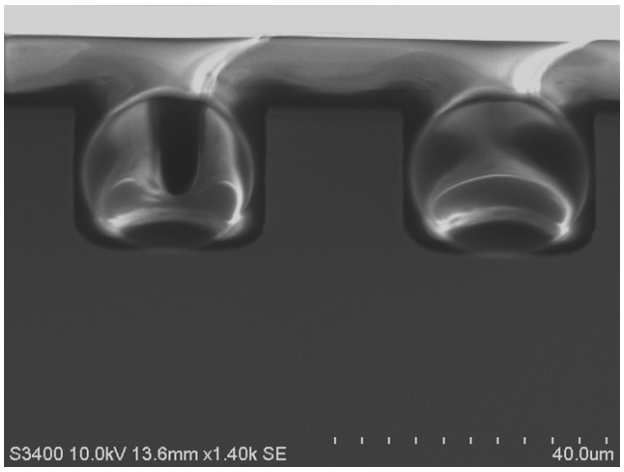

Figure 3.25: *Resist bridging over 30 micron deep trenches.*

The fabrication process for this in-hole oxidation design was identical to the planar fabrication process described earlier in Section 3.1.1 up until the LTO step after boron diffusion. Because both the boron diffusion and the side-wall passivation steps involve a thermal oxidation, the two procedures were combined. The oxidation procedure forming the in-hole passivation layer also served as the nitride removal process (LTO) required for solid-source boron diffusion. Focusing on the passivating role of the oxide, the LTO process was modified to be a dry oxidation at 900 °C rather than 800 °C. Also, the oxidation process was extended to 45 minutes.

Once the in-hole oxide layer was grown, the resist bridge technique was implemented for the purpose of metal lift-off over the trenched surface. Before metal evaporation, the oxide stripping process (BOE) was prolonged 1 minute to clear the thicker oxide resulting from the passivation oxidation process. This oxide etch also completed the deglaze step necessary from the boron diffusion. The final device appears identical to the selective diffusion device, Fig. 3.21, including the oxide ring indicating the buffer space around the trenches. However, a thin oxide layer exists within the holes. Note that a thermally grown oxide removes damage from the silicon surface within the perforations as it grows thicker.

3.4.2 Leakage Current

The in-hole oxidation process reduced leakage current beyond the selective window design. At 10 volts of reverse bias, the leakage current was observed to be roughly 100 nanoamps, Fig. 3.26. This level of leakage current is roughly two orders of magnitude less than the first perforated diode attempt involving a piercing design.

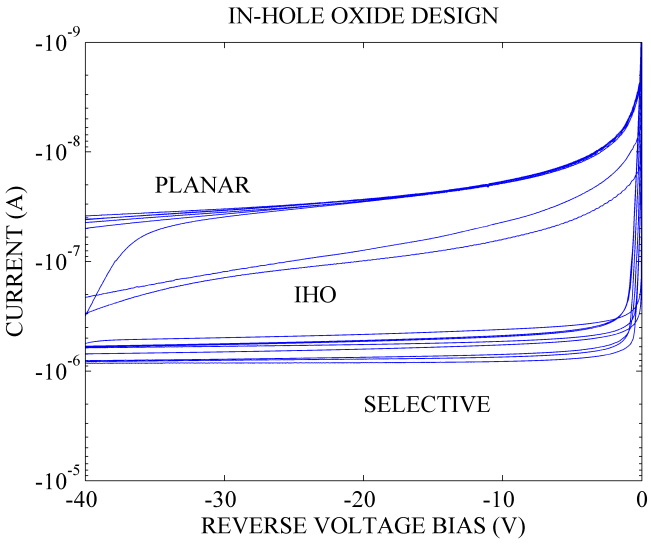

Figure 3.26: *Leakage current resulting from the in-hole oxidation design of perforated diode.*

With leakage current substantially below 1 microamp, the in-hole oxidized devices were much better suited for energetic charged particle detection. The fabrication process was

more complex than the previous efforts, but a good potential candidate for the perforated diode neutron detector was finally established. The work was later reported as an effective neutron sensor [16].

As improvements were being made in fabricating the perforated diode, parallel work advanced in the area of plasma etching the high aspect ratio trenches. Processes were finely tuned that produced deeper trenches while retaining smooth side walls. It was soon realized that the deeper trenches resulted in substantially greater leakage current. Even with the improvements presented here, leakage current once again approached several microamps as the trench depth grew to 100 microns. As a direct result, another design alternative was implemented.

3.5 In-hole Diffusion

To negate the effects of surface damage and/or contamination along the trench side-walls, a shallow p-type layer was diffused throughout the interior surfaces of the trenches. The result is a pn-junction that conforms to the surface morphology of the sensor, Fig. 3.27. This alternative design of producing a perforated diode is described in U.S. patent number 7164138 filed by McGregor in October of 2003 [17]. In addition, diffusing a pn-junction into deep silicon cavities has been successfully implemented in other fields such as betavoltaic devices [18].

3.5.1 Fabrication Process

The in-hole diffused perforated diode was fabricated by first plasma etching the deep trenches into the surface of a wafer. Then the wafer was cleaned thoroughly before executing a standard oxidation procedure. The oxidation establishes a diffusion mask as before, but also consumes some of the damaged or contaminated surfaces left from plasma etching. The oxidation was followed by a photolithography step to pattern the diffusion area of the diode. After opening diffusion windows in the oxide with a BOE step, a standard boron diffusion

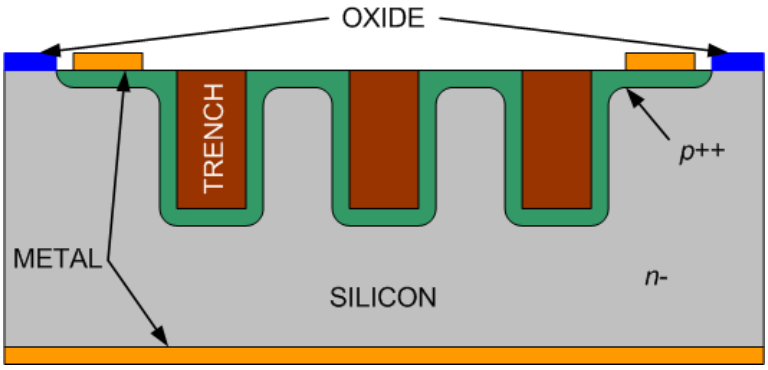

Figure 3.27: *The in-hole diffusion design of perforated diode.*

process then formed a shallow p-type layer that conformed to the trenched surface. Lastly, metal was deposited as described earlier with the in-hole oxidation design.

In addition to covering the suspect trench surfaces with a diffusion layer, the in-hole diffusion design alters the electrical geometry of the structure drastically. The p-type layer can be considered a conductive electrode that extends into the device along the trench side-walls and bottoms. This conformal electrode no longer follows a parallel-plate capacitor type of geometry.

3.5.2 Theoretical Consideration

A shallow p-type layer has the potential to deplete tens of micrometers of high resistivity silicon material. With a spacing between trench side-walls being only 30 microns, the depletion from each side-wall converges to cause a fully depleted condition between the trenches. This fully depleted condition occurs even with no reverse bias applied. In addition, the p-type layer across the bottom of the trenches guarantees that the depletion volume extends beyond the depth of the trenches.

With the previous perforated diode designs, reverse bias was necessary to deplete beyond the deep trenches and had the adverse effect of increasing leakage current and electronic noise. In a pn-junction the electric field near the end of the depletion region reduces to practically zero. Thus, poor carrier transport can be expected at the extent of the depletion

region near the bottom of the trenches. TCAD software was used to compare the electric potential within the selective window design and the in-hole diffusion design, Fig. 3.28.

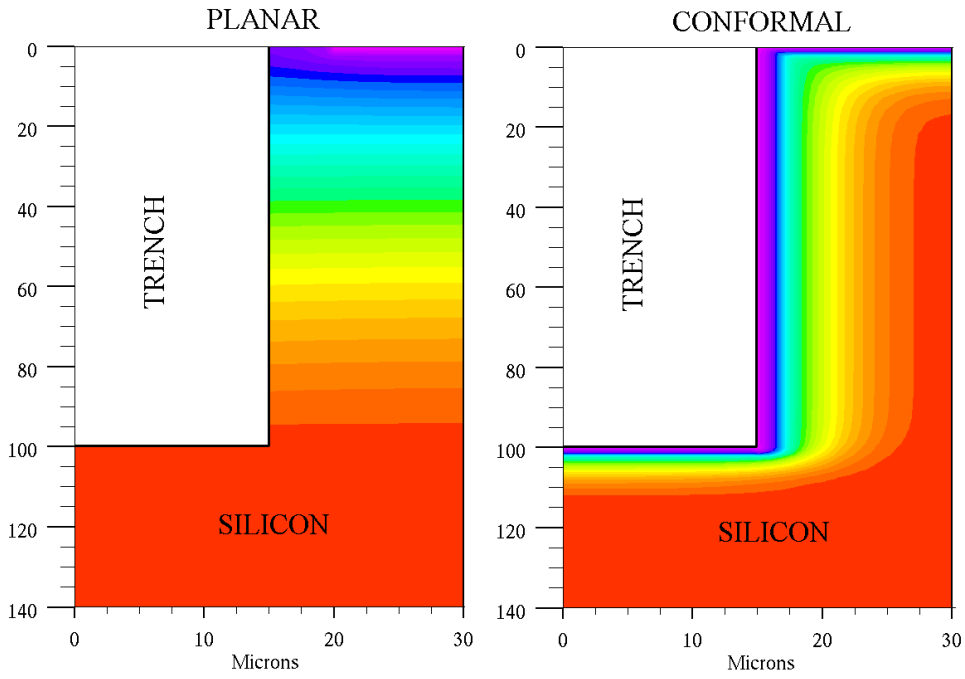

Figure 3.28: *Potential field models of the previous in-plane diode design (left) with selectively diffused windows and the conformal in-hole diffusion design (right).*

The selective design demonstrates a broadening gradient toward the bottom of the trench. Beyond the depth of the trench there is no gradient, indicating the presence of a low electric field. On the other hand in the conformal design, a sharp gradient exists near the sidewall and bottom of the trench.

3.5.3 Leakage Current

The in-hole diffusion design demonstrated less leakage current than any of the previous efforts. Much deeper trenches were fabricated while maintaining the low level of leakage current required to sense small ionization signals. The results of leakage current testing are plotted in Fig. 3.29. With trench depths of 100 microns, leakage current was an order of magnitude less than the in-hole oxide design, which increased to nearly 10 microamps.

A neutron detection performance comparison between the two designs was later reported showing the benefits of the in-hole diffusion design as a neutron sensor [19].

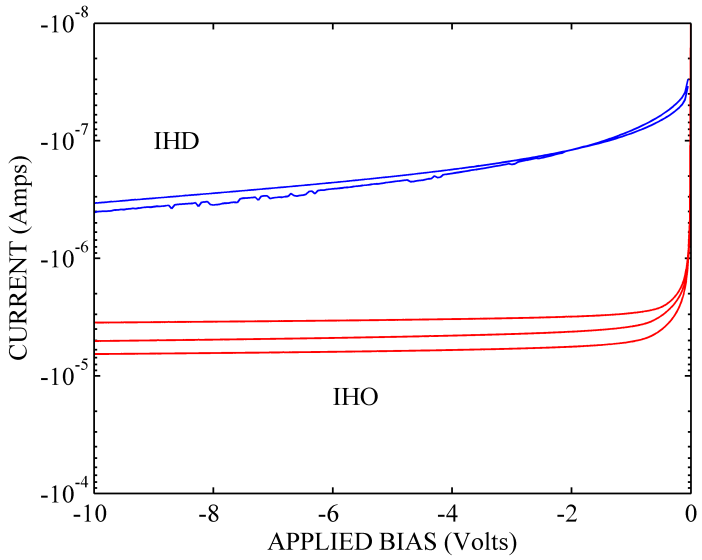

Figure 3.29: *Leakage current comparison between diodes of in-hole diffusion (IHD) and in-hole oxidation (IHO) designs with 100 micron deep holes.*

Chapter 4

Coating and Filling Diode Structures

4.1 Planar Diode Coating

Thin neutron conversion films are typically applied with an evaporation process. Lithium-Fluoride is a unique material to evaporate via e-beam, especially if the starting material is powder. One must heat the material very slowly the first time so that the powder can conglomerate into a fluid melt without blowing material out of the crucible with the electron beam. Colors of green, dark-blue, and purple, hover away as impurities vaporize and the source material becomes molten orange.

A flat aluminum plate was used as a shadow mask to deposit ^{6}LiF within the metal ring contact on the diode surface. Deposition was performed on an entire wafer with 5.5 millimeter round holes through the mask on a 7 mm by 7 mm pitch, matching the diode spacing. Utilizing a shadow mask, an entire wafer of diodes may be coated without photolithography, etching, or lift-off procedures.

Deposition rates up to 10 Angstroms per second were maintained with the e-beam evaporator. Thick films appear soft-white on the wafer surface, Fig. 4.1. Prolonged exposure to humid air over a period of many days was observed to cause LiF films to delaminate or flake-off from diode surfaces. Thus encapsulation of the deposited film was required. Successful encapsulates include photo-sensitive polymer material that can be patterned, dipping compounds, evaporation, or aerosols that can be painted on.

Figure 4.1: *Evaporated LiF film coating on a diode structure.*

4.2 Filling of Microscopic Perforated Structures

Four methods of filling microscopic trenches with LiF were investigated with varying success. These methods include evaporation, powder filling, melting, and a condensation technique. Each method is described and its level of success is discussed.

4.2.1 Evaporation

Evaporation is not an effective method for filling deep, high aspect ratio, trenches with LiF. Typically when depositing materials through vapor transport, one is concerned with the build up of material on the side-walls. A nearly parallel incident deposition condition was explored, with a small source in a vacuum medium at a significant distance from the target. With parallel incidence, side-wall deposition should be minimized. However, with LiF and its filamentary deposition behavior, a rapid closing of the deep cavities took place.

LiF was observed to seed well on slight changes in surface contours. The deposited material followed a crystalline type of growth that resulted in many small structures or grains that grew preferentially in a direction normal to the surface. The disadvantage in trench filling with this method is clear when the LiF hairs grow from the contours at the edge of a trench, Fig. 4.2. The hairs reach out over the trench and block the cavity from further

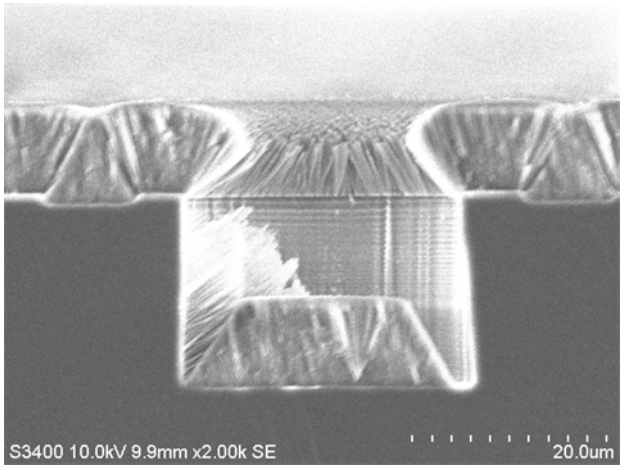

Figure 4.2: *Hole closing off at the top from evaporated coating.*

deposition. A 30 micron wide hole became pinched off after several microns of material was deposited.

Minimal tapering of the trench side walls may provide useful deposition from the sidewall surface toward the center of a shallow trench. Some void may still remain, but the potential exists to fill most of the volume. Sidewall tapering unfortunately is not an option when trench aspect ratios of 10:1 are foreseeable in the perforated diode design. There is no lateral space for such a structure in an aggressive perforated diode design.

4.2.2 Powder Filling

Enriched ^{6}LiF was produced from source materials including enriched ^{6}Li metal, de-ionized water, and hydrofluoric acid. Slowly adding small amounts of Li metal to water produced lithium hydroxide and hydrogen gas. Then through an acid/base reaction, the addition of hydrofluoric acid to lithium hydroxide resulted in the precipitation of LiF powder. After dehydration the powder had grain sizes around 5 micrometers. With some mortar and pestle work, the LiF powder could be ground down further to submicron grain sizes.

Trenches were filled with ^{6}LiF powder by dragging a soft object over the powder covered surface repeatedly. Pushing an accumulation of the soft powder across the surface with a

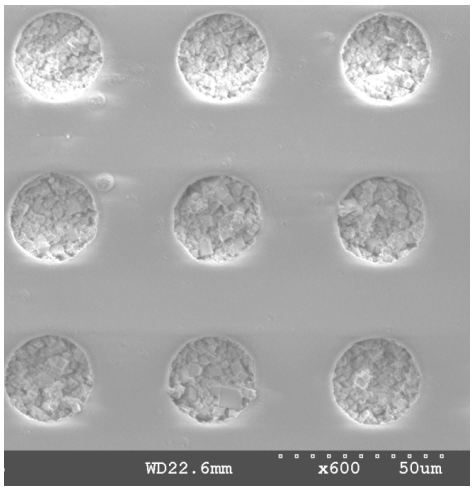

Figure 4.3: *Trenches filled with powder.*

slight downward force, the accumulation would reduce in volume as the material found its way into the deep cavities. When the reduction of source material ceased, it was assumed that the cavities were filled and not accepting any more material, Fig. 4.3.

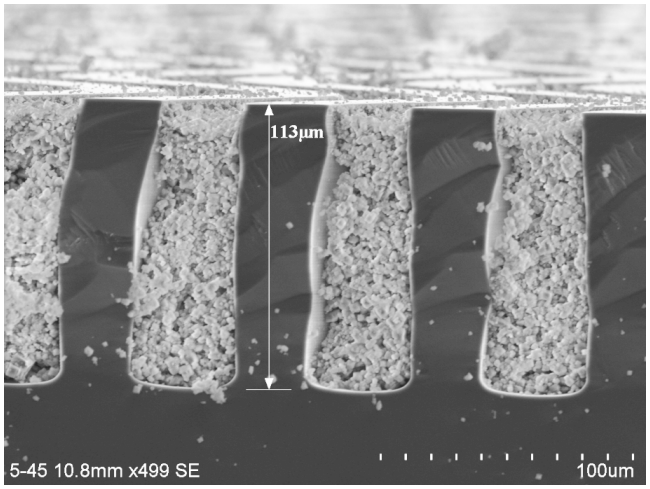

Figure 4.4: *30 micron wide trenches over 100 microns deep filled with* ^{6}LiF *powder.*

With powder filling, a 100% packing fraction may not be achieved unless a great deal of force is applied to the powder. Considering that material density can improve neutron absorption, one may be interested in a solid filling technique. However, charged particle

capture is critically important and is inversely related to the density of the conversion material. Thus, a lesser packing fraction will have the result of improving the probability of charged particle escape from the trench. A cross-sectional view of a powder filled trench, Fig. 4.4, shows that powder can be packed deep into the narrow cavities and also a significant fill fraction is apparent. Regardless of the immediate success with powder filling, the search continued for a feasible solid filling process.

4.2.3 Melting

LiF powder was melted on top of a perforated silicon structure in a chamber at a vacuum of 20 milliTorr. The chamber was purged with argon gas before pumping the vacuum to remove reactive gases such as oxygen. A quartz lamp above the substrate was turned on and current was slowly increased. When the powder was observed to melt, looking through a view-port, the temperature of a thermocouple under the substrate indicated 790 °C. Immediately thereafter, the temperature was steadily reduced to room-temperature. The entire thermal cycle lasted less than one minute and resulted in a solid fill of the microscopic cavities in the silicon substrate, Fig. 4.5.

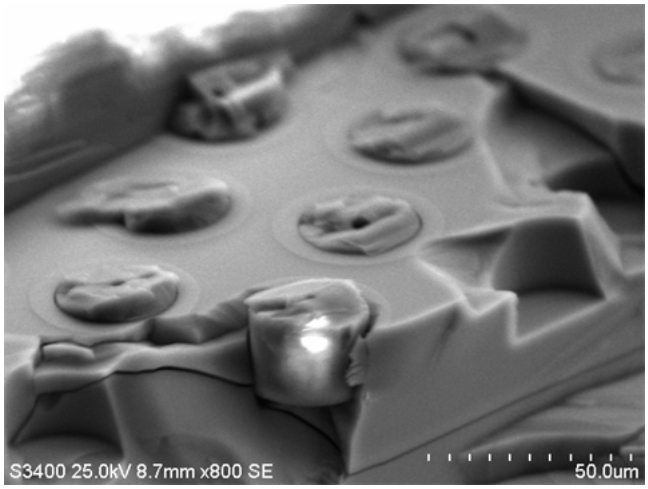

Figure 4.5: *LiF solid fill by melting powder material on top of the perforated structure with shallow holes.*

The viscosity and surface tension of the molten LiF was apparently low enough for the melt to flow into the microscopic structures. Solid filling is apparent by the fractures exposed from breaking away the excess material on top of the structure. Also, the solidified material molded to the shape of the cavities in the silicon.

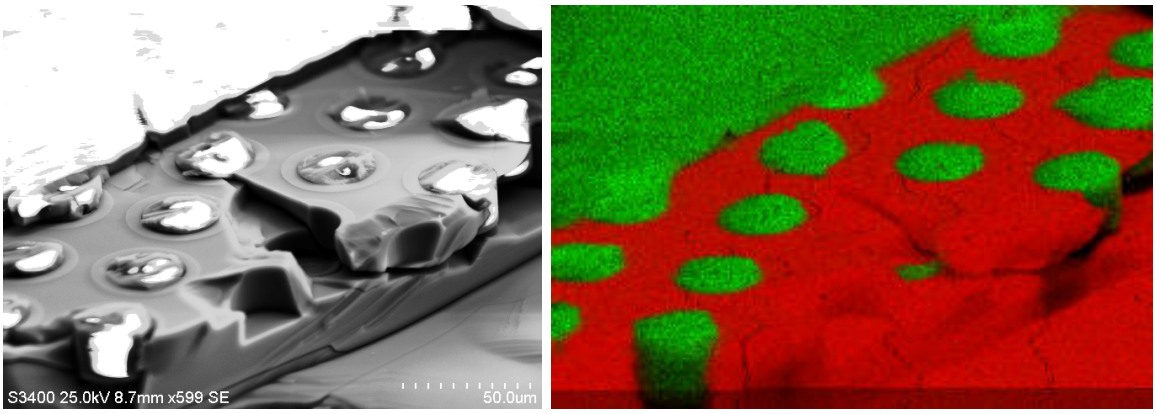

(a) SEM Image. (b) X-Ray Fluorescence.

Figure 4.6: *A scanning electron microscope image (left) and X-ray fluorescence (XRF) micrograph of the resulting melt-fill process (right). Red represents silicon and green indicates the presence of Fluorine.*

An X-ray fluorescence (XRF) scan of the filled structure, Fig. 4.6(b), showed no sign of any unusual elements including oxygen in the form of a bulk oxide or similarly any nitride. The filling material appears to contain a dense concentration of fluorine while the substrate shows entirely silicon. Lithium was below the measuring capabilities of the XRF system.

The melting process was repeated on a completely fabricated diode, rather than just a perforated slab of silicon. After the melt process, the rectifying properties of the diode were lost all together. The lack of rectifying behavior indicates that severe contamination of the diode material took place. At the high temperature required to melt LiF, there are many contaminants that can diffuse quickly into the silicon material. Lithium is a well known fast-diffuser and an n-type dopant in silicon. Also fluorine is an effective etchant for both silicon and silicon dioxide material. Unfortunately, the deeply etched trenches provide direct

access to the most sensitive part of the diode, the high resistivity bulk where depletion must take place.

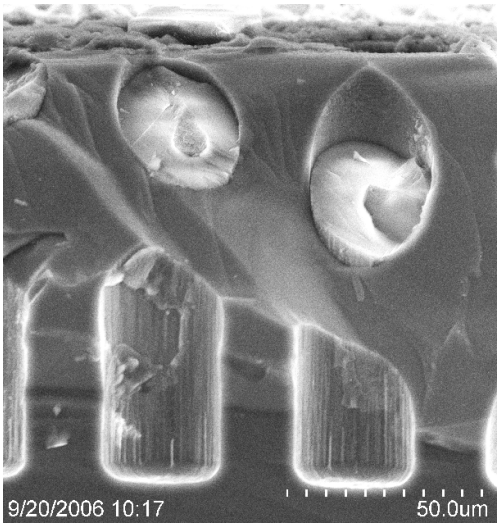

Figure 4.7: *LiF solid fill by melting material on top of a hole-perforated structure 100 microns deep.*

A solid fill of 100 micron deep trenches is shown in Fig. 4.7. This result may be interesting for other fields of work. However, if deep trench filling is to be done with a diode device, the internal structure of the diode must be protected from contamination at these elevated temperatures. Perhaps in future work some diffusion barrier can be implemented with success. On the other hand, a process that retains lower temperatures may be more interesting.

4.2.4 Condensation Deposition

Another solid filling method was investigated that allowed the temperature of the substrate to be much less than the melting point of LiF. This involved condensing LiF vapor onto a cooled wafer. If the wafer can be cooled from the backside, the potential for condensation may be more prevalent toward the bottom of the trenches and might reduce the tendency of the trench to close off at the top.

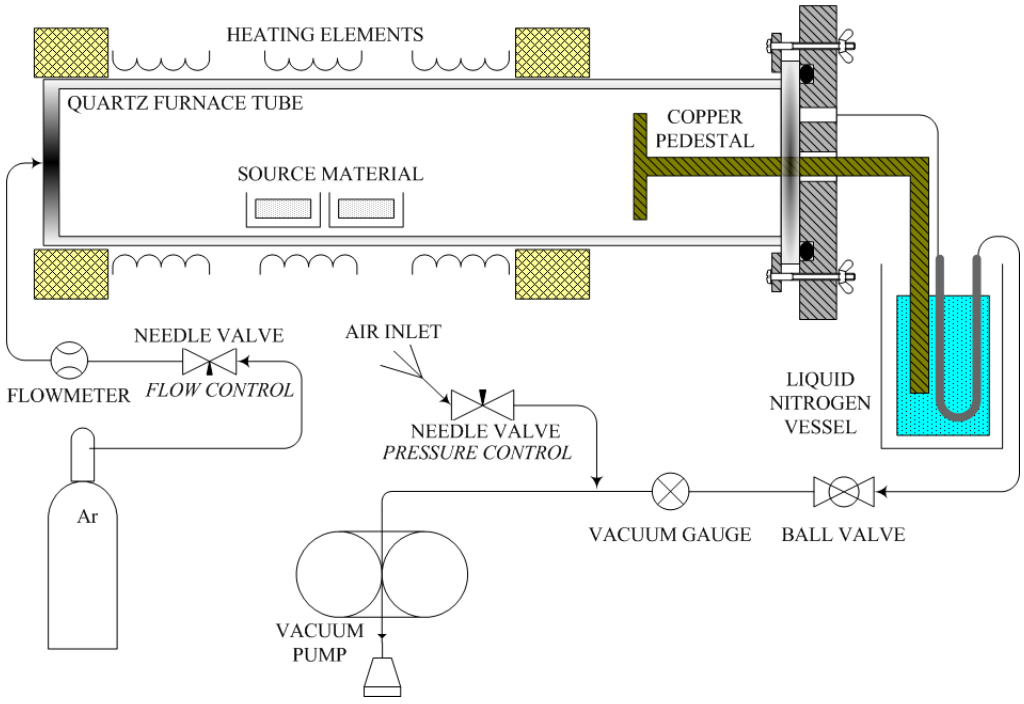

Figure 4.8: *Condensation apparatus for filling trenches via vapor transport.*

The condensation process required a tube furnace with an air-tight cap such that the chamber could be purged with inert gas, Fig. 4.8. The inert environment minimizes unwanted reactions at elevated temperature. A unique fitting was made to seal one end of the furnace tube so a wafer could be mounted on a heat-sink pedestal. The opposing end of the pedestal protruded out of the chamber where it was submerged in liquid nitrogen. A vacuum pump controlled the chamber pressure and drew the inert gas toward the wafer pedestal.

After much work and several trials it was discovered that LiF could be condensed onto the wafer and into the microscopic cavities, Fig. 4.2.4. The variables in the process greatly affect deposition rate as well as the porosity of the deposited material. Coarse grains of deposited material were first observed in preliminary process runs. With the correct environmental conditions, the porosity could be reduced to the extent that the depositing material appeared solid.

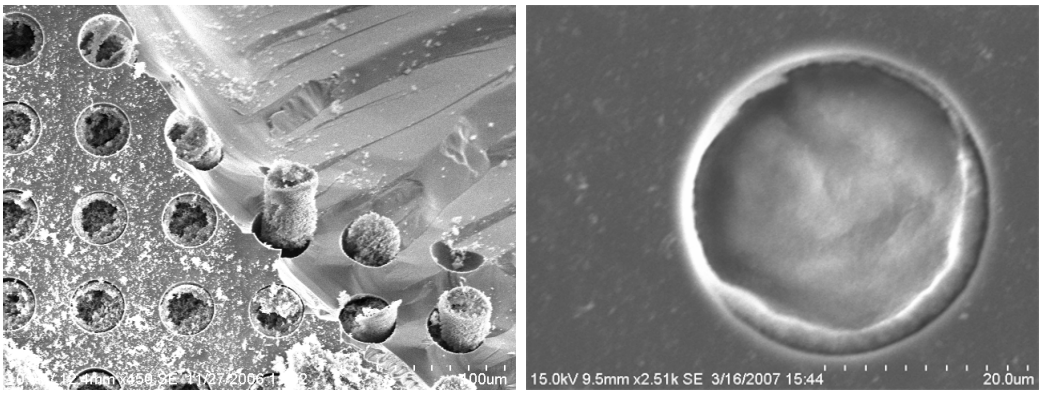

(a) Birds-eye view of filling. (b) Close-up of optimized results.

Figure 4.9: *Filling of 30 micron diameter holes with LiF via condensation.*

The downfall of this technique was the deposition rate. Though the wafer temperature could be kept below the melting point of LiF, as many as 8 hours of duration were required to fill cavities that were less than 100 micrometers deep. Considering future plans to make trenches 250 micrometers deep, and the interest in high-volume manufacture, the condensation method was considered an unsuitable filling technique. As a side note, the condensation method demonstrated to be useful in synthesizing very fine grained LiF material on a nanometer scale.

4.2.5 Powder Filling and Evaporation

Powder filling and evaporation were combined in some cases to form a cap over the powder filled trenches, Fig. 4.10. The cap of neutron sensitive material has the potential to improve efficiency very slightly. However, the slight benefit of a cap layer is generally not worth the difficulty involved with its implementation. The charged particle capture probability of the cap, like the thick-film geometry, is poor and absorbs a significant fraction of neutrons without registering a count. This wasting of neutrons reduces the potential to detect neutrons with a second sensor or after a scatter from nearby material.

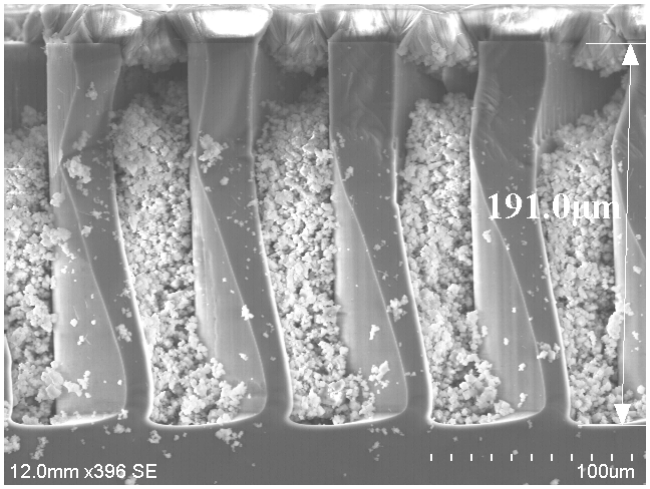

Figure 4.10: *Powder filling with evaporated cap.*

Chapter 5

Sensor Testing and Performance

The silicon diode utilized in thin-film or perforated sensors must be able to detect charged particles before it can be expected to detect neutrons. It was standard practice in this work to test diodes for leakage current, then charged-particle response, and finally neutron response. The incremental testing allowed for an early identification of failure during sensor fabrication.

5.1 Alpha Particle Detection

Americium-241 was used as a source of energetic alpha particles. The primary alpha emissions from ^{241}Am have energies of 5.49 MeV and 5.55 MeV [20]. These energies are quite large compared to the 2.73 MeV triton and the 2.05 MeV alpha particle released by a neutron capture in ^{6}Li. In the leakage current testing station a perforated diode was connected to an Ortec 142A pre-amplifier and was exposed to the alpha source. Signal pulses were observed and captured with a digital oscilloscope, Fig. 5.1.

The two pulses in Fig. 5.1 indicate consecutive alpha particles entering the diode and depositing similar amounts of energy. The fast rise and long tail are typical of a pre-amplifier output signal. The signal is distinct from baseline noise, indicating a good signal-to-noise ratio. Gadolinium-148 is a more appropriate charged particle source to use in simulating the conversion products from ^{6}Li. The ^{148}Gd source emits alpha particles with 3.18 MeV of energy [21] and will supply signal pulses with a magnitude closer to what is expected from

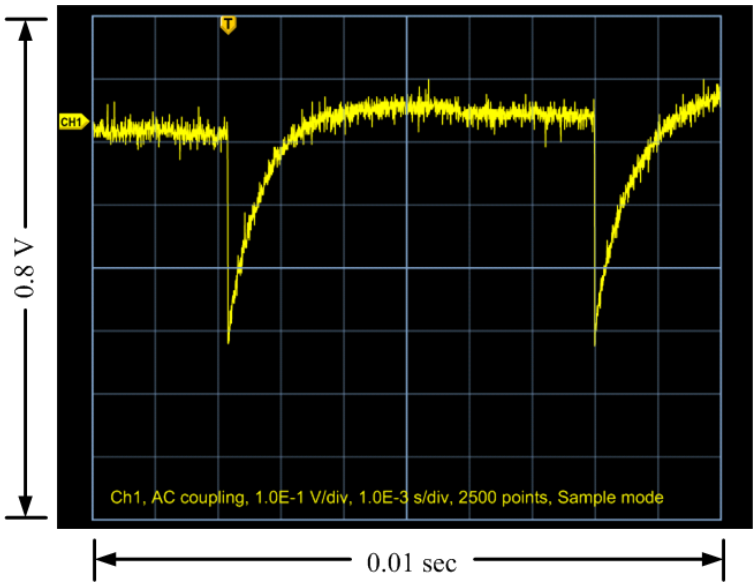

Figure 5.1: *Signal pulses from alpha particle interactions in a perforated silicon diode.*

the charged particle reaction products resulting from neutron interactions in ^{6}Li. Also, a pulse height spectrum collected from the alpha particle response provides much more information about the performance of the sensor.

A pulse height spectrum was collected from an in-hole oxidized perforated diode over a duration of time that included exposure to an ^{241}Am alpha source and a ^{148}Gd alpha source. The spectrum shows an accumulation of pulses at two different energies showing up as peaks, Fig. 5.2.

The lower-level discriminator (LLD) was set at a level just above where counts began accumulating from the electronic noise level. The peaks in the spectrum indicate that the sensitive volume or depletion region is large enough to capture most of the energy of the penetrating particles. The 3.18 MeV alpha particle from the gadolinium source is responsible for the left peak in the spectrum. Because the neutron reaction products from ^{6}Li are at 2.05 and 2.73 MeV, one can predict that signal pulses resulting from the full capture of each particle will reside somewhere just to the left of the 3.18 MeV gadolinium peak in the spectrum. Because the perforated diode design offers the chance for capturing

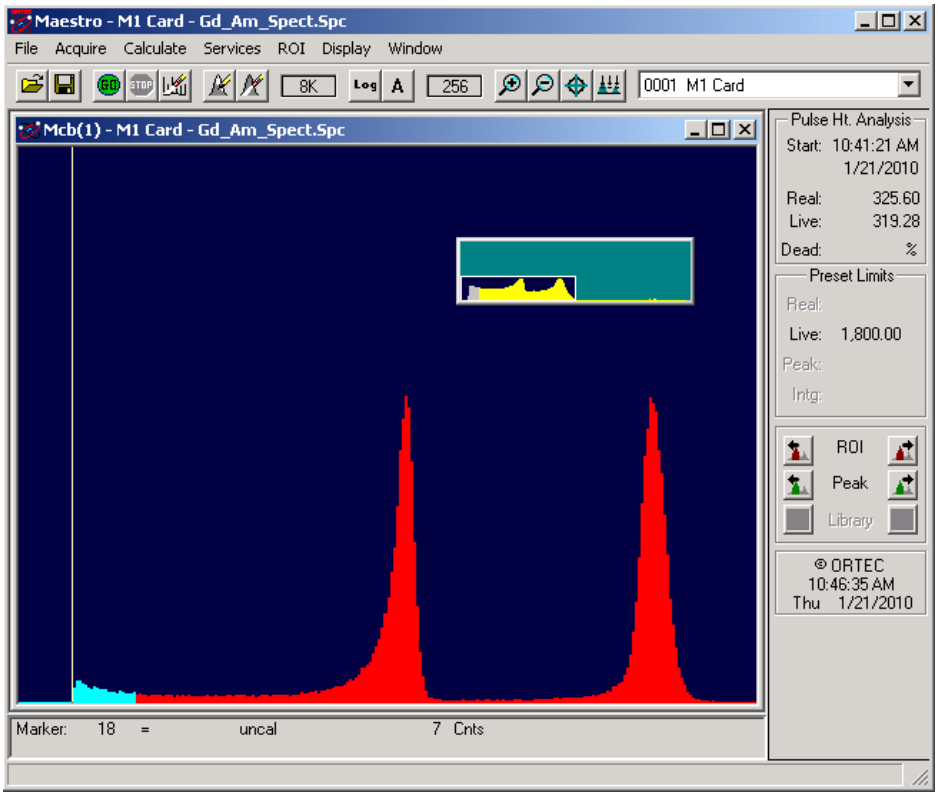

Figure 5.2: *Alpha particle pulse height spectrum produced by a hole-patterned microstructured sensor irradiated consecutively from sources of* ^{241}Am *and* ^{148}Gd.

both particles simultaneously, the spectral response from neutrons may include counts that extend up to 4.78 MeV, closer to the 5.5 MeV americium peak on the right in the charged particle spectrum.

5.2 Testing for Neutron Response

Verifying or confirming measurements made with a diffuse neutron source becomes difficult experimentally or through simulation. On the other hand, a beam of mono-energetic neutrons is more specific and can be simulated more accurately. Setting up a mono-energetic neutron beam is somewhat involved. However, devices such as neutron monochromators are becoming common-place at major neutron beam-line facilities and provide an ideal testing configuration.

5.2.1 Diffracted Neutron Beam

A narrow neutron beam was utilized from a radial beam-port of the TRIGA Mark II nuclear reactor at Kansas State University. A neutron monochromator was installed in this beam to provide mono-energetic neutrons through a diffraction mechanism. As part of a master thesis project, the installation of the KSU monochromator was lead by Troy Unruh [22]. In that work, the neutron energy in the diffracted beam was determined to be 0.0253 eV.

The entire diffractometer arrangement was shielded excessively with borated high-density polyethylene as well as concrete. The only exception was a 0.5-inch diameter hole aligned with the exiting beam of the monochromator. Thus, the diffracted exiting beam was collimated to 0.5 inches in diameter. The excessive shielding was effective at reducing spurious albedo neutrons scattered outside of the beam.

5.2.2 Thin-Film Coated Diode Neutron Response

The response of the thin-film neutron sensor is well documented [3] and can be produced with theoretical models as was done earlier, Fig. 2.7. A planar diode that tested well in leakage current and alpha particle detection was coated with a thin film of ^{6}LiF via e-beam evaporation. The thickness of the deposited film was measured to be 1400 angstroms, or 0.14 microns, with a profilometer. The sensor was placed in the center of the diffracted neutron beam and a pulse height spectrum was collected, Fig. 5.3.

The resulting spectrum was characteristic of a conversion film much thinner than the range of the two charged particle reaction products. A separate peak is clearly defined for the 2.05 MeV alpha particle and the 2.73 MeV triton reaction products from ^{6}Li. The narrow resolution of the energy peaks confirms there is a high probability of capturing the full energy of the charged particles. Also, the similarity to the simulated spectrum shown earlier, Fig. 2.7, indicates that energy deposited in the diode is being effectively formed into signal. Recall that, the simulation only considered the energy deposited by the charged particles and not the signal formation mechanisms. With a Cd shutter in the beam, sensor

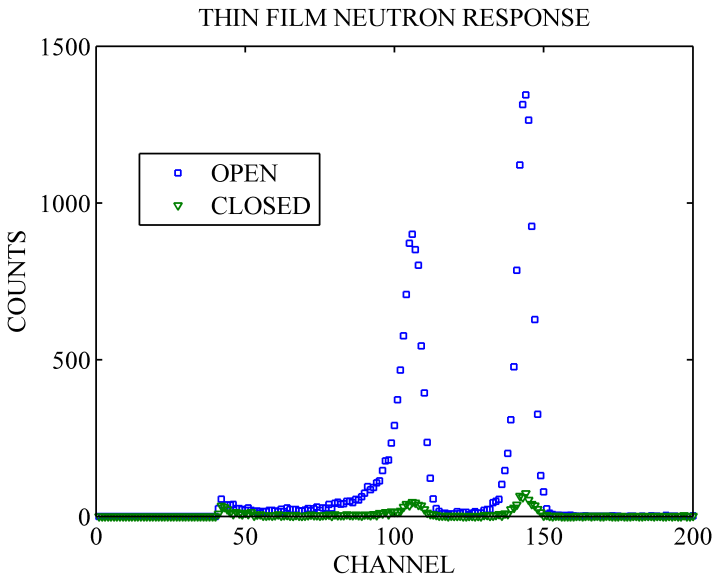

Figure 5.3: *Neutron pulse height spectrum from thin-film coated diode with 0.14 nanometers of ^{6}LiF, acquired with a Cd shutter open and closed.*

response is greatly suppressed and indicates that the detection of background radiation and non-thermal neutrons is negligible.

Thick-film Device Neutron Response

To further parallel historical work and theory, a ^{6}LiF film was evaporated 26 micrometers thick onto a planar diode and tested as a neutron sensor. The pulse height spectrum resulting from the experiment is given in Fig. 5.4.

The spectrum does not display any resolved peaks, but rather a long shelf with a distinct edge which represents the maximum energy collected from the 2.73 MeV tritons. Looking closely, there is a small ledge near channel 100 that represents the maximum energy of the 2.05 MeV alpha particles. The spectral shape is similar to the simulated spectra of a thick film coated diode neutron sensor shown earlier, Fig. 2.8.

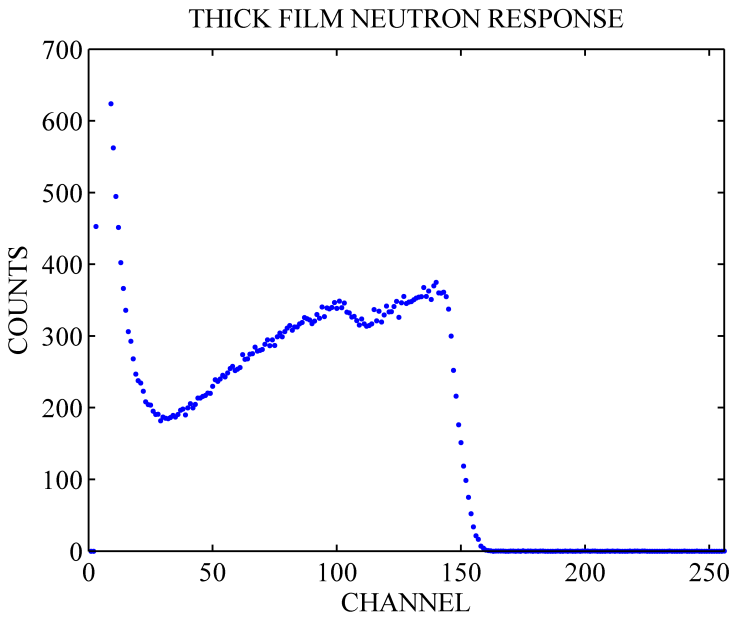

Figure 5.4: *Neutron pulse height spectrum from a thin-film coated diode with 26 microns of* ^{6}LiF.

5.2.3 Hole Pattern

An in-hole oxidized perforated diode with round holes 22 microns deep was filled with ^{6}LiF powder and tested in the diffracted beam. The device also employed an evaporated film of ^{6}LiF conversion material, 20 microns thick, over the powder-filled trenches. The neutron response, Fig. 5.5, shows a slight rise in counts from channel 20 toward the right approaching a defined shelf at channel 65. The shelf is abrupt but does not drop to zero counts as before with the thick film device. There is a significant accumulation of counts to the right of the shelf edge, forming a tail of counts extending toward higher energy. As discussed earlier in Section 2.5, the random processes that take place in detecting neutrons can be simulated with Monte Carlo computational routines. A simulation for this sensor geometry was supplied by Prof. Kenneth Shultis of Kansas State University and a routine was executed, Fig. 5.6, to compare with the experimentally obtained data.

The simulated spectrum shows some similarities to the experimentally collected pulse height spectrum. A gentle rise in the number of counts can be seen leading rightward toward

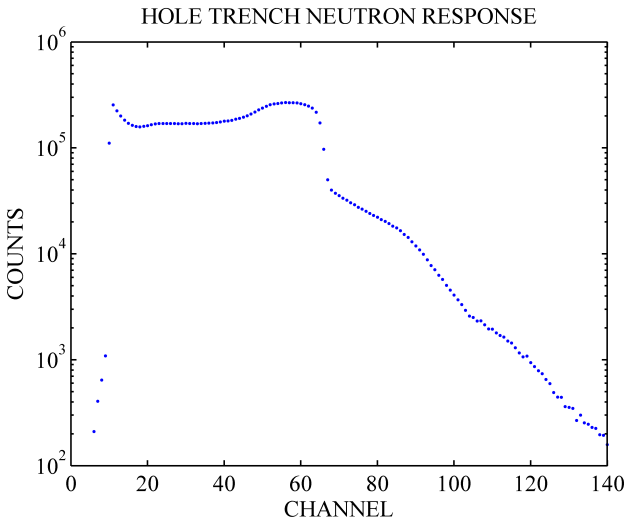

Figure 5.5: *Neutron pulse height spectrum obtained from a hole-patterned device, 22 microns deep, fabricated with the in-hole oxidation process. The trenches were filled with* ^6LiF *powder and 20 microns of* ^6LiF *coated the surface.*

a distinct shelf. In addition, the shelf edge does not reach lower to zero counts. As in the experimentally gathered spectrum, there is a high-energy tail of counts extending rightward from the base of the shelf edge. The short ledge from the alpha particle maximum energy is one missing feature from the experimental data. The experimental spectrum is excessively smeared which is likely masking the subtle feature from the alpha particle capture. The smearing can be attributed to electronic noise in the system and perhaps other non-ideal behaviors that stem from leakage current and manufactured imperfections.

Counts extending to the right of the shelf must represent high energy counts from capturing energy from both the triton and the alpha particle in a single neutron absorption. The probability of capturing both particles is relatively low, evident by the height of the shelf edge. The much greater chance of capturing a single triton raises the number of counts well above the two-particle capture scenario. The similarity between the experimentally gathered spectrum and the simulated spectrum of 5.6 confirms the functionality of perforated neutron sensor. If any of the operational mechanisms between capturing the neutron and extracting the signal were executed poorly, such an ideal spectrum would not have resulted.

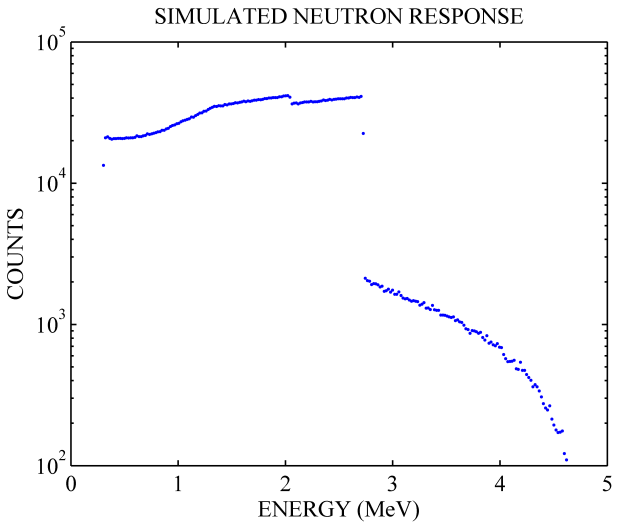

Figure 5.6: *A simulated pulse height spectrum for a hole-trenched device backfilled with* ^{6}*LiF and incorporating a 20 micron film coating of* ^{6}*LiF. Courtesy of Prof. Kenneth Shultis.*

5.2.4 Sinusoid

An in-hole oxidized sinusoidal trenched device, 100 microns deep and filled with ^{6}LiF powder was tested for neutron response. The leakage current of this type of device was substantially greater than the hole-patterned device presented earlier, Fig. 5.5. The pulse height spectrum resulting from neutron testing is shown in Fig. 5.7.

The neutron response consists of a short flat profile near the bottom end of the spectrum that transitions into a declining slope. The slope gets steeper before transitioning into a tail of counts that reduces toward higher energies. The spectral response of the in-hole oxidized sinusoid device is questionable. From Table 2.4.2, the charged particle capture probability is greater than the thick-film design. Thus, fewer counts at lower energy should be expected, shifting counts in the spectrum toward the right. However, the experimentally gathered pulse height spectrum has many more counts at lower energy than any of the previously tested devices.

Spectral simulations of the sinusoid geometry are significantly more complicated than the hole and straight trench geometries. Simulations of this design are not yet available.

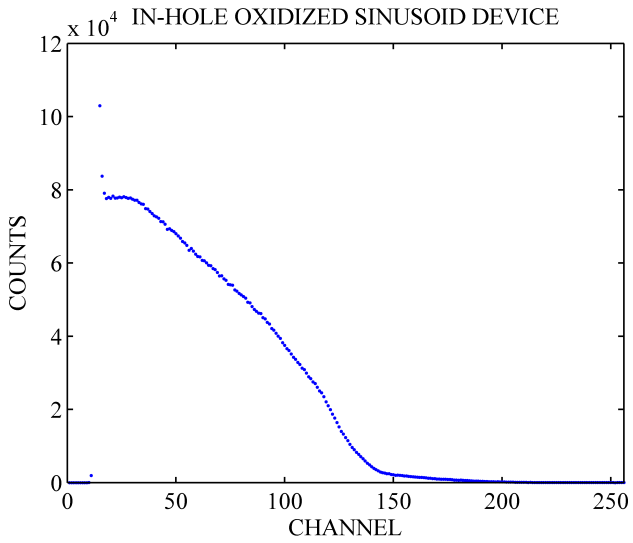

Figure 5.7: *Experimentally gathered pulse height spectrum of a sinusoid trenched device in a diffracted neutron beam. The trenches were 100 microns deep and powder filled with* ^{6}LiF*. The fabrication method implemented the in-hole oxidation process.*

This is due in-part to the complexity of ray tracing through the multiple solutions provided by a sine wave surface in 3-dimensional geometry.

The neutron response for the shallow hole device and the deeper sinusoidal trench device is representative of a trend observed in this work. With the in-hole oxidized fabrication process, the spectral neutron response has been shown to deteriorate significantly with increasing trench depth [23, 24]. Deterioration in signal becomes clear approaching 100 microns in trench depth and very extensive up to 200 microns in depth. As the depth goes beyond 100 microns the pulse height spectrum continues to shift to the lower energy range, to the point that the spectral shape takes the form of an exponential noise spectrum. The indication from Fig. 5.7 is that less energy is deposited in the detector than theoretically predicted, hence the depletion region in the device may not extend beyond the reaction product ranges.

5.2.5 In-Hole Diffused Sinusoid

It was shown in Chapter 3 that in-hole diffused devices demonstrate less leakage current. Following that effort, an in-hole diffused sinusoid trenched device was tested for neutron response. This in-hole diffused device shared the same trench pattern and depth of 100 microns as with the in-hole oxidized device just discussed, Section 5.7.

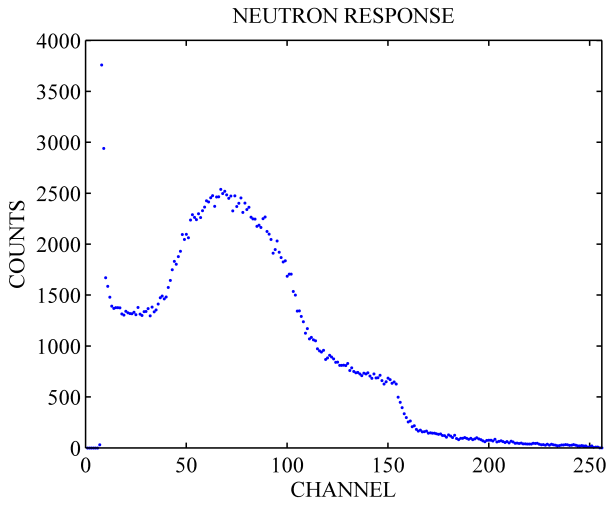

Figure 5.8: *Experimentally gathered pulse height spectrum of a sinusoid trenched device in a diffracted neutron beam. The trenches were 100 microns deep and powder filled with* ^{6}LiF*. The fabrication method implemented the in-hole diffusion process.*

The in-hole diffusion spectral response, Fig. 5.8, differs greatly from the in-hole oxidation device. A distinct valley exists toward the low-energy end of the spectrum, just above the noise level. To the right of the valley is a large hump. On the high-energy side of the hump, counts reduce and transition into a nearly level plateau. Then, the sharpest feature in the spectrum appears as a ledge or shelf at channel 160. Finally, the high-energy tail of counts is apparent again, as was seen in the hole-perforated sensor from before, Fig. 5.5.

The neutron response of the in-hole diffused device is a great improvement over the in-hole oxidized device for many reasons. First, the large dip in counts at low energy confirms that the charged particle capture probability is large. The sharp shelf at higher energy in the spectrum indicates the maximum energy of the 2.73 MeV tritons. Beyond the sharp ledge,

the counts represent capturing some energy from both the triton and the alpha particle simultaneously.

The shape of this spectrum shows resemblance to published theoretical spectra considering straight trenches of similar depths [13]. However, the similarities are limited to the shelf ledge and some form of reduced counts at lower energy. In the referenced work, this sinusoid spectrum closely resembles those theoretical spectra of straight trenches with a tighter spacing. This similarity is valid considering that the sinusoidal trenches stacked 30 microns apart at the peaks and valleys are only separated by 22 microns at their mid-wave. The improved spectral response over the in-hole oxidation design can be attributed to better signal formation in the in-hole diffusion design.

Bias and Response

In most diode-type radiation sensors, the characteristics of signal formation respond significantly to the applied bias. Commonly, greater reverse bias increases the depletion volume as well as the electric field that drives signal charge. Greater signal usually results along with increased noise and leakage current. A small amount of reverse bias was applied to an in-hole diffused neutron sensor perforated with 50 micron deep holes to note the change in spectral response, Fig. 5.9.

The applied reverse bias of 10 volts had the effect of shifting the spectrum rightward to higher energy. In addition, the large hump in the spectrum was stretched in the process. Another noticeable change is that the transition from the hump-like shape to the sharp ledge appears to be more distinct. The bias clearly increased the average pulse height produced by the device. However, the low-level noise also shifted rightward.

The in-hole oxidized devices discussed previously proved to be poor candidates for reverse bias. Leakage current with 100 micron deep trenches was already marginal without bias applied. The reverse bias simply made leakage current a severe problem. With the in-hole oxidation process the expected spectra either could not be obtained or suffered excessively from electronic noise.

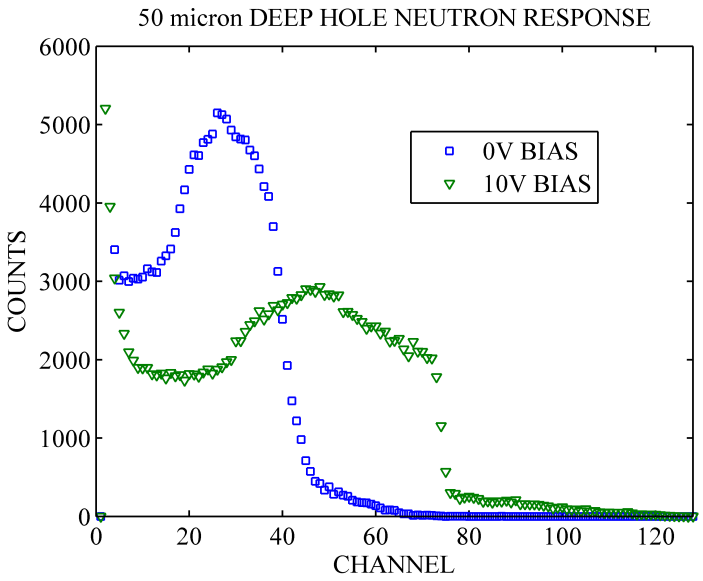

Figure 5.9: *Neutron response at different levels of reverse bias on a 50 micron deep, hole-patterned device.*

The response to reverse bias was also obtained for a 100 micron deep in-hole diffused sinusoid sensor. The trend is shown in Fig. 5.10 with multiple levels of reverse bias. The difference in response is significant between 0.5 volts and 5 volts, whereas 5, 10, and 20 volts only change the response slightly. The resulting trend is that the centroid of the hump moves rightward. Meanwhile, the height of the spectrum is reduced. This follows that the number of total counts should be conserved in the entire spectrum. The last jump in bias to 36 volts from 20 volts made a relatively dramatic change in response for the worse. The hump was almost completely flattened and the high energy ledge was smeared beyond recognition, most likely a consequence of higher leakage current.

The improving, then worsening, spectral response can be explained by a rapid increase in depletion in the device with just a small amount of bias. At some point with greater bias the device will begin to breakdown, significantly increasing leakage current along with electronic noise. The smeared spectrum at 36 volts is likely a result of the diode reaching the breakdown condition.

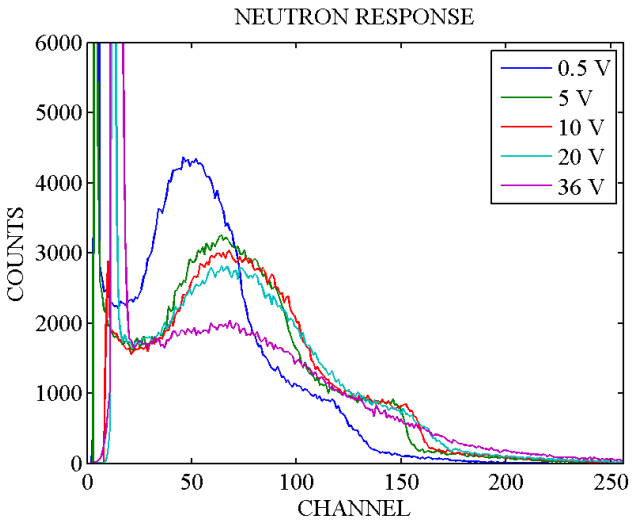

Figure 5.10: *Neutron response at different levels of reverse bias on a 100 micron deep, sinusoid trenched device.*

Beyond a few volts there is little gain in the application of reverse bias with the in-hole diffused devices. The limited gain in signal magnitude with applied bias goes against the traditional thought with planar diode designs. The diffusion into the trenches results in a non-planar geometry. With the diffusion layer being of high conductivity, electric potential will not drop greatly within its vicinity. As a result, the potential changes little between the trenches and there is only a small electric field present within the semiconductor fins to drift signal charge from ionization events.

Depth and Response

Deeper trenches have an adverse effect on the spectral response of the perforated sensors to neutron capture events. Neutron response spectra from similar devices with different trench depth have been plotted together for comparison, Fig. 5.11.

There is a definite trend in the response as trenches get deeper beyond 100 microns. From a trench depth of 100 microns up to 245 microns, the large wide hump shifts to lower energy and becomes narrower. Similarly, the valley of counts at low energy becomes shallower and narrower. Also, the sharp ledge is becoming smeared and much less defined as the trenches

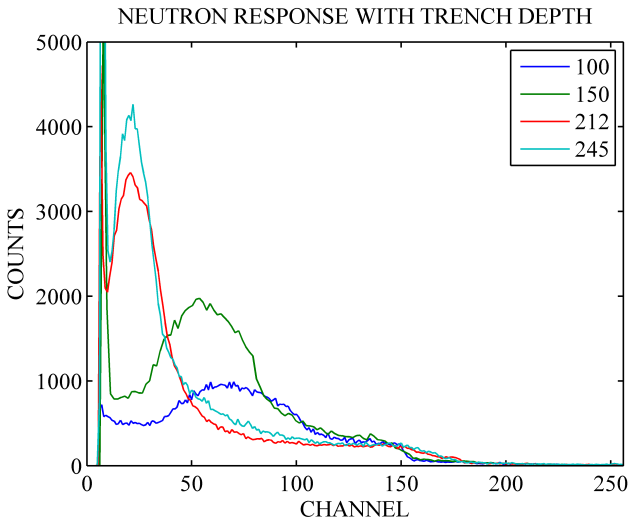

Figure 5.11: *Neutron response of in-hole diffused sinusoid devices with increasing trench depths.*

get deeper. The degrading shape of the spectral response indicates that signal formation is suffering in the diode as the trenches get deeper.

5.2.6 Simulating Signal Formation

A small cell of the trenched diode structure was defined as an input file for the ATLAS tool in the TCAD software package. A shallow p-type layer (0.5 micron) was defined along all surfaces of the trenches as well as across the top of the silicon material to represent a thermal diffusion process performed after the trenches were etched in the substrate. The width of silicon between the trenches is 30 microns and the thickness of the substrate was set to 300 microns.

The substrate resistivity was defined as 10,000 Ohm-cm with phosphorus as the primary impurity, uniformly distributed throughout the bulk. An electrode was defined at the top of the silicon, having width just less than the silicon fin between the trenches. Another electrode was defined along the entire bottom of the substrate to represent a monolithic back-side contact. Both of these electrodes were set to behave as ohmic contacts to minimize low-bias instabilities.

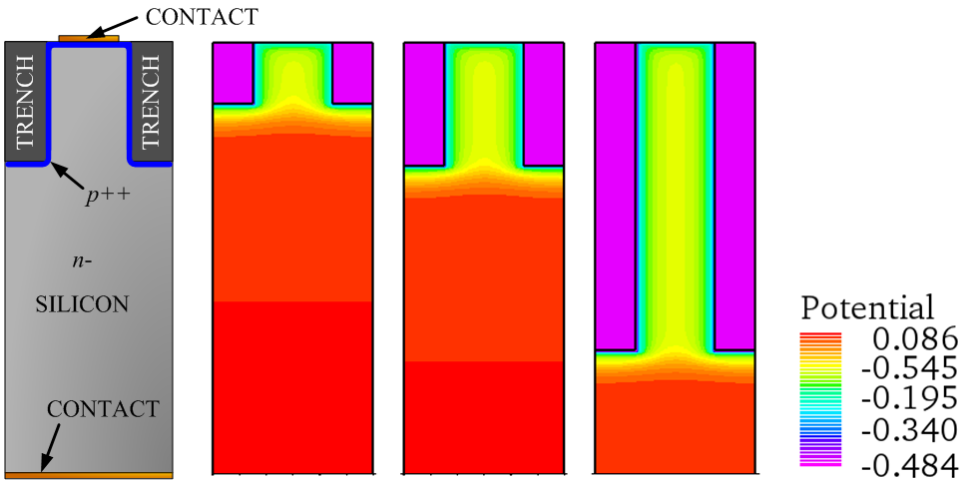

Figure 5.12: *Potential distribution within in-hole diffused trenched structures 50, 100, and 250 microns deep at self bias.*

A solution was obtained for trench depths of 50, 100, and 250 microns, Fig. 5.12, as color maps of the potential distribution. In the color map, a fade from green to yellow between the trenches indicates a slight potential gradient between trenches in this self-bias configuration. The greatest gradient in the potential and similarly the greatest electric field appears below the trenches.

Another solution from the modeled geometry was obtained for a reverse bias of 2 volts, Fig. 5.13. With 2 volts applied, the potential gradient between the trenches has been lost. However, the gradient beneath the trenches has been extended downward toward the backside (bottom) contact. The flat potential profile between the trenches indicates that there is little electric field present to force signal charge to drift between the top and bottom electrodes.

In addition to these static solutions, the Silvaco software enables a time-dependent routine to be defined. A transient condition can simulate a single ionization event within the device. A cloud of charge was defined in each of the structures as a cylinder of electron-hole pairs 10 microns in diameter, 10 microns long, and located midway between the trenches at a distance of 45 microns from the top. The current experienced by the top electrode was

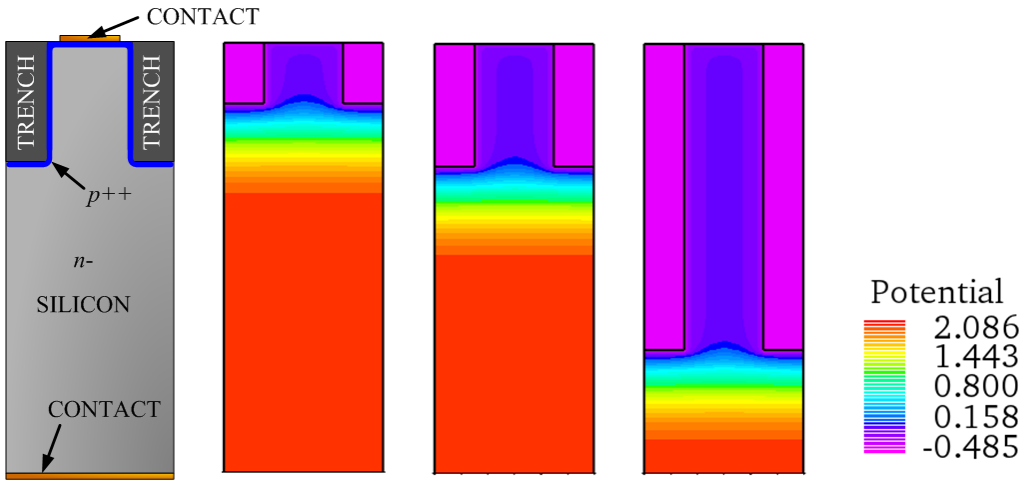

Figure 5.13: *Potential distribution within in-hole diffused trenched structures 50, 100, and 250 microns deep at 2 volts reverse bias.*

plotted as a function of time. The response is a current pulse, which was overlaid for each device configuration, Fig. 5.14.

The current pulse with 50 micron deep trenches is tall and narrow, shown in red. A relatively large current is observed for a short duration of time. The current has mostly dissipated within 0.5 microseconds after the event initially began. The 100 micron deep trenched structure shows a much shorter current pulse (green) stretched over a much longer duration of time. The peak current is roughly one-fourth that of the 50 micron trenched structure. The trend continues with the 250 micron deep trenched structure demonstrating much less peak current as well as a long duration of current beyond 8 microseconds.

In most detection systems the current signal output by the sensor is integrated by a charge-sensitive pre-amplifier circuit. The circuit is generally tuned for fast current pulses, much like the signal observed from the 50 micron deep trench simulation. Elongated current pulses resulting from deep trenched structures are poorly-matched to this signal processing equipment. As a result, only a fraction of the current pulse is integrated and smaller signals are output by the amplifier circuit. Smaller pulses cause pulse height spectrum features to move leftward, as was observed in the depth dependent neutron response plots, Fig. 5.11.

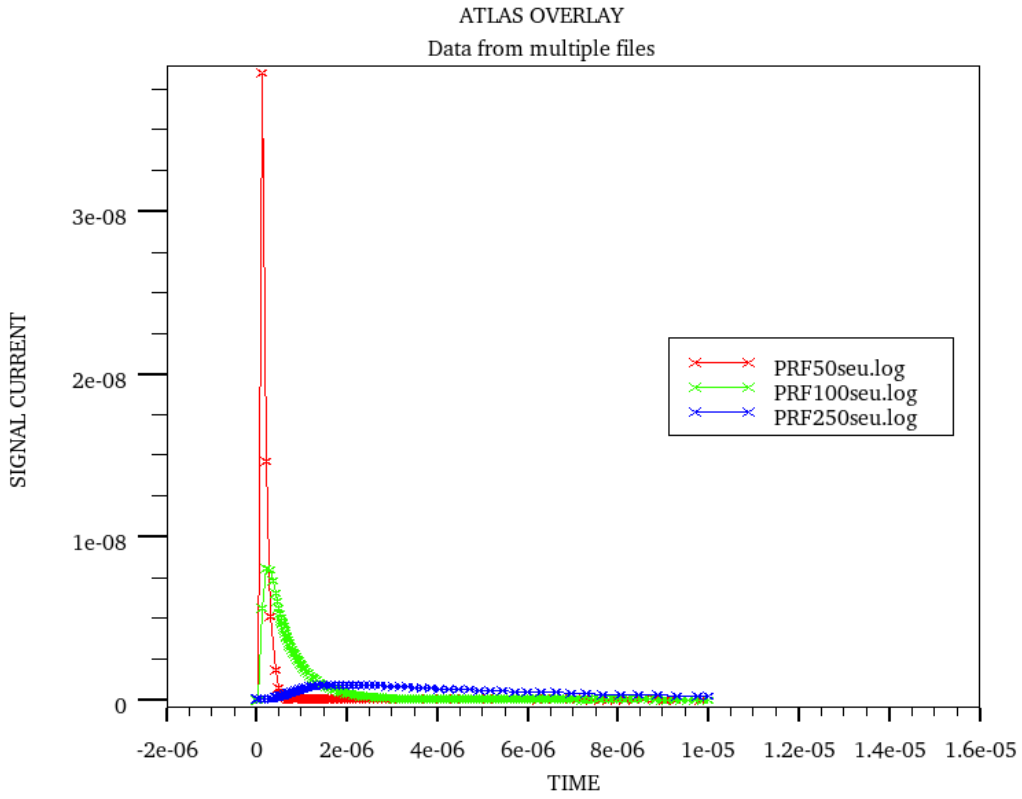

Figure 5.14: *Simulated current pulse induced on the top electrode, resulting from a single-event-upset of charge at a popular location between trenches having depth 50 (red), 100 (green), and 250 (blue).*

The long duration of the signal pulse from the 250 micron deep trench structure can be attributed to the weak electric field established between the trenches. The simulated signal current, Fig. 5.14, indicates slower signal with greater aspect-ratio trenches. In the transient simulation, the charge cloud could be observed as a function of time. Several snapshots of the electron concentration in the structure were generated during a transient solution of the 250 micron deep trenched device, Fig. 5.15.

Characteristics in the time-reel support that the motion of signal charge is dominated by diffusion transport rather than drifting. The spreading, or growing, of the cloud indicates that the charges are likely redistributing themselves, transitioning from a higher concentration to a lower concentration. The second indication of diffusion dominating over drifting

is that the centroid of the charge cloud remained in the same place throughout the entire time-reel. The only significant drifting in this process takes place below the trenches, where there is a substantial electric field present. Charge is drifted swiftly, draining away from the cloud above.

The behavior of charge transport within the in-hole diffused device is unusual and is not desired for radiation counting sensors. Ideally, the entire cloud of charge should retain a tight formation and move as one unit from one electrode toward another. This provides the maximum current density by moving all of the charge in a single direction simultaneously. With the in-hole diffusion design only a small fraction of the signal charge is being drifted efficiently at any given time.

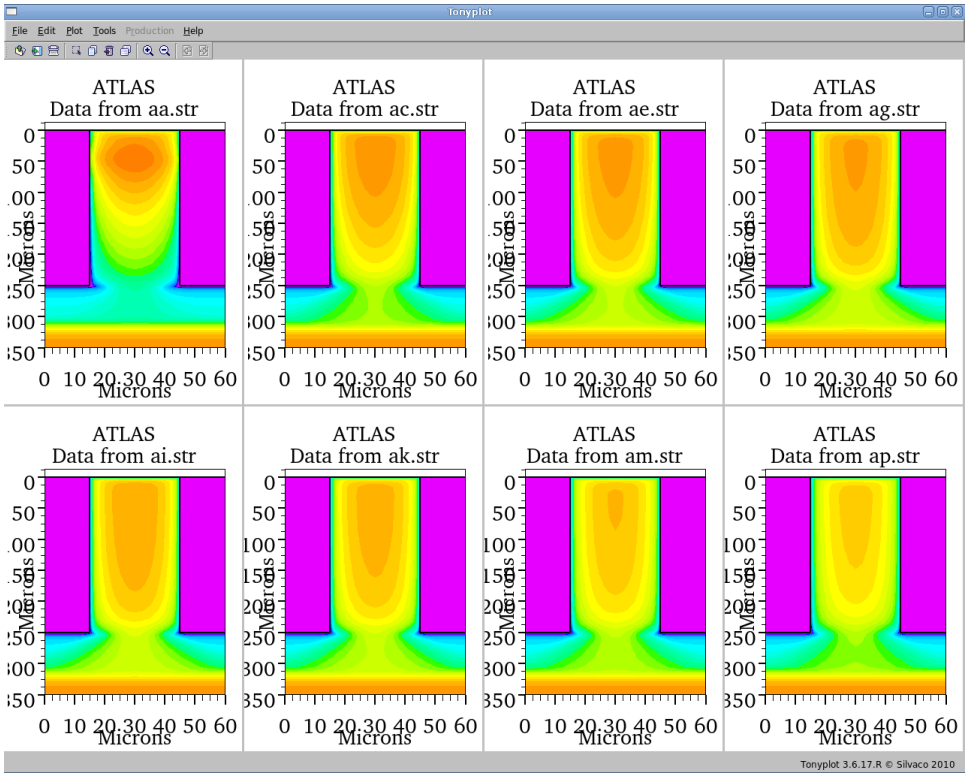

Figure 5.15: *Time-reel showing snapshots of electron concentration during the simulated signal pulse formation of figure 5.14 within the 250 micron trench geometry.*

5.3 Efficiency Testing

A Reuter Stokes ^{3}He coaxial proportional counter, 2 inches in diameter and 6 inches long was utilized as a standardized neutron sensor to which other sensors could be compared. The efficiency of the ^{3}He sensor, E_{He}, was determined experimentally to be 80.7%±0.50% through an attenuation experiment in the diffracted beam [25].

The diode neutron sensor efficiency was determined by comparing its thermal neutron counting response to the standard ^{3}He sensor. First, counts were collected from the ^{3}He detector mounted in the beam with and without a Cd shutter in the beam. Net counts N_{He} result from subtracting a Cd shutter response from the bare-beam response. Then a similar net response, N_{dev}, was gathered with the diode neutron sensor centered in the beam. With all collections taken over the same duration of time, the diode sensor efficiency was calculated with the simplified relation,

$$E_{dev} = E_{He} A_f \frac{N_{dev}}{N_{He}}, \tag{5.1}$$

where A_f is an area correction factor, beam area over sensor area ($A_f = 4.525$). This correction is necessary because the ^{3}He sensor was much larger than the beam, while the diode sensor was smaller than the beam.

5.3.1 Thin-film Coated Diode Efficiency

With a film thickness much less than the range of the charged particle reaction products in the conversion material, peaks form in the pulse height spectrum with little interference from noise or LLD settings. Thus, the thin-film design can be expected to closely follow theory in thermal neutron counting efficiency.

The efficiencies of several thin film devices were experimentally measured and compared to calculated theoretical values [3]. Table 5.1 shows that the experimentally obtained values closely correlate to theoretical predictions. Over a wide range of film thickness, the worst correlation of the three sensors was within 13% of the theoretical calculation. Similar find-

Thickness	Converter	Measured Eff. (%)	Theoretical Eff. (%)
450 (Å)	^{10}B	0.101±0.0006	0.116
18 (μm)	^{6}LiF	3.75±0.034	3.99
27 (μm)	^{6}LiF	4.19±0.032	4.3

Table 5.1: *Measured and theoretical intrinsic neutron counting efficiency from various thin-film detectors fabricated with the methods described in Chapter 3.*

ings have been reported in the literature [23, 25]. It is important to note that the measured efficiency was less than the theoretical prediction in all cases. The theoretical efficiency is an optimum case, and fabricated devices should be expected to perform slightly worse in a realistic scenario.

5.3.2 Perforated Diode Efficiency

The efficiency of perforated diode sensors was determined with the same method as for film coated sensors. Perforated sensors were tested with hole, straight-trench, and sinusoidal trench patterns having various depths. Both in-hole oxidation and in-hole diffusion device designs were considered.

In-hole Oxidized Sensors

Table 5.2 shows a variety of perforated diode devices fabricated with the in-hole oxidation process. Within the data set there is a fair comparison between the hole, straight-trench, and sinusoid-trench designs, all having a similar depth of 200 microns. At 16.2%, the sinusoid trench design offers roughly 1.3 times more neutron counting efficiency over the straight trench design, at 12.6%. Similarly, the straight trench outperforms the hole pattern design by a factor of 1.3. In the table, theoretical efficiency is also provided for each geometry. This theoretical efficiency was simulated with the methods in Chapter 2.4.

Trends in the data are clearer in a bar graph representation, Fig. 5.16. In all cases, as efficiency increases so does the margin between the measured and theoretical values. Recall from Fig. 5.11, the neutron response of the in-hole oxidized sensor was quite poor with trench

Design	Depth (μm)	Measured Eff.	Theoretical Eff.
Hole	22	0.049±0.009	0.056
Hole	200	0.097±0.004	0.119
Straight	200	0.126±0.006	0.204
Sinusoid	100	0.089±0.006	0.165
Sinusoid	200	0.162±0.009	0.250

Table 5.2: *Measured and theoretical intrinsic neutron counting efficiency from perforated neutron sensors implementing various trench patterns and fabricated with the in-hole oxidation method.*

depths of 100 microns. The spectrum shifted down toward the noise level with increasing depth. The hole-trenched design remains closer to theoretical performance than the other trench patterns and is likely due to the greater charged-particle capture probability.

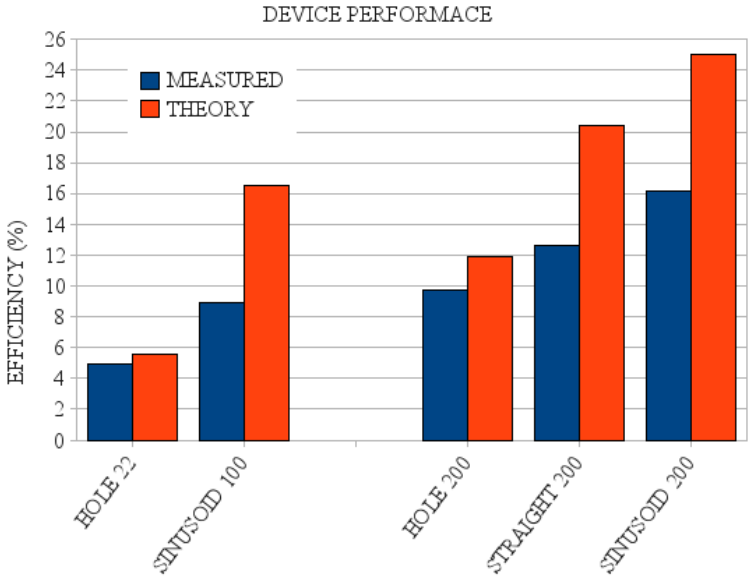

Figure 5.16: *Measured efficiency of various in-hole oxidized devices with theoretical values for comparison.*

Another trend is that the margin to theory becomes progressively worse from the hole design to the straight trench design, and furthermore to the sinusoid design. One characteristic difference between the designs that may support this trend is the surface area of the

trenches. The etched surfaces within the trenches are less pure than that of the bulk silicon material, resulting in greater leakage current and poor signal formation in the diode structure. Even with the surfaces passivated with silicon dioxide, the interface is of much poorer quality than the bulk material and is responsible less than ideal performance in neutron counting efficiency.

In-hole Diffused Sensors

The in-hole diffused devices showed better spectral response compared to the previous in-hole oxidized design, Section 5.2.4. By covering the surface damage of the trench walls with a conductive diffusion layer acting as an electrode, leakage current was substantially reduced. As a result, fabrication processes were more reliable and effective in producing operable devices with deeper trench structures.

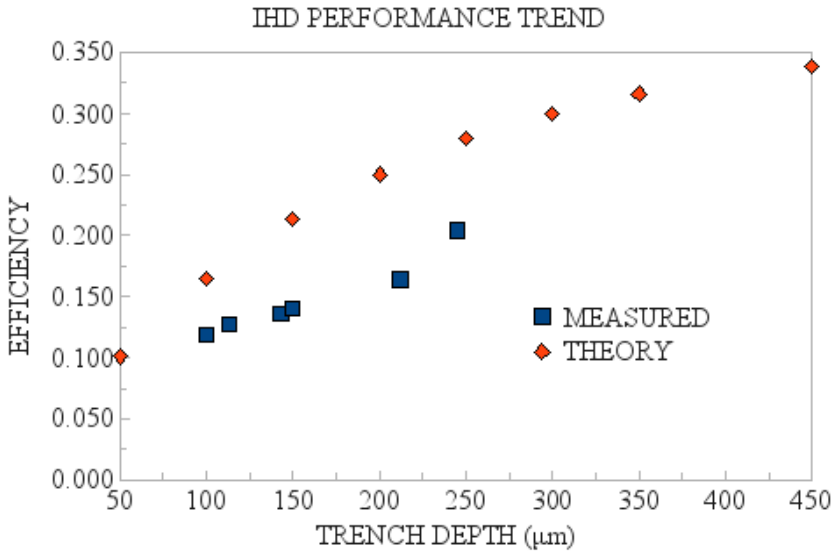

Figure 5.17: *Comparison of sinusoidal in-hole diffused (IHD) neutron sensor efficiency (blue) with theoretical efficiency values (red).*

To this date, devices with trench depths up to 245 microns have been made, resulting in a thermal neutron counting efficiency of 21% [26]. The measured efficiency of several in-hole diffused devices are plotted together to show the progression of efficiency with depth, Fig.

5.17. As depth increased from 100 microns to nearly 250 microns, the efficiency improved. However, the measured efficiency continues to fall short of the simulations of Section 2.4.2. In this case, with the in-hole diffused design, weak electric fields established between the trenches hinder efficient charge transport and poor signal formation reduces the neutron counting efficiency.

5.4 Gamma-Ray Response

A γ-ray source of ^{60}Co was obtained and placed within 0.5 cm of the face of a thin-film coated diode neutron sensor. A pulse height spectrum was collected from the sensor, Fig. 5.18, with the discriminator set to a low level to observe the smaller pulses that arrive closer to the noise floor. For direct comparison to the neutron response, a pulse height spectrum was collected in the diffracted neutron beam with the same settings.

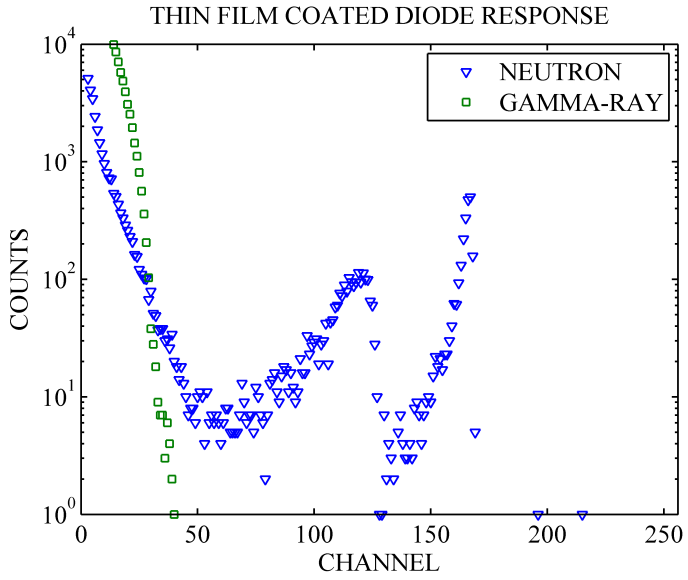

Figure 5.18: *Pulse height spectra resulting from γ-ray and neutron irradiation of a planar thin-film coated silicon diode neutron sensor.*

The pulses produced by γ-ray irradiation are much lower in magnitude than measured for the characteristic neutron induced peaks from alpha and triton particle reaction products.

Cobalt-60 emits a 1.173 and a 1.332 MeV γ ray for every disintegration [20]. The 2.05 MeV alpha particles produce pulses up to channel 120. However, γ rays carrying half the energy of the alpha particles produce pulses up to channel 40, roughly a third that of the alpha particles. The repressed pulse height of γ-ray events indicates that the maximum energy of the γ ray is not being efficiently converted into a signal pulse. These γ-ray signals will be easily discriminated by the LLD without the neutron response suffering greatly.

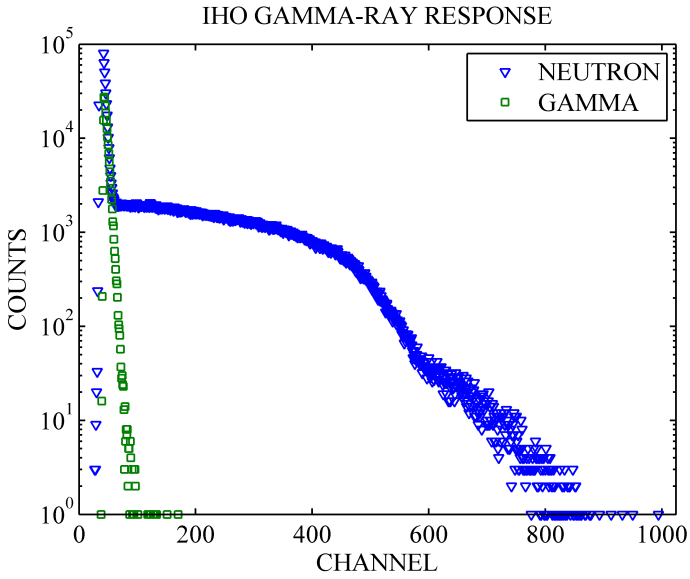

Figure 5.19: *Pulse height spectra resulting from γ-ray and neutron irradiation of an in-hole oxidized sinusoid patterned perforated neutron sensor, 100 microns deep.*

The same experiment was executed with an in-hole oxidized sinusoid patterned device having 100 micron deep trenches, Fig. 5.19. The resulting spectra show many neutron pulses extending to a soft ledge around channel 500. The γ-ray pulses, once again, are repressed to lower energy with significant counts appearing below channel 100. The low quality of neutron response with the in-hole oxidized device is less than ideal and raising the LLD to eliminate γ-ray counts comes at the expense of eliminating many neutron counts.

A neutron/gamma comparison was also executed for an in-hole diffused sinusoid patterned sensor, Fig. 5.20. The same repressed γ-ray response can be seen as with the in-hole

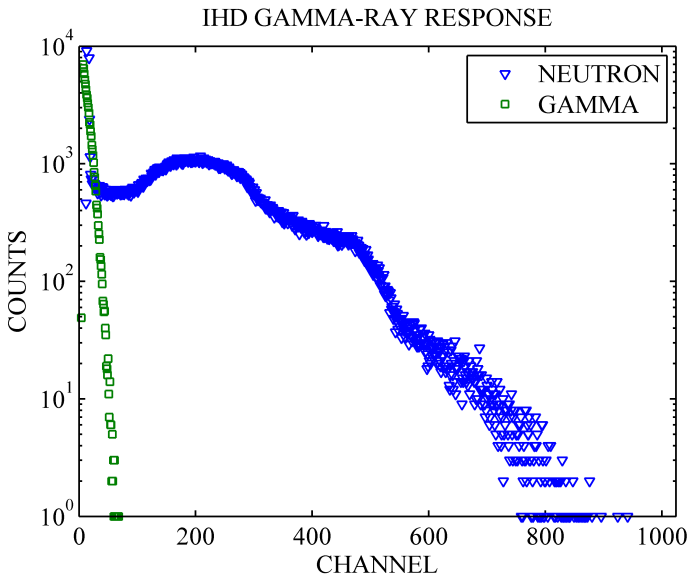

Figure 5.20: *Pulse height spectra resulting from γ-ray and neutron irradiation of an in-hole diffused sinusoid patterned perforated neutron sensor, 100 microns deep.*

oxidized device before. However, the improved neutron response offers more counts at higher energies. Unlike the in-hole oxidized device, the greatest counts per channel lie near channel 200. Those neutron counts below channel 100 are substantially less in number and the LLD can be raised with only a small detriment to neutron counts. With a conservative LLD setting of 500 keV, the γ-ray rejection ratio has been measured to be 1.6×10^7 γ's/neutron for this in-hole diffused sensor design [25].

Summary

Consider a thin-film device that utilizes ^{10}B as a conversion material instead of ^{6}LiF. The most probable charged particle reaction products in that case would be a 0.84 MeV ^{7}Li particle and a 1.47 MeV alpha particle. These are less than half the energies compared to the 2.05 MeV and 2.73 MeV reaction products from ^{6}Li as a neutron converter. Thus the neutron response would shift to lower energies and γ-ray rejection would be less effective.

There is much work ahead in this area to improve the signal formation process of the micro-structured diode. Theoretical analysis shows that there is room for improvement in

efficiency. If better signal is formed, the efficiencies of the perforated designs will approach theoretical predictions. The success in this work has resulted in a number of prototype systems varying from battery-powered pager-sized detectors, to fine-resolution pixel array systems. The latter is described in the next chapter.

Chapter 6

1-D Fine-Resolution Pixel Array

The potential for perforated diode neutron detectors to be small, yet efficient, drew interest from a research group at the Spallation Neutron Source (SNS) facility at Oak Ridge National Laboratory (ORNL). There was desire to install a high-resolution pixel array in a small-angle neutron scattering beam-line. Through a grant from the National Science Foundation, a custom 1-dimensional array of perforated diode neutron detectors was developed for neutron scattering measurements. The work became a collaborative effort between Kansas State University, University of Tennessee, and Oak Ridge National Laboratory.

Kansas State University took responsibility for creating the neutron sensor array with a set of desired performance characteristics. The University of Tennessee was employed to design custom signal amplifiers for the sensor array. Oak Ridge National Laboratory provided the data acquisition instrumentation. Lastly, within Kansas State University, the Electronics Design Laboratory (EDL) managed system integration and assembly as well as development of a user interface for the entire system.

Generally in scattering experiments the goal is to determine or monitor the distribution of radiation intensity scattered off of a test specimen or target, Fig. 6.1. Small angle neutron scattering (SANS) is a specific method with several uses ranging from measuring crystalline material properties to non-destructive stress measurement. Only scattering or diffraction along one dimension was of interest. Thus, a 1-dimensional array of detectors in the form of long straight pixels was designed.

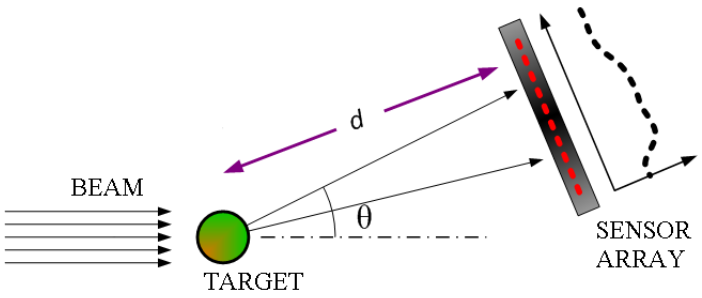

Figure 6.1: *A generalized small-angle neutron scattering experiment with a beam incident on a target and the resulting distribution of counts on a pixellated sensor array.*

One of the design constraints for this neutron sensor array was sub-millimeter spatial resolution. Resolution near 1 millimeter and slightly greater is achieved on a regular basis with multi-anode wire gas detector assemblies. Solid state sensors have the advantage of greater neutron absorption over gas-filled sensors, due to the greater atomic density of the solid material. In addition, the neutron reaction products have a short penetration distance in the solid sensor material.

6.1 Pixel Design

The mask pattern designed for the perforated diode pixel array is shown in Fig. 6.2. A narrow diode structure outlines a trench to form each pixel. To provide good electrical contact to a pixel, a metal layer was patterned on top of the diffusion layer that defines the diode. In addition, large metallic pads were created extending from the end of the pixels to provide adequate area for probing the pixels in testing and wire bonding for permanent assembly.

With such a tight array of pixels, bonding pads alternate to each end of a pixel. This design doubles the space available between pads and allows the pads to be larger than the width of a pixel. The 1000 pixels were not fabricated onto a single silicon chip. The specified design constraint for the total size was 4 cm long pixels spanning across 10 cm. The rectangular area of the array is too large to fit on the 3-inch silicon wafers processed

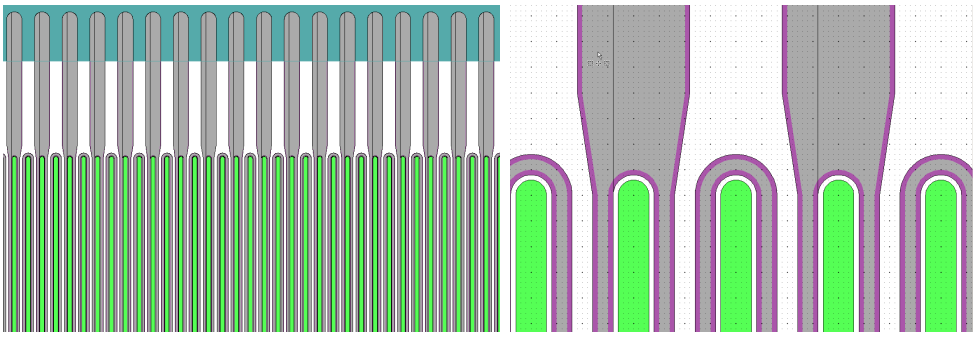

(a) Pixel layout. (b) Close-up view.

Figure 6.2: *Pixel layout in L-edit software for photomask design. Includes layers for the trench pattern (green), diffusion pattern (purple), and metal pattern (grey).*

in the SMART laboratory. Regardless, it becomes much more reliable to produce smaller chips with fewer numbers of pixels so that a single pixel failure does not ruin the entire array. A conservative number of pixels were patterned on several die so that several chips could be tiled together to make up the entire array. The first detector chips contained 32 pixels each. Later the number of pixels per chip was increased to 64.

6.2 Sensor Array Development

The fabrication process for the pixel array was no different than the in-hole oxidation process mentioned earlier in Section 3.4.1. However the pixel fabrication was more difficult to execute. Metallic contacts running down the full length of the pixels were only ten microns wide and required alignment tolerance of only 5 microns. The resist bridging technique combined with a lift-off process required thick resist and was difficult to perform reliably over the trenched features. With much attention to photolithography and several attempts for each wafer, the fine pixel structures were successfully fabricated, Fig. 6.3.

A critical feature was the buffer spacing between the trench sidewalls and the diffusion layer. Under high magnification, Fig. 6.4, it is clear that good alignment and photolithography work was done. The masking oxide layer appears in yellow in the figure while the

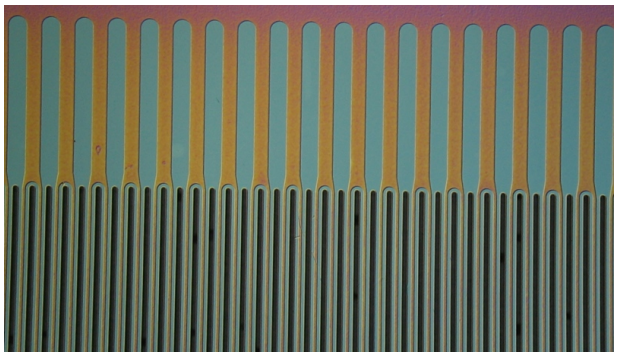

Figure 6.3: *The resulting diode array fabricated, before applying the conversion material.*

diffusion window is blue-green. Uniform buffer spacing exists around the entire trench and is implemented to reduce leakage current.

Figure 6.4: *Close-up view of the diode array showing the buffer space between the trench (black) and the diffusion layer (blue-green).*

For testing purposes a planar diode sensor array was also fabricated. The planar diode pixels were patterned and fabricated just as the perforated array, except trenches were not etched. Lastly, a coating of ^{6}LiF was evaporated over the diode pixels to make a thin-film coated diode neutron sensor array. Once fabrication was complete, leakage current and alpha particle testing took place.

Individual pixels were probed and tested for leakage current. Typical pixel I-V curves were plotted together for planar and perforated devices, Fig. 6.5. Leakage current is less than 100 nanoamps with a reverse bias under 8 volts for both the planar and perforated

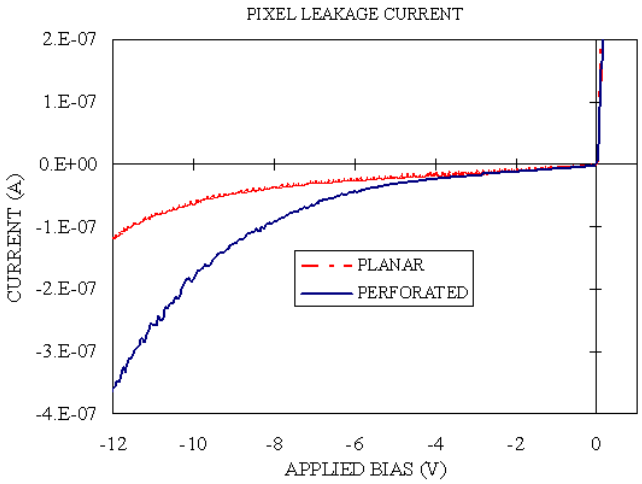

Figure 6.5: *Leakage current of a planar and perforated diode pixel.*

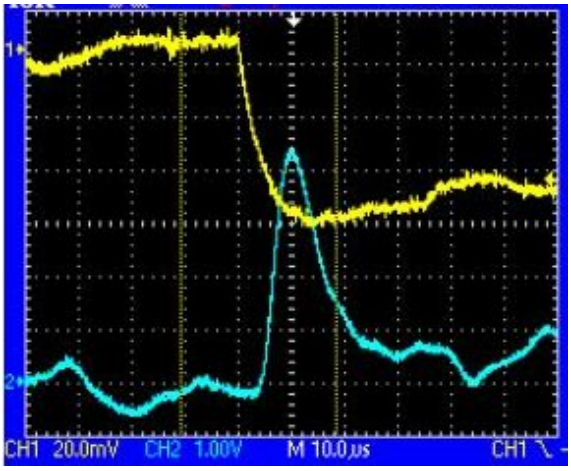

Figure 6.6: *An alpha particle pulse generated by a perforated diode pixel. Pre-amp signal is shown in yellow, while the shaping amplifier output is shown in blue*

diode pixels. The addition of deep trenches only increased leakage current slightly beyond the planar design.

With low leakage current confirmed, a test for alpha particle response was executed. A standard Ortec 142 preamplifier was connected to a single diode pixel. Then, an alpha particle source was placed on top of the chip and a signal pulse was captured, Fig. 6.6. The signal pulse was clearly above noise and showed effective particle detection.

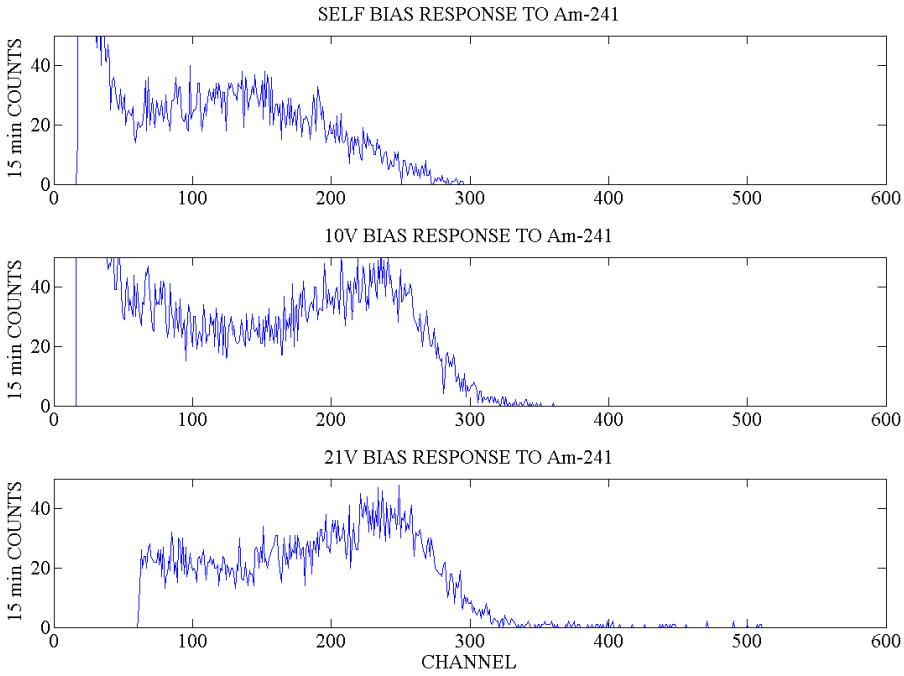

Figure 6.7: *Alpha particle spectral response of a perforated diode array at self-bias (top), 10 volts bias (middle), and 21 volts bias (bottom).*

To further confirm the expected behavior from incident alpha particles, pulse height spectra were collected during exposure to the alpha particle source. A few spectra were collected to show the change in response to applied reverse bias, Fig. 6.7. The spectrum did not demonstrate a sharp peak as what was produced from the perforated diodes before in Fig. 5.2. The broad peak should not be a surprise, as the lateral dimension of a single pixel is small. The small size of the pixel combined with the isotropic emission of a larger alpha source results in many particle near-misses at the boundaries of the sensor pixel and partial energy is deposited. With some particles depositing partial energy, the spectral peak is broadened and smeared toward lower channels.

Counts in the spectrum shifted toward the right as reverse bias was increased. The rightward shift is an indication that more energy is being converted into signal. Increased energy per particle capture could result from increasing the depletion region in the device or by establishing greater electric fields that move charge more efficiently. In any case a

rightward shift in the pulse height spectrum is common behavior in a diode radiation sensor and parallels what was demonstrated with sensor testing earlier, Fig. 5.9.

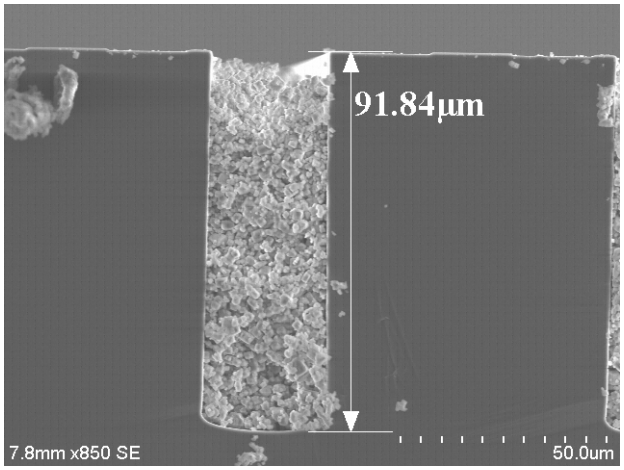

Figure 6.8: *A trench in the pixel array wafer, filled with ^{6}LiF and measured for depth.*

After confirming particle response, the trenches were filled with ^{6}LiF for neutron sensitivity. A scanning electron microscope image of a cleaved device, Fig. 6.8, shows trenches packed effectively with ^{6}LiF powder. Also, the depths of the trenches were measured to be 92 microns.

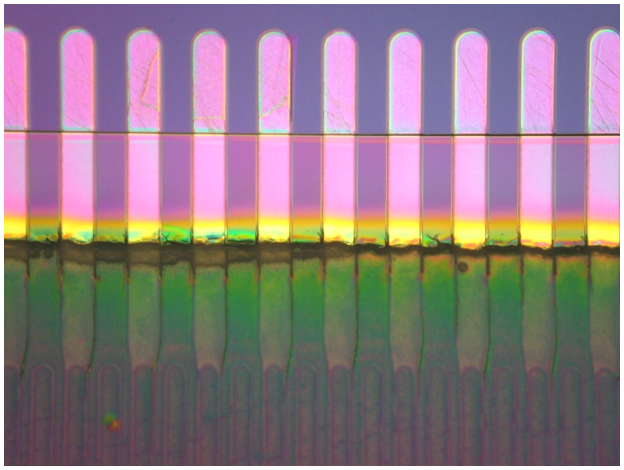

Figure 6.9: *A pixel array chip viewed under an optical microscope. The ^{6}LiF film is visible (green) as well as the thin encapsulating film (transparent) on top of the diode structures.*

In addition to trench filling, the detector array was also capped with an evaporated ^{6}LiF film and was encapsulated for protection from the environment. Fig. 6.9 shows a close-up view of a pixel array chip after fabrication. The film of ^{6}LiF halts at the end of the trenches and is translucent under the optical microscope. The encapsulating film is mostly transparent and has a distinct line where it was masked from the bonding pads. The pads must remain exposed so that electrical connections can be made via probing or wire-bonding.

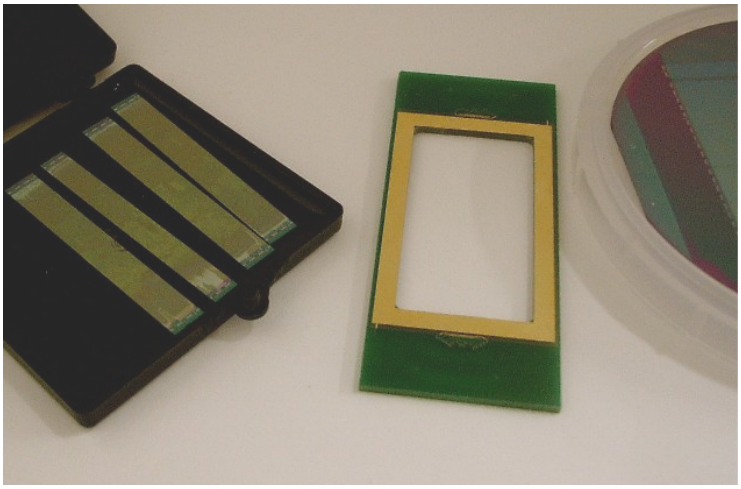

Figure 6.10: *32-pixel chips and the daughter card.*

Chips were diced out of the wafer such that 32 pixels remained intact. The sensor array chip was then mounted on a small circuit board, or daughter card, Fig. 6.10. Wirebonds were used to make connections to the circuit board from the sensor chip. Finally, an insulating epoxy was applied to protect the small and fragile wirebonds. The daughter card utilizes rigid connectors that allow the array chip to snap into place on a larger circuit board that will house signal processing circuitry. This motherboard processes information from the sensor pixels and translates it to a PC for data interpretation.

6.3 System Design and Development

With fine-pitched arrays, the only feasible method to pack signal processing circuitry into a reasonable space is to utilize an application specific integrated chip (ASIC). A custom chip was designed with microscopic amplifier circuits fabricated through CMOS processes.

6.3.1 Amplifier Circuitry

The amplifier chip for the perforated diode pixel array was designed by a research group at the University of Tennessee. The development took place in a three stage process. First a 16-channel prototype was made to prove the design and the capability of the fabrication house contracted by the group. The second stage in development was then scaled to, a more practical, 32 channels. The final stage was to produce a 64-channel chip.

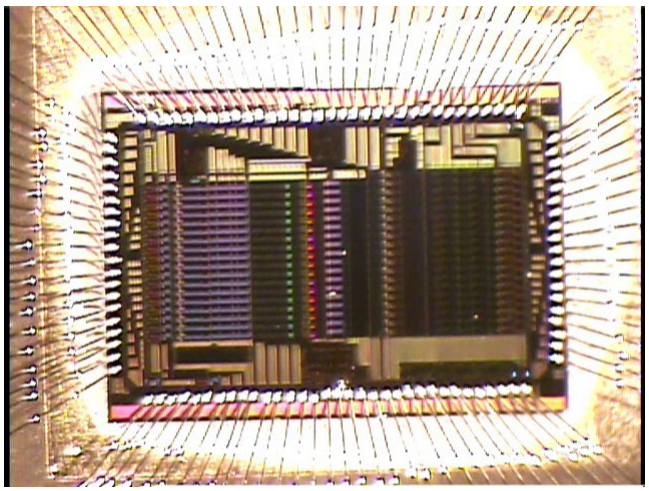

Figure 6.11: *The Patara ASIC amplifier chip.*

The ASIC was named "Patara" by the Tennessee group. A TSMC level IC fabrication process was utilized with 0.35 micron technology. The chip was designed to act as a preamplifier, pulse shaper, and a baseline restorer on the analog signal. Figure 6.11 shows one of the chips produced with the Patara design. Results from the first Patara testing were reported at an IEEE conference in 2006 [27].

As an amplifier for each channel, the chip has many features, including adjustable gain, polarity, and leakage current compensation. Though the chip was designed specifically for this project, it is a versatile component that could be used for other sensor designs in the future and for a wide range of applications.

A number of Patara chips were mounted on small circuit boards, Fig. 6.12, by the EDL at Kansas State University. As with the neutron sensor daughter card, connectors on the Patara board allow for the amplifier chips to be installed and removed easily. This not only makes removal easy in the unlikely event of failure, but it also allows a single working chip to be relocated to test other parts of the system.

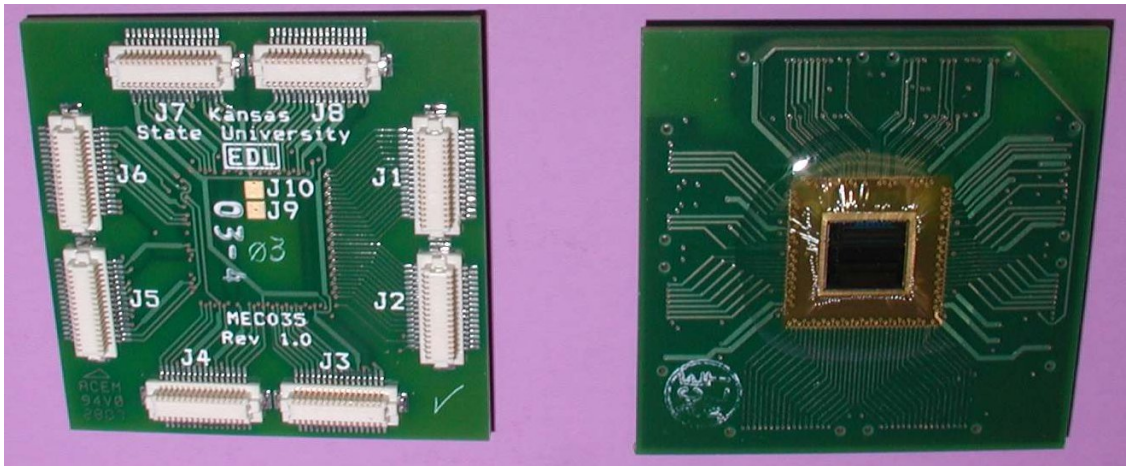

Figure 6.12: *Amplifier chip on a modular daughter board.*

After passing initial tests, the Patara design was modified and a second stage of development took place. Improvements on the Patara design were reported in a conference proceeding [28]. Also, a full description of the ASIC development process can be found in a master's thesis by Anthony Antonacci [29].

6.3.2 Signal Processing and Read-Out

The first generation of Patara offered analog signal amplification and output. The EDL then designed thresholding circuitry on the motherboard for each channel of output to digitize

the signal into convenient logic pulses. It is commonly necessary to convert an analog signal pulse into a square-wave logic pulse that is easily handled by digital electronic components, such as microcontrollers.

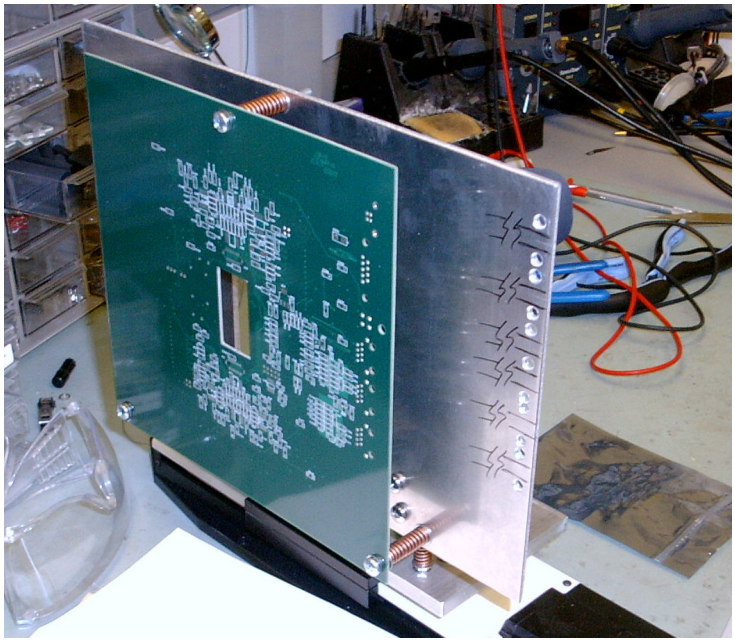

Figure 6.13: *The 32-channel pixel array system motherboard mounted on a precision translation stage.*

Digital pulses were counted within a set duration of time by outputting counts and time-stamp data to a PC data acquisition card. The information was sent from the motherboard, Fig. 6.13, to a computer through gigabit communications. Once the data was acquired with the PC, a LabView program allows the user to see a graphical output that includes total counts collected on each pixel over a set duration of time, and the count rate of each pixel, Fig. 6.14.

Communication back to the instrumentation was also established so a user could change the comparator thresholds and operating inputs for the Patara chips. A function for saving the data in tabulated form was also programmed into the interface software. It was then easy for data to be transferred to another personal computer to be analyzed and formatted for publishing results.

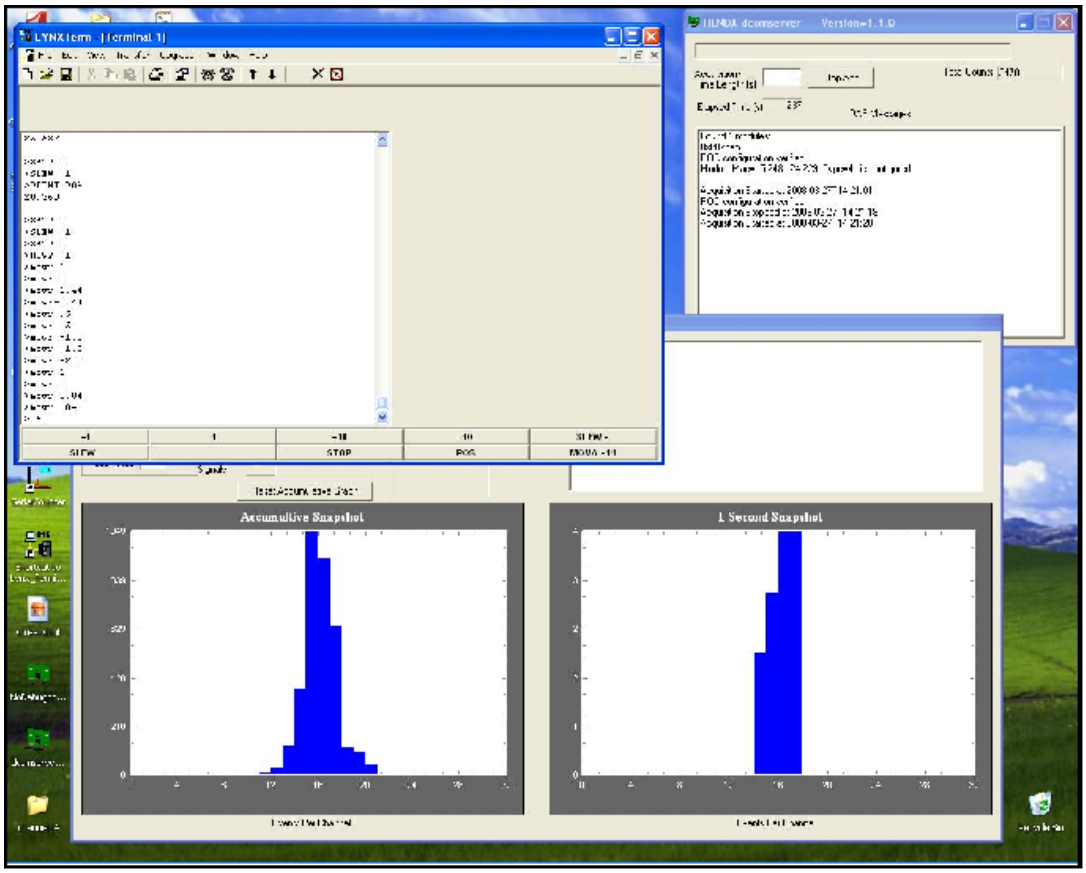

Figure 6.14: *Screenshot of the LabView user interface on the PC.*

6.4 System Performance

Diagnostic testing was performed at the EDL including feeding test signals to the input of the amplifier chips while mounted to the motherboard and checking the output of the user interface. The neutron sensor was then installed finalizing a complete prototype 32-channel array system. This prototype underwent testing for neutron response as well as spatial resolution to prove functionality before a larger 1024-pixel array system was developed.

6.4.1 Neutron Response

A temporary lead was attached to the output of one channel of the amplifier chip to view the analog pulse with an oscilloscope, Fig. 6.15. This was necessary because the system was

hard-wired to convert analog signal and communicate digital signals only to the PC. Signal pulses were captured while the sensor array was exposed to a neutron beam at the reactor facility at Kansas State University.

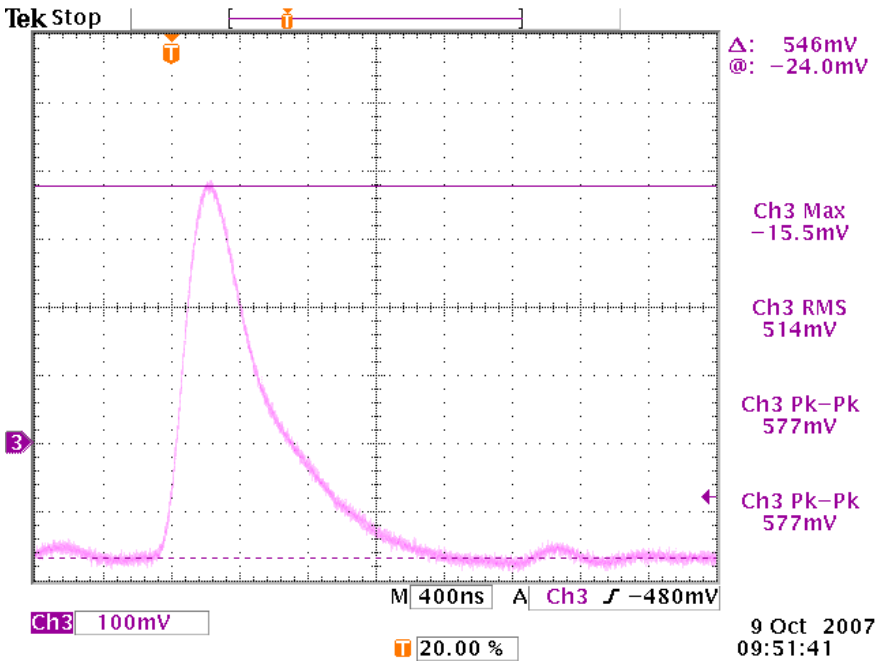

Figure 6.15: *Neutron signal response from a pixel in the 32-channel perforated neutron sensor array system.*

The neutron signal pulse height was greater than 0.5 volts and roughly 1.2 microseconds wide at the base. The pulse height, as well as the low level of noise shown, was easy to work with regarding threshold circuitry. Also, the pulse width was narrow enough to offer a potential for high counting rates exceeding 1×10^5 counts per second. High counting rates are also an advantage of a solid state detector design over gas-filled detectors. From this single pulse capture, it was clear that the amplifier chip was functioning well with the perforated diode sensor.

6.4.2 Spatial Resolution

The spatial resolution of the 32-channel prototype was measured by analyzing the array response to an abrupt edge (knife edge) in the neutron beam. The knife edge was a gadolinium foil produced with a straight edge by evaporating the material over a mask on a silicon wafer. With the mask removed, the gadolinium film covered half of the wafer with a straight edge down the middle. The film was then peeled off and the wafer was cleaved to provide a straight edge. The film was re-applied to the wafer such that the straight edge of the film overhung from the straight edge of the wafer. The wafer provided rigid support for the film. The assembly was mounted in front of the array on a micro-positioning tilting stage so that it could be aligned to the pixels on the array.

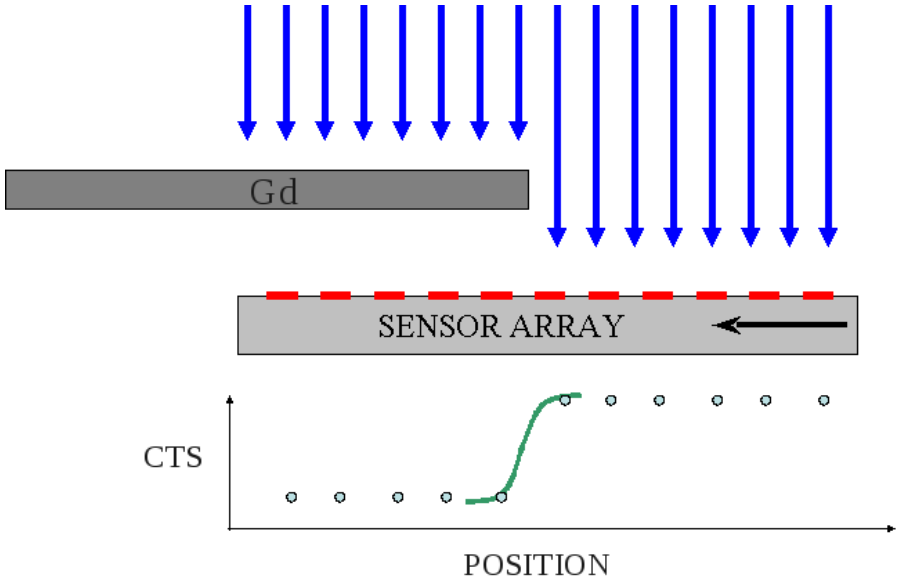

Figure 6.16: *Spatial response experiment.*

Once the foil edge was aligned with the array in the neutron beam, the array was translated at fixed increments of 25 microns across several pixels. Counts were collected for a fixed duration of time at each position interval, Fig. 6.16. The response was tracked as pixels transitioned from full beam exposure to full coverage by the absorber. The edge response in this type of situation generally follows an error-function distribution, the integral of a

Gaussian distribution. The full-width half-maximum (FWHM) of that Gaussian distribution is widely accepted as a metric for spatial resolution. A relatively small FWHM indicates fine resolution.

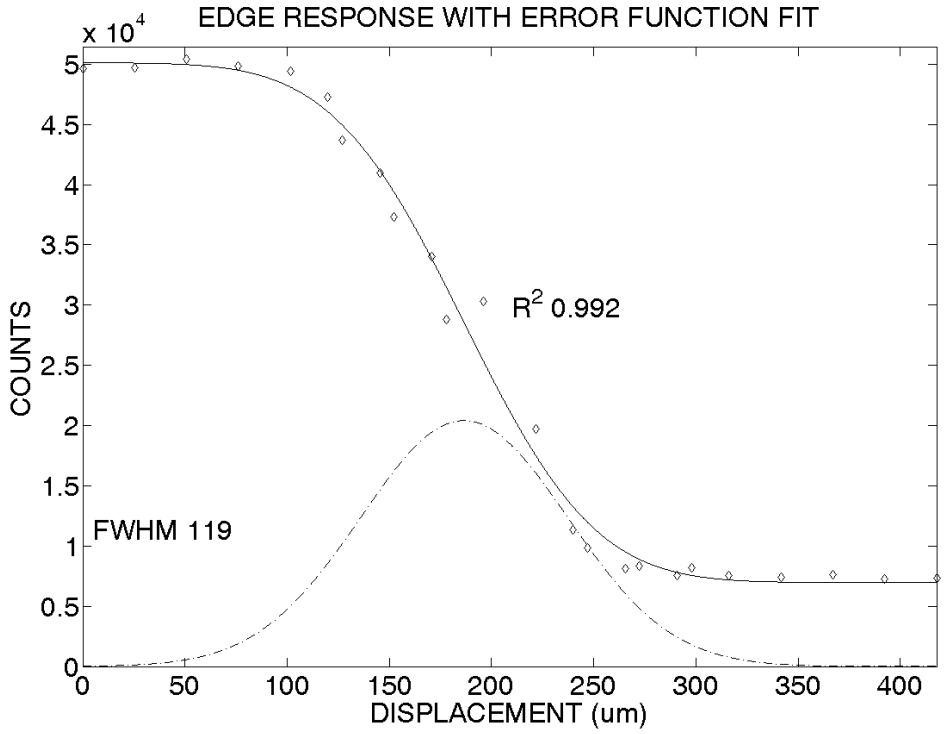

Figure 6.17: *Spatial response to translating the knife edge across the perforated diode pixel array.*

An error function curve was fit to the data collected in the knife edge experiment, Fig. 6.17, requiring a scaling parameter in the horizontal and vertical direction. The acquired data fit the error function profile well, as indicated by an R-squared value of 0.992. The derivative of the fitted function produced a corresponding Gaussian distribution. The full-width half-maximum of that profile was then determined to be 119 microns.

The spatial resolution experiment performed with a long knife edge has the potential for error on the greater side of the resolution. Alignment of a 4 centimeter long edge over pixels that are 100 microns wide is difficult and misalignment will result in a spreading of the edge over the array.

6.4.3 Practical Demonstration

The prototype array was demonstrated at the high flux isotope reactor (HFIR) at Oak Ridge National Laboratory (ORNL), Fig. 6.18. The demonstration further characterized the instrument and introduced the instrument to the end users.

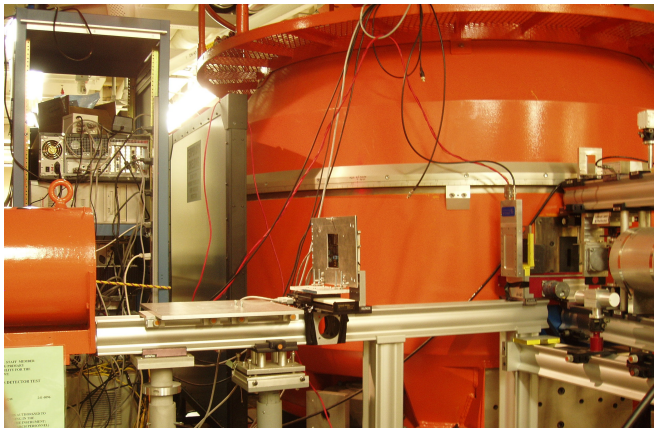

Figure 6.18: *Instrumentation at the HFIR beam line.*

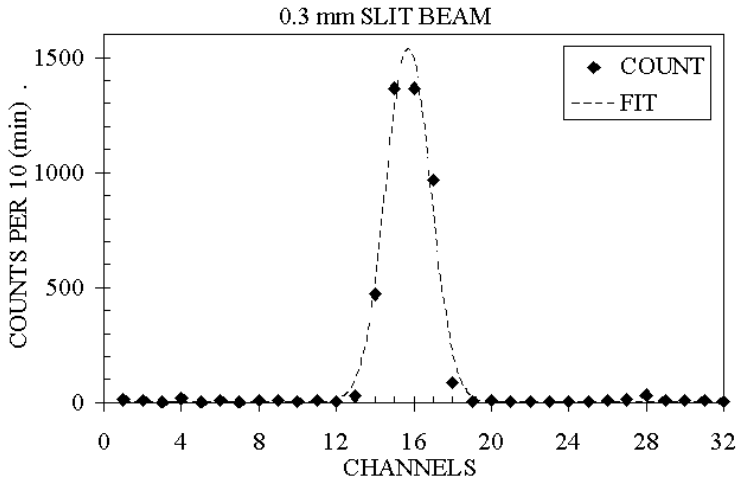

Figure 6.19: *32-channel perforated pixel array resolving a 300 micron slit.*

At the HFIR, the instrument was tested for response to a 300 micron wide slit-beam. A thin sheet of beryllium was sandwiched between two blocks of neutron absorbing material

to form a long and thin transparent window for neutrons. The neutron beam then took the form of a long slice 300 microns in width, roughly equivalent to a few sheets of paper.

Collecting counts on all 32 channels in this configuration, the pixel array very quickly responded by indicating significant counts on only four pixels, Fig. 6.19. The system accurately represented the beam dimensions and was efficient enough to warrant adding shielding around the beam to minimize response to background radiation.

Testing Summary

The results of this testing and demonstration show the successful operation of the 32-channel prototype system. It was concluded that all aspects of the system were functional including the perforated diode sensor chip, the custom amplifier ASIC, on-board signal processing electronics, and communications to the PC. The spatial resolution experiment quantified the performance of the array and documented the ability to resolve features nearly one-tenth of a millimeter [30]. The next step was then to copy this proven concept multiple times to form a much larger and more complex instrument with over 1000 channels.

6.5 1024-Channel Perforated Diode Array

Several improvements were considered for the 1024-channel system. The Patara was expanded to 64 channels on a single ASIC to reduce fan-out in the circuitry. The new version of the Patara also included thresholding and produced digital pulses for output rather than the analog signal. The neutron sensor chip design was also expanded from 32 pixels to 64 pixels per chip to reduce the number of duplicated chips across the array.

6.5.1 Chip Testing

Anticipating a large number of detector chips to be tested and a large number of pixels, a testing box was made that utilized two probing cards, Fig. 6.20(a). These cards have 32 probes with a spacing that is matched to the bonding pads on the detector chip. Probing 32 pixels from each end, all pixels on the chip were accounted for. A set of high voltage

barrel switches allowed solid electrical connections to be made between a selected pixel and a single feed-through to an Ortec 142 preamplifier.

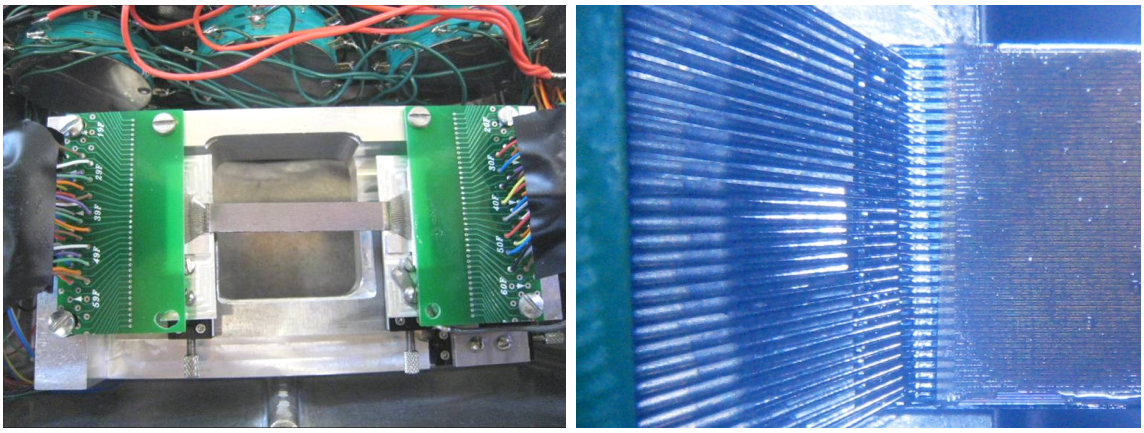

(a) The testing box for a 64-pixel chip.

(b) Close-up of 32 probe tips.

Figure 6.20: *Probe cards protrude from left and right over the bonding pads of the chip. Also, the high-voltage barrel switches can be seen at the top (left). Tips extending from a probe card over the bonding pads at on end of a 64-channel perforated diode neutron sensor chip (right).*

Smaller bonding pads would have made probing difficult and would have required precision translation stages just to make contact to the chip. With the probe-card testing box, the chip could be aligned beneath the probes by rotating a small screwdriver while against the side of the chip. Alignment was easily confirmed by viewing the assembly under a stereo-zoom microscope, Fig. 6.20(b). Once aligned with the bonding pads the probes could be lowered into contact with the turn of a screw. The spring-like pressure provided by the numerous probe tips held the chip in place during the experiment and ensured a good mating contact between the metallized back-side of the chip and the base.

Once a chip was mounted, all 64 channels could be checked individually by connecting testing equipment to a BNC connector on the side of the test box. For leakage current measurements, a bias supply and current meter were employed. For neutron response, signal processing equipment included a 142A Ortec preamplifier, a lower level discriminator,

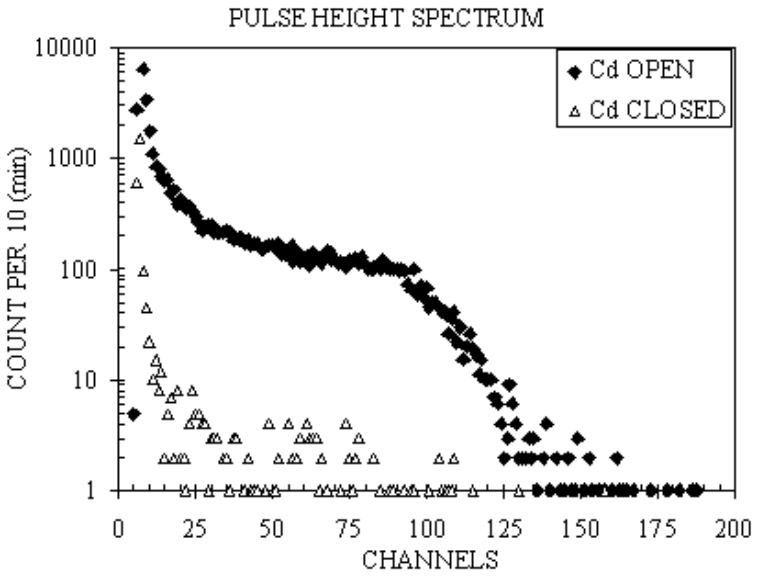

Figure 6.21: *Spectral neutron response of perforated pixel array.*

shaping amplifier, counter/timer, and a multi-channel analyzer for generating pulse height spectra.

Electrical connection to a pixel was made by selected appropriate dial positions on the test box. With a constant bias applied to the test specimen, leakage current could be monitored quickly as a go/no-go test by sweeping through the dial positions while viewing the current meter reading. Most of the chips that were fabricated passed this test and the chips with the lowest leakage current were selected to be installed on the sensor array daughterboard of the 1024-channel system.

A spectral response of a pixel to a neutron beam is shown in Figure 6.21, including a cadmium shutter response. The neutron response is characteristic of the in-hole oxidized device shown earlier, Fig. 5.7. It is clear that the sensor is capable of generating signal well above the noise floor.

Another experiment was performed to establish that most of the pixels were functional on the chip. The chip was placed roughly centered in a diffracted neutron beam collimated down to 3 mm. Afterwards, counts were collected from each pixel for a fixed duration of

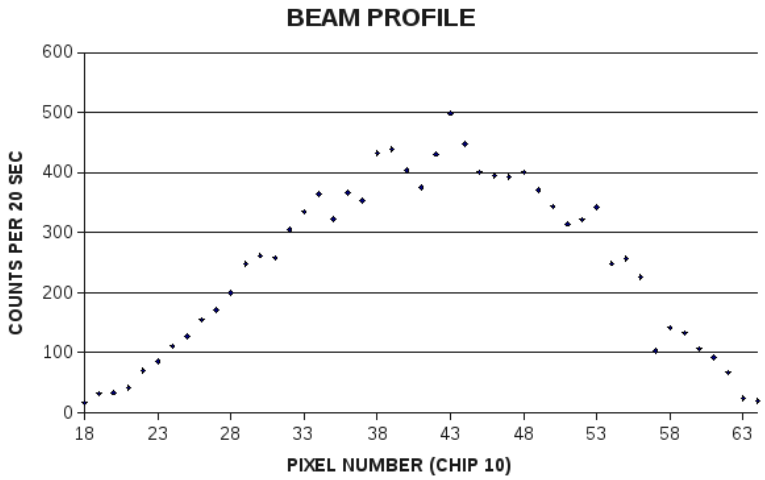

Figure 6.22: *Profile of a 3 mm diameter diffracted neutron beam produced by stepping through dial settings on the chip test box.*

time utilizing a counter/timer. The counts, when plotted as a function of pixel location, produced a 1-dimensional profile of the beam, Fig. 6.22.

The profile of the beam indicates that pixels 18 through 64 on the chip are behaving as expected. There is also some indication of the uniformity of the response across the chip. Some variation is expected depending on the packing fraction of the neutron conversion material, as well as small differences in the pixel and circuit electrical characteristics ahead of the preamplifier. More details on this work were published in a conference proceeding in 2009 [31].

6.5.2 1024-Channel System Design and Assembly

Sixteen of the best pixel chips were mounted to a circuit board, tiled side-by-side. The large neutron sensor daughter card is shown in Figure 6.23. Several rigid connectors were required to connect all of the pixels to the signal processing circuitry.

With so many wire bond connections, large bonding pads offer insurance against failing bonds. A simple scuff or spec of residue on the bonding pad can make bonding difficult or even impossible. If there is only room for one bond on the pad, then the likelihood for

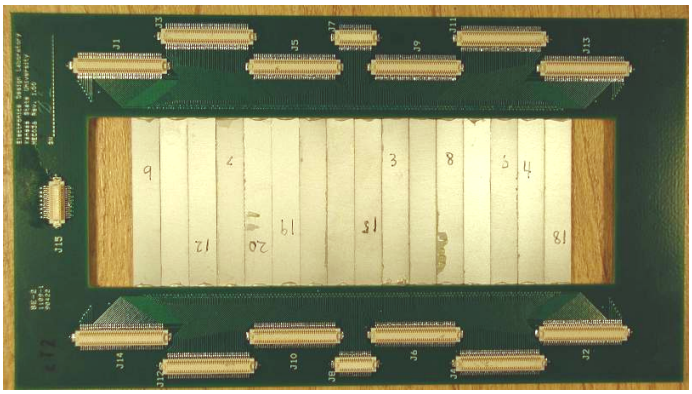

Figure 6.23: *Large perforated diode array daughter card.*

failure is high. On the other hand if the pad is much larger than the bond, Fig. 6.24, the bonder can reapply the connection on a different part of the pad.

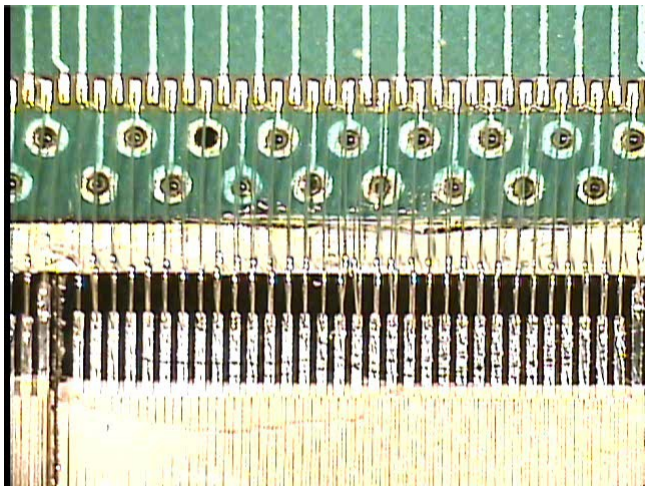

Figure 6.24: *Wire-bonds on the 1024 array.*

As with the 32-channel prototype, the 1024-channel sensor array board plugs into a large system board that directs pixel signals to the amplifier chips, Fig. 6.25. In addition the amplifier output is routed into microcontrollers that handle the digital signals and communicate information to the data acquisition card in the PC.

The sensor array board and the system board both have large windows cut out of them to minimize the amount of material present in the neutron beam. Scattered neutrons from

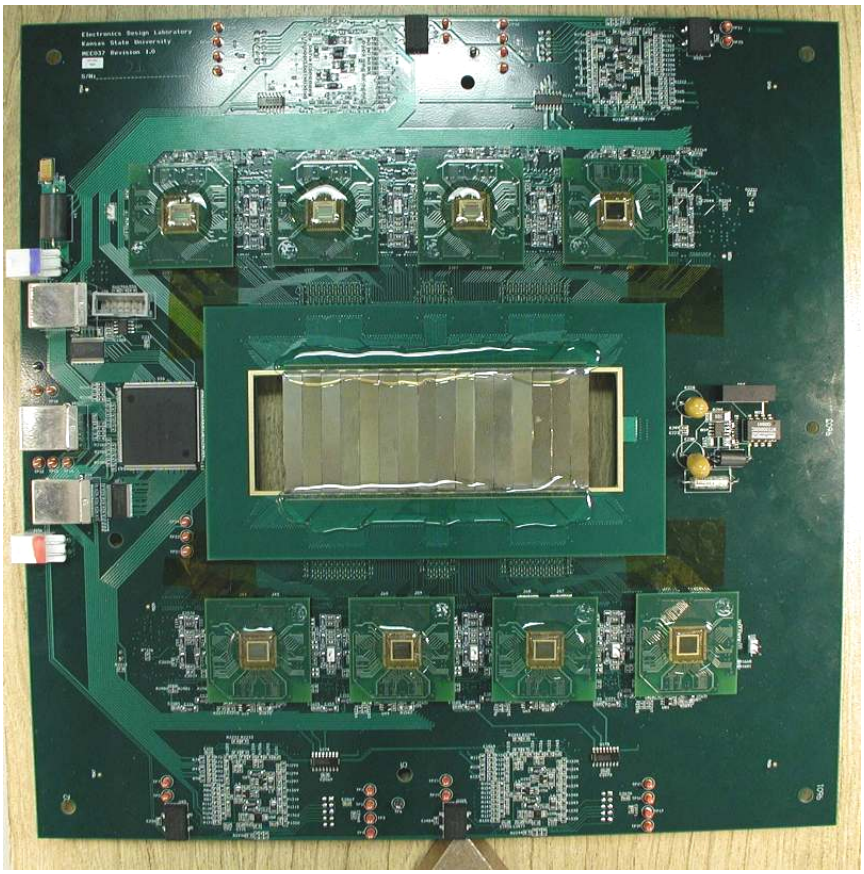

Figure 6.25: *1024-channel system board populated with the sensor card and amplifier boards.*

the foreign material increase the number of counts appearing in adjacent channels and will blur the data acquired by the array. Thus, it is a great advantage to ensure that only the neutron sensor is in the beam. With the diode neutron sensor design, less than half a millimeter of silicon and highly absorbing ^{6}LiF is present in the neutron beam. In addition to removing material from the path of the beam, the system board is laid out so that the electronic components are far from the neutron beam path to minimize exposure to damaging radiation and offer plenty of clearance for bulky shielding to be installed for protection.

On the front side of the system board the gigabit cable jacks can be seen on the left in Figure 6.25. Also a large microcontroller that handles the communications is present near the jacks. Eight Patara chips are visible on the front side of the system board, each on a

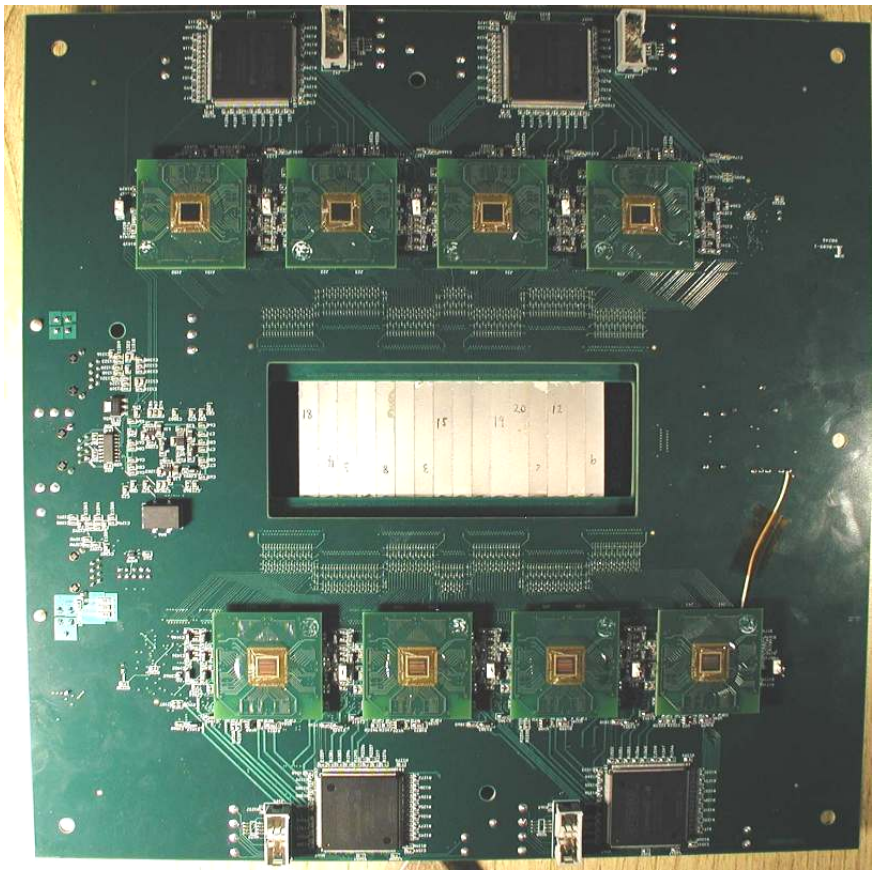

Figure 6.26: *1024-channel perforared diode array system backveiw.*

daughter board that plugs into the system board in modular fashion, like the sensor board.

On the backside of the system board shown in Figure 6.26, the other 8 amplifier chips are visible. There are 16 preamplifier chips total to handle 1024 signals from the detector pixels. The amplifier boards alternate to either side of the system board to conserve space. Also, on this side of the system, 2 large microcontrollers rest at the top and bottom. These controllers are responsible for time stamping the pulse arrivals, such that counting rates can be determined, and communicating data digitally. This information is sent from 4 controllers to a single controller where it is assembled into a single dataset that represents neutron counts over the entire 1024 array. Finally, it is communicated to the PC data acquisition card.

The same computer and software used in the 32-channel prototype was compatible with the 1024-channel system. The custom LabView program was simply expanded to include all of the channels as well as input values to control the settings of the second generation amplifier chips.

Sensor Array Summary

The development of the 1-D neutron detector array system progressed well with one exception. The final and most complex configuration of the amplifier chips came with some operational issues. Permanent failures were experienced with the chips and system testing has been postponed. Aside from this set-back in the latest configuration, the system retains great potential that has been proven with the 32-channel prototype. An efficient detection system with exceptional spatial resolution can be realized with the perforated diode neutron detector technology. In addition, there are many improvements that can be made in the design to provide better spatial resolution and more efficiency.

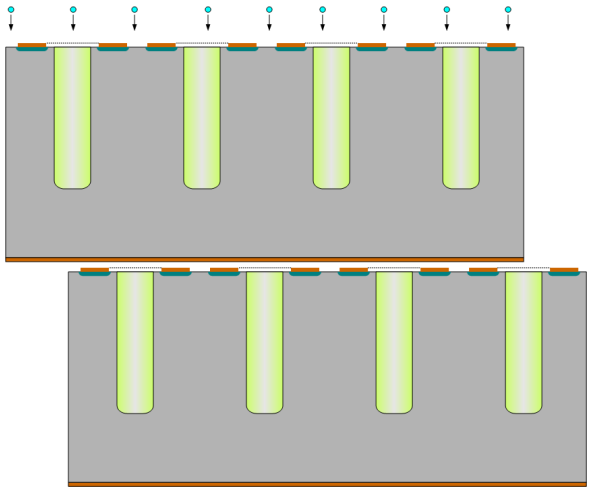

Figure 6.27: *Stacked and aligned perforated diode neutron sensor arrays.*

An obvious gain in efficiency can be achieved by pursuing deeper trenched structures. However, another improvement can be made utilizing a unique characteristic of the perforated neutron sensor design. Significant neutron streaming occurs between the trenches and

allows stacking of additional sensors to increase efficiency. Taking an identical perforated sensor array and placing it behind the original can double the efficiency, Fig. 6.27, if the back sensor perforations are offset to capture the neutrons streaming between the front sensor perforations. With stacking one has the choice of combining the front and back pixel counts for greater efficiency or to consider the back sensor array as additional pixels between the pixels of the front sensor, cutting the spatial resolution in half.

Chapter 7

Conclusion

The perforated diode neutron sensor design has proved to achieve nearly 5 times the thermal neutron counting efficiency of the common thin-film coated diode design. The challenge of maintaining low leakage current within the perforated diode structure was overcome with a selective diffusion fabrication technique and furthermore with an in-hole diffusion technique. Diffusing a shallow impurity layer into the trenches resulted in superior leakage current over the in-hole oxidation design.

Low leakage current allowed deeper perforations to be constructed while maintaining acceptable levels of electronic noise. Efficiency was shown to increase with deeper perforations. However, with deeper perforations, efficiency deviated farther from theoretical expectations. The shortcoming in efficiency was determined to be caused by a low electric field condition between the trenches within the in-hole diffusion design. The low electric field slowed signal formation and reduced signal magnitude, ultimately causing a loss of neutron counts. Substantial improvement in efficiency can be expected if work continues to address the low electric field problem.

The demand for smaller neutron sensors to achieve greater efficiency will prompt future work to explore deeper trenched structures, double-sided, and layered designs. In addition to intrinsic neutron counting efficiency, work must progress to investigate the limitations in sensitive area that can be achieved by a single diode device. Field instruments today use larger neutron sensors to gain better sensitivity than can be achieved with the diode sensors

presented in this work. If larger diode sensors cannot be made, multiple sensors must be grouped in an array to achieve acceptable sensitivity for a commercial instrument.

The perforated diode neutron sensor design has also proved to be adaptable to varying missions. In addition to the successful demonstration as a single sensor, a fine-resolution pixel array design was developed achieving sub-millimeter spatial resolution while maintaining neutron counting efficiency much greater than the thin-film coated diode design. Battery-powered prototype neutron detector systems have also been developed to this date by adapting perforated diode sensors to meet the need for compactness and ruggedness.

Bibliography

[1] D. Kramer, "DOE begins rationing helium-3," *Physics Today*, vol. 63, pp. 22–25, June 2010.

[2] R. V. Babcock, R. Davis, S. Ruby, K. Sun, and E. Wolley, "Coated semiconductor is tiny neutron detector," *Nucleonics*, vol. 17, pp. 116–122, April 1959.

[3] D. McGregor, M. Hammig, Y.-H. Yang, H. Gersch, and R. Klann, "Design considerations for thin film coated semiconductor thermal neutron detectors - i: Basics regarding alpha particle emitting neutron reactive films," *Nuclear Instruments and Methods in Physics Research, Section A*, vol. 500, pp. 272–308, November 2003.

[4] R. Muminov and L. Tsvang, "High-efficiency semiconductor thermal-neutron detectors," *Soviet Atomic Energy*, vol. 62, pp. 316–319, April 1987.

[5] S. Azimov, F. Mullagalieva, N. Sheina, and A. Yafasov, "High-efficiency semiconductor thermal-neutron detector," *Instruments and Experimental Techniques, New York*, vol. 28, pp. 782–784, July 1985.

[6] C. Allier, *Micromachined Si-Well Scintillator Pixel Detectors*. DUP Science, Delft University Press, The Netherlands, 2001.

[7] J. Schelten, M. Balzhsauser, F. Hsongesberg, and R. Reinartz, "New neutron detector development based on silicon semiconductor and ^{6}LiF converter," *Physica B: Condensed Matter*, vol. 234-236, pp. 1084–1086, June 1997.

[8] D. McGregor, R. Klann, H. Gersch, E. Ariesanti, J. Sanders, and B. VanDerElzen, "New surface morphology for low stress thin-film-coated thermal neutron detectors," *IEEE Transactions on Nuclear Science*, vol. 49, pp. 1999–2004, August 2002.

[9] C. Solomon, J. Shultis, and D. McGregor, "Angular design considerations for perforated semiconductor detectors," *IEEE Nuclear Science Symposium Conference Record*, November 2007.

[10] J. K. Shultis and D. S. McGregor, "Efficiencies of coated and perforated semiconductor neutron detectors," *IEEE Transactions on Nuclear Science*, vol. 53, pp. 1659–1665, June 2006.

[11] J. K. Shultis and D. S. McGregor, "Calculation of ion energy-deposition spectra in silicon, lithium-fluoride, boron, and boron carbide," Tech. Rep. 299, Kansas State University, Department of Mechanical and Nuclear Engineering, Manhattan, KS 66503, April 2007.

[12] J. Shultis and D. McGregor, "Designs for micro-structured semiconductor neutron detectors," *Poceedings of SPIE - The International Society for Optical Engineering*, vol. A 7079, August 2009.

[13] J. Shultis and D. McGregor, "Design and performance considerations for perforated semiconductor thermal-neutron detectors," *Nuclear Instruments and Methods in Physics Research*, vol. A 606, pp. 608–636, July 2009.

[14] W. Kern and D. Puotinen, "Cleaning solutions based on hydrogen peroxide for use in silicon semiconductor technology," *RCA Review*, vol. 31, pp. 187–206, June 1970.

[15] B. Rice, "Inductively coupled plasma etching of silicon and gallium arsenide," Master's thesis, Kansas State University, 2006.

[16] W. McNeil, S. Bellinger, T. Unruh, E. Patterson, J. Shultis, and D. McGregor, "Perforated diode fabrication for neutron detection," *IEEE Nuclear Science Symposium Conference Record*, vol. 6, pp. 3732–3735, November 2006.

[17] D. McGregor and R. Klann, "High-efficiency neutron detectors and methods of making same," *U.S. Patent*, no. 7164138, 2007.

[18] W. Sun, N. P. Kherani, K. D. Hirschman, L. L. Gadeken, and P. M. Fauchet, "A three-dimensional porous silicon p-n diode for betavoltaics and photovoltaics," *Advanced Materials*, vol. 17, pp. 1230–1233, May 2005.

[19] S. Bellinger, W. McNeil, and D. McGregor, "Improved fabrication technique for microstructured solid-state neutron detectors," *Materials Research Society Symposium Proceedings*, vol. 1164, pp. 57–65, April 2009.

[20] B. of Radiological Health, ed., *Radiological Health Handbook*. Washinton, D.C. 20402: Superintendent of Documents, U.S. Government Printing Office, January 1970. U.S. Department of Health, Education, and Welfare, Public Health Service, Food and Drug Administration, Rockville, Maryland 20852.

[21] J. R. Parrington, H. D. Knox, S. L. Breneman, E. M. Baum, and F. Feiner, eds., *Nuclides and Isotopes, Chart of the Nuclides*. GE Nuclear Energy, 175 Curtner Ave. M/C 948, San Jose, CA 95125-1088: General Electric Co. and KAPL, Inc., 15 ed., 1996.

[22] T. Unruh, "Development of a neutron diffraction system and neutron imaging system for beamport characterization," Master's thesis, Kansas State University, 2009.

[23] S. Bellinger, W. McNeil, T. Unruh, and D. McGregor, "Angular response of perforated silicon diode high efficiency neutron detectors," *IEEE Nuclear Science Symposium Conference Record*, vol. 3, pp. 1904–1907, October 2007.

[24] S. Bellinger, W. McNeil, T. Unruh, and D. McGregor, "Characteristics of 3d microstructured semiconductor high efficiency neutron detectors," *IEEE Transactions on Nuclear Science*, vol. 56, pp. 742–746, June 2009.

[25] D. McGregor, W. McNeil, S. Bellinger, T. Unruh, and J. Shultis, "Microstructured semiconductor neutron detectors," *Nuclear Instruments and Methods in Physics Research, Section A*, vol. 608, pp. 125–131, September 2009.

[26] S. Bellinger, W. McNeil, and D. McGregor, "Variant designs and characteristics of improved microstructured solid-state neutron detectors," *IEEE Nuclear Science Symposium Conference Record*, pp. 986–989, October 2009.

[27] J. Britton, S. Bunch, C. Britton Jr., B. Blalock, D. McGregor, and L. Crow, "Patara: Solid-state neutron detector readout electronics with pole-zero and complex shaping and gated baseline restorer for the sns," *IEEE Nuclear Science Symposium Conference Record*, vol. 1, pp. 27–31, 2007.

[28] A. Antonacci, J. Britton, S. Bunch, M. Ericson, B. Blalock, R. Chun, R. Greenwell, D. McGregor, L. Crow, L. Clonts, T. Sobering, R. Taylor, W. McNeil, S. Bellinger, and C. Britton Jr., "Patara ii: A 64-channel solid-state neutron detector readout system with integrated analog and digital processing for the sns," *IEEE Nuclear Science Symposium Conference Record*, pp. 68–74, October 2009.

[29] A. G. Antonacci, "A 64-channel mixed-signal data acquisition system for a solid-state high efficiency neutron detector array," Master's thesis, University of Tennessee, Knoxville, 2007.

[30] W. McNeil, S. Bellinger, B. Blalock, J. C.L. Britton, J. Britton, S. Bunch, S. Cowley, C. Henderson, T. Sobering, R. Taylor, and D. McGregor, "Preliminary tests of a high efficiency 1-D silicon pixel array for small angle neutron scattering," *IEEE Nuclear Science Symposium Conference Record*, vol. 3, pp. 2340–2342, October 2007.

[31] W. McNeil, S. Bellinger, T. Unruh, C. Henderson, P. Ugorowski, R. Taylor, B. Blalock, J. C.L. Britton, and D. McGregor, "1-D array of micro-structured neutron detectors," *IEEE Nuclear Science Symposium Conference Record*, pp. 2008–2011, October 2009.

Appendix A

Simulation Programs

A.1 Spectral Neutron Response with Thin-Film Geometry

This Matlab routine takes data interpolated from TRIM simulations describing ionization versus depth and applies it to the random tracks in the thin film geometry.

```
clear all; clc

% this program produces the spectra of a thin film device

load EDEPTRACK

% Range of particles in microns
R1=max(Tx); R2=max(Ax);

numD=2e2;    % number of depth locations to simulate
Dmax=36.4;     % maximum depth or film thickness 0.4 and 36.4
% depth of interaction from interface
D=Dmax/numD:Dmax/numD:Dmax;

% For Long range particle

% array of angles
numT=3e2;          % number of angles to consider for each depth
Textreme=acos(min(D)/R1);    % determine the maximum angle
Tstep=Textreme/numT;      % size of angle increment

L=0;     % start an array to build on
for i=1:1:numD
```

```
    if D(i) >= R1
        break
    end
    % max angle of interest
    thetaM=acos(D(i)/R1);
    theta=0:Tstep:thetaM;
    % array of lengths
    tmp=R1-(D(i)./(cos(theta)));
    L=cat(2,L,tmp);
    clear thetaM theta tmp
end
% look-up energy relationship to pathlength
EnT=interp1(Tx,TCE,L);

clear Textreme Tstep

L2=0;

% For Short range particle

% array of angles
Textreme=acos(min(D)/R2);
Tstep=Textreme/numT;

for i=1:1:numD
    if D(i) >= R2
        break
    end
    % max angle of interest
    thetaM=acos(D(i)/R2);
    theta=0:Tstep:thetaM;
    % array of lengths
    tmp=R2-(D(i)./(cos(theta)));
    L2=cat(2,L2,tmp);
    clear thetaM theta tmp
end

EnA=interp1(Ax,ACE,L2);

En=cat(2,EnT,EnA);

% Presenting the Data
```

```
C=0:R1/100:R1;
% figure(1);
% Tr=hist(L(:),C);
% Alf=hist(L2(:),C);
% plot(C,Tr,C,Alf)

% Plotting the output
% figure(2);
% hist(En,256);

[Sp,Ch]=hist(En,256);
tck=zeros(1,20);
Sp=cat(2,Sp,tck);
dch=Ch(2)-Ch(1);
tack=max(Ch)+dch:dch:max(Ch)+20*dch;
Ch=cat(2,Ch,tack);
SSp=smoothts(Sp, 'g', 45, 20);

%%
figure(3); hold on
%plot(Ch,SSp);
area(Ch,SSp);
title('THICK-FILM NEUTRON RESPONSE')
xlabel('ENERGY (MeV)')
ylabel('COUNTS')
```

This program generates the dataset interpolated from TRIM simulations.

```
clear all; clc;

load TRIMDATA.mat

dxAlpha=AlphaX(2)-AlphaX(1);


CF=2.050/(sum(AlphaE)*dxAlpha);
CAE=AlphaE*CF;
clear CF;

dxTrit=TritonX(2)-TritonX(1);

CF=2.730/(sum(TritonE)*dxTrit);
CTE=TritonE*CF;
```

```
find(CAE==0)
tmp=CAE(1:95);
AE=tmp(95:-1:1);
Ax=AlphaX(1:95);
clear tmp

find(CTE==0)
tmp=CTE(1:91);
TE=tmp(91:-1:1);
Tx=TritonX(1:91);

save EDEPDAT Ax AE Tx TE

plot(Ax,AE,Tx,TE)

ACE=cumsum(AE)*dxAlpha;
TCE=cumsum(TE)*dxTrit;
plot(Ax,ACE,Tx,TCE)

save EDEPTRACK Ax ACE Tx TCE
```

A.2 Charged Particle Capture with Hole Geometry

This Matlab routine simulates the attenuation of neutrons through a cylinder of ^{6}LiF conversion material and generates random secondary charged-particle tracks from the location of neutron interactions. Recording the termination points of the charged-particle tracks, the counting efficiency was approximated by counting the termination points that would be found outside of the cylinder.

```
clear all; clc
% MATERIAL PROPERTIES
sig=54.79;  % att.length 1/mean free path
n=1e3;      % number of events
R=15;       % radius of cylinder
harea=pi*R^2; lattice=60;
uarea=lattice^2;
L1=7.51; L2=43.3; % particle ranges
depth=100;    % initial depth for ruitine
%% NEUTRON ABSORPTION EVENT
```

```
ff=exp(-depth*sig/(10^4));
z=(10^4)*log((ff)+((1-ff)*rand(1,n)))/(-sig);
clear ff
%z=(10^4)*log(1-rand(1,n))/(-sig); % importance sampling on
    exponential
% importance sampling is simply the CDF with rand in for variable
r=R*sqrt(rand(1,n)); % sample radius
theta=2*pi*rand(1,n); % sample angle
x=r.*cos(theta);          % convert to rectangular coord for
    locating in 3space
y=r.*sin(theta);
%% CHARGE PARTICLE TRACK
phi=2*pi*rand(1,n); % sampled azimuthal angle
cai=pi*(rand(1,n)); % sampled polar angle
x2=L1*sin(cai).*cos(phi)+x;
y2=L1*sin(cai).*sin(phi)+y; %clear phi
z2=L1*cos(cai)+z;  %clear cai
x3=x+L2*(x-x2)/L1;
y3=y+L2*(y-y2)/L1;
z3=z+L2*(z-z2)/L1;
%% TRACK ENDS TO POLAR COORDS
r2=sqrt(x2.*x2+y2.*y2); % polar makes easy to check if out of
    cylinder
r3=sqrt(x3.*x3+y3.*y3);
%% SORTING ARRAYS
noabs=z<depth; % neutron not absorbed in LiF zero to eliminate
nocnt=(r2>R)|(r3>R)|(z2>depth)|(z3>depth);
CR=sum(noabs.*nocnt); clear nocnt noabs
clear CR
grid on
%% CIRCLE
 xc=-15:0.1:15;
 yc=sqrt(R*R-xc.*xc);
 zc=zeros(1,numel(xc));
 xrec=[0 0  0  0];
 yrec=[R R -R -R];
 zrec=[depth 0 0 depth];
%% PLOTS FROM HERE ONWARD
figure(1)
polar(theta,r,'.')
title('INTERACTION LOCATIONS');
%% depth of int
figure(2)
```

```
hist(z,10); title('DEPTH OF INTERACTION'); % show sampled
    distribution
xlabel('DEPTH (microns)');
ylabel('# OF INTERACTIONS');
%% graphical plot
%  A=cat(1,x2,x,x3); B=cat(1,y2,y,y3); C=cat(1,z2,z,z3);
%  figure(3)
%  plot3(x,y,z,'*',x2,y2,z2,'rs',x3,y3,z3,'gd',A,B,C,'m')
%  legend('NEUTRON ABSORPTION','ALPHA','TRITON')
%  hold on
%  plot3(xc,yc,zc,'k',xc,-yc,zc,'k',xc,yc,zc+depth,'k',xc,-yc,zc+
    depth,'k')
%  plot3(xrec,yrec,zrec,'k')
%  %axis([-50 50 -50 50 0 depth+100])
%  %axis([-150 150 -150 150 0 150])
%  axis([-100 100 -100 100 0 150])
%  grid on
%  hold off
%% ANGULAR DIST
figure(4)
 subplot(121); hist(cai,10); ylabel('# OF ANGLES'); xlabel('POLAR
    (Rad.)');
 subplot(122); hist(phi,10); xlabel('AZIMUTHAL (Rad.)');
```

A.3 Charged Particle Capture with Straight Trench Geometry

This Matlab routine simulates the attenuation of neutrons through a straight wall of ^{6}LiF conversion material and generates random secondary charged-particle tracks from the location of neutron interactions. Recording the termination points of the charged-particle tracks, the counting efficiency was approximated by counting the termination points that would be found outside of the wall.

```
clear all; clc
% MATERIAL PROPERTIES
sig=54.79;  % att.length 1/mean free path
n=1e3;      % number of events
R=15;       % radius of cylinder
harea=pi*R^2; lattice=60;
```

```
uarea=lattice^2;
L1=7.51; L2=43.3; % particle ranges
depth=100;    % initial depth for ruitine
%% NEUTRON ABSORPTION EVENT
ff=exp(-depth*sig/(10^4));
z=(10^4)*log((ff)+((1-ff)*rand(1,n)))/(-sig);
clear ff
%z=(10^4)*log(1-rand(1,n))/(-sig); % importance sampling on
    exponential
% importance sampling is simply the CDF with rand in for variable
r=R*sqrt(rand(1,n)); % sample radius
theta=2*pi*rand(1,n); % sample angle
x=r.*cos(theta);          % convert to rectangular coord for
    locating in 3space
y=r.*sin(theta);
%% CHARGE PARTICLE TRACK
phi=2*pi*rand(1,n); % sampled azimuthal angle
cai=pi*(rand(1,n)); % sampled polar angle
x2=L1*sin(cai).*cos(phi)+x;
y2=L1*sin(cai).*sin(phi)+y; %clear phi
z2=L1*cos(cai)+z;  %clear cai
x3=x+L2*(x-x2)/L1;
y3=y+L2*(y-y2)/L1;
z3=z+L2*(z-z2)/L1;
%% TRACK ENDS TO POLAR COORDS
r2=sqrt(x2.*x2+y2.*y2); % polar makes easy to check if out of
    cylinder
r3=sqrt(x3.*x3+y3.*y3);
%% SORTING ARRAYS
noabs=z<depth; % neutron not absorbed in LiF zero to eliminate
nocnt=(r2>R)|(r3>R)|(z2>depth)|(z3>depth);
CR=sum(noabs.*nocnt); clear nocnt noabs
clear CR
grid on
%% CIRCLE
 xc=-15:0.1:15;
 yc=sqrt(R*R-xc.*xc);
 zc=zeros(1,numel(xc));
 xrec=[0 0  0  0];
 yrec=[R R -R -R];
 zrec=[depth 0 0 depth];
%% PLOTS FROM HERE ONWARD
figure(1)
```

```
polar(theta,r,'.')
title('INTERACTION LOCATIONS');
%% depth of int
figure(2)
hist(z,10); title('DEPTH OF INTERACTION'); % show sampled
    distribution
xlabel('DEPTH (microns)');
ylabel('# OF INTERACTIONS');
%% graphical plot
%  A=cat(1,x2,x,x3); B=cat(1,y2,y,y3); C=cat(1,z2,z,z3);
%  figure(3)
%  plot3(x,y,z,'*',x2,y2,z2,'rs',x3,y3,z3,'gd',A,B,C,'m')
%  legend('NEUTRON ABSORPTION','ALPHA','TRITON')
%  hold on
%  plot3(xc,yc,zc,'k',xc,-yc,zc,'k',xc,yc,zc+depth,'k',xc,-yc,zc+
    depth,'k')
%  plot3(xrec,yrec,zrec,'k')
%  %axis([-50 50 -50 50 0 depth+100])
%  %axis([-150 150 -150 150 0 150])
%  axis([-100 100 -100 100 0 150])
%  grid on
%  hold off
%% ANGULAR DIST
figure(4)
 subplot(121); hist(cai,10); ylabel('# OF ANGLES'); xlabel('POLAR
     (Rad.)');
 subplot(122); hist(phi,10); xlabel('AZIMUTHAL (Rad.)');
```

A.4 Charged Particle Capture with Sinusoid Trench Geometry

This Matlab routine simulates the attenuation of neutrons through a sinusoidal-shaped wall of conversion material and generates random secondary charged-particle tracks from the location of neutron interactions. Recording the termination points of the charged-particle tracks, the counting efficiency was approximated by counting the termination points that would be found outside of the wall.

```
clear all; clc
% MATERIAL PROPERTIES
```

```
sig=54.79;  % att.length 1/mean free path
n=1e3;      % number of events
R=15;       % radius of cylinder
harea=pi*R^2; lattice=60;
uarea=lattice^2;
L1=7.51; L2=43.3; % particle ranges
depth=100;    % initial depth for ruitine
%% NEUTRON ABSORPTION EVENT
ff=exp(-depth*sig/(10^4));
z=(10^4)*log((ff)+((1-ff)*rand(1,n)))/(-sig);
clear ff
%z=(10^4)*log(1-rand(1,n))/(-sig); % importance sampling on
    exponential
% importance sampling is simply the CDF with rand in for variable
r=R*sqrt(rand(1,n)); % sample radius
theta=2*pi*rand(1,n); % sample angle
x=r.*cos(theta);        % convert to rectangular coord for
    locating in 3space
y=r.*sin(theta);
%% CHARGE PARTICLE TRACK
phi=2*pi*rand(1,n); % sampled azimuthal angle
cai=pi*(rand(1,n)); % sampled polar angle
x2=L1*sin(cai).*cos(phi)+x;
y2=L1*sin(cai).*sin(phi)+y; %clear phi
z2=L1*cos(cai)+z;  %clear cai
x3=x+L2*(x-x2)/L1;
y3=y+L2*(y-y2)/L1;
z3=z+L2*(z-z2)/L1;
%% TRACK ENDS TO POLAR COORDS
r2=sqrt(x2.*x2+y2.*y2); % polar makes easy to check if out of
    cylinder
r3=sqrt(x3.*x3+y3.*y3);
%% SORTING ARRAYS
noabs=z<depth; % neutron not absorbed in LiF zero to eliminate
nocnt=(r2>R)|(r3>R)|(z2>depth)|(z3>depth);
CR=sum(noabs.*nocnt); clear nocnt noabs
clear CR
grid on
%% CIRCLE
 xc=-15:0.1:15;
 yc=sqrt(R*R-xc.*xc);
 zc=zeros(1,numel(xc));
 xrec=[0 0  0  0];
```

```
 yrec=[R R -R -R];
 zrec=[depth 0 0 depth];
%% PLOTS FROM HERE ONWARD
figure(1)
polar(theta,r,'.')
title('INTERACTION LOCATIONS');
%% depth of int
figure(2)
hist(z,10); title('DEPTH OF INTERACTION');  % show sampled
   distribution
xlabel('DEPTH (microns)');
ylabel('# OF INTERACTIONS');
%% graphical plot
%  A=cat(1,x2,x,x3); B=cat(1,y2,y,y3); C=cat(1,z2,z,z3);
%  figure(3)
%  plot3(x,y,z,'*',x2,y2,z2,'rs',x3,y3,z3,'gd',A,B,C,'m')
%  legend('NEUTRON ABSORPTION','ALPHA','TRITON')
%  hold on
%  plot3(xc,yc,zc,'k',xc,-yc,zc,'k',xc,yc,zc+depth,'k',xc,-yc,zc+
   depth,'k')
%  plot3(xrec,yrec,zrec,'k')
%  %axis([-50 50 -50 50 0 depth+100])
%  %axis([-150 150 -150 150 0 150])
%  axis([-100 100 -100 100 0 150])
%  grid on
%  hold off
%% ANGULAR DIST
figure(4)
 subplot(121); hist(cai,10); ylabel('# OF ANGLES'); xlabel('POLAR
    (Rad.)');
 subplot(122); hist(phi,10); xlabel('AZIMUTHAL (Rad.)');
```

Appendix B

Silvaco TCAD Input Files

B.1 Piercing Trench Comparison with Selective Window Design

To compare the two different configurations of perforated diode, two input files were created independently and executed to produce the electric field solutions. The data viewing software tool called Tonyplot was used to plot both solutions in one graph with a similar and shared color map. The input file for the piercing model is given below.

```
go atlas

mesh
x loc=0 spac=1
x loc=10 spac=0.1
x loc=20 spac=1

y loc=0 spac=0.1
y loc=50 spac=1
y loc=100 spac=1


region num=1 x.min=0 x.max=20 y.min=50 y.max=100 material=silicon
region num=1 x.min=10 x.max=20 y.min=0 y.max=50 material=silicon
region num=2 x.min=0 x.max=10 y.min=0 y.max=50 material=oxide

electrode top name=anode x.min=16 x.max=20
electrode bottom name=cathode
```

```
contact all neutral

material taun0=1e-4 taup0=1e-4 region=1

#interface x.min=0 x.max=12 y.min=0 y.max=52 qf=-1e10 s.n=1e2 s.p
   =1e2

doping uniform region=1 resistivity=12000 n.type
doping gaussian conc=1e19 char=1 p.type peak=0.1

#save outfile=piercinggeo.str
#tonyplot piercinggeo.str

models consrh conmob bgn kla auger fldmob bbt.std
#impact crowell

method newton autonr carriers=2 climit=1e-3

solve init

save outfile=piercinginit.str
tonyplot piercinginit.st

solve vanode=0 vcathode=0 vstep=-1 vfinal=-5 name=anode

save outfile=piercing5.str
tonyplot piercing5.str
quit
```

The second input file responsible for building the selective window geometry and simulation is given below.

```
go atlas

mesh
x loc=0 spac=1
x loc=10 spac=0.1
x loc=20 spac=1

y loc=0 spac=0.1
y loc=50 spac=1
y loc=100 spac=1
```

```
region num=1 x.min=0 x.max=20 y.min=50 y.max=100 material=silicon
region num=1 x.min=10 x.max=20 y.min=0 y.max=50 material=silicon
region num=2 x.min=0 x.max=10 y.min=0 y.max=50 material=oxide

electrode top name=anode x.min=16 x.max=20
electrode bottom name=cathode

contact all neutral

material taun0=1e-4 taup0=1e-4 region=1

#interface x.min=0 x.max=12 y.min=0 y.max=52 qf=-1e10 s.n=1e2 s.p
   =1e2

doping uniform region=1 resistivity=12000 n.type
doping gaussian conc=1e19 char=1 ratio.lat=1 p.type x.left=16 x.
   right=20 peak=0.1

save outfile=selectivegeo.str
tonyplot selectivegeo.str

models consrh conmob bgn kla auger fldmob bbt.std
#impact crowell

method newton autonr carriers=2 climit=1e-3

solve init

save outfile=selectiveinit.str
tonyplot selectiveinit.st

solve vanode=0 vcathode=0 vstep=-1 vfinal=-5 name=anode

save outfile=selective5.str
tonyplot selective5.str
quit
```

B.2 In-Hole Diffusion Comparison with In-Hole Oxidation

A new input file was created with the in-hole diffusion geometry. This involved defining boron diffusion profiles along the trench walls. The potential field results of this model were simply compared to similar solutions with the selective window design that was already simulated B.1.

```
go atlas

mesh

x loc=0 spac=4
x loc=15 spac=0.5
x loc=30 spac=4
x loc=45 spac=0.5
x loc=60 spac=4
x loc=75 spac=0.5
x loc=90 spac=4
x loc=105 spac=0.5
x loc=120 spac=4

y loc=0 spac=0.5
y loc=15 spac=6
y loc=85 spac=6
y loc=100 spac=0.5
y loc=115 spac=6
y loc=200 spac=10
y loc=285 spac=6
y loc=300 spac=1

region num=1 material=silicon x.min=0 x.max=120 y.min=0 y.max=300
region num=2 material=oxide x.min=15 x.max=45 y.min=0 y.max=100
region num=2 material=oxide x.min=75 x.max=105 y.min=0 y.max=100

electrode num=1 name=anode top x.min=55 x.max=65
electrode num=2 name=cathode bottom

contact all neutral

material taun0=1e-4 taup0=1e-4 region=1
```

```
doping region=1 uniform phosphorus conc=1e12

doping gaussian boron conc=1e19 char=1 ratio.lat=0 peak=0 x.min=0
   x.max=15
doping gaussian boron conc=1e19 char=1 ratio.lat=1 peak=100 x.min
   =15 x.max=45
doping gaussian boron conc=1e19 char=1 ratio.lat=0 peak=0 x.min=45
    x.max=75
doping gaussian boron conc=1e19 char=1 ratio.lat=1 peak=100 x.min
   =75 x.max=105
doping gaussian boron conc=1e19 char=1 ratio.lat=0 peak=0 x.min
   =105 x.max=120

doping gaussian dir=x boron conc=1e19 char=1 y.min=0 y.max=100 x.
   min=15 x.max=15
doping gaussian dir=x boron conc=1e19 char=1 y.min=0 y.max=100 x.
   min=75 x.max=75
doping gaussian dir=x boron conc=1e19 char=1 y.min=0 y.max=100 x.
   min=45 x.max=45
doping gaussian dir=x boron conc=1e19 char=1 y.min=0 y.max=100 x.
   min=105 x.max=105

#save outfile=IHDgeo.str
#tonyplot IHDgeo.str
#quit

models consrh conmob bgn kla auger fldmob bbt.std

method newton autonr carriers=2 climit=1e-3

solve init
solve prev

save outfile=IHDinit.str
tonyplot IHDinit.str

solve vanode=0 vcathode=0 vstep=0.5 vfinal=5 name=cathode
save outfile=IHD5.str
tonyplot IHD5.str
```

B.3 In-Hole Diffusion Signal Response with Trench Depth

Simulating the pulse for three different trench depths required three different input files. For simplicity, I will simply insert a single input file. The only difference in the other files was the definition of the trench depth and meshing to accomodate the location of the bottom of the trench surface.

```
go atlas

mesh three.d

x loc=0 spac=2
x loc=15 spac=0.3
x loc=30 spac=2
x loc=45 spac=0.3
x loc=60 spac=2

y loc=0 spac=0.3
y loc=30 spac=4
y loc=135 spac=6
y loc=220 spac=4
y loc=250 spac=0.3
y loc=280 spac=4
y loc=300 spac=6
y loc=330 spac=4
y loc=350 spac=1

z loc=0 spac=4
z loc=60 spac=4

region num=1 material=silicon x.min=0 x.max=120 y.min=0 y.max=350
   z.min=0 z.max=60
region num=2 material=oxide x.min=0 x.max=15 y.min=0 y.max=250 z.
   min=0 z.max=60
region num=2 material=oxide x.min=45 x.max=60 y.min=0 y.max=250 z.
   min=0 z.max=60

electrode num=1 name=anode top x.min=20 x.max=40 z.min=0 z.max=60
electrode num=2 name=cathode bottom
```

```
contact all neutral

material taun0=1e-4 taup0=1e-4 region=1

doping region=1 uniform phosphorus resist=10000

doping gaussian boron conc=1e19 char=0.5 ratio.lat=0.1 peak=0 x.
   min=15 x.max=45 z.min=0 z.max=60
doping region=1 gaussian boron conc=1e19 char=0.5 ratio.lat=1 x.
   min=0 x.max=15 y.min=0 y.max=250 z.min=0 z.max=60
doping region=1 gaussian boron conc=1e19 char=0.5 ratio.lat=1 x.
   min=45 x.max=60 y.min=0 y.max=250 z.min=0 z.max=60

#doping gaussian phosp conc=1e21 char=0.5 peak=300

save outfile=PRF250geo.str
#tonyplot3d PRF250geo.str


models consrh conmob bgn kla auger fldmob bbt.std

method newton autonr carriers=2 climit=1e-3

solve init
solve prev

save outfile=PRF250init.str
#tonyplot PRF250init.str


log outfile=PRF250.log
solve vanode=0 vcathode=0 vstep=0.1 vfinal=2 name=cathode
save outfile=PRF250v2.str

solve vanode=0 vcathode=2 vstep=0.2 vfinal=5 name=cathode
save outfile=PRF250v5.str
tonyplot3d PRF250v5.str

solve vanode=0 vcathode=5 vstep=0.2 vfinal=10 name=cathode
save outfile=PRF250v10.str
tonyplot3d PRF250v10.str

solve vanode=0 vcathode=10 vstep=0.2 vfinal=20 name=cathode
```

```
save outfile=PRF250v20.str
tonyplot3d PRF250v20.str

tonyplot PRF250.log

method halfimpl dt.min=5e-10
log outf=PRF250seu.log
solve tfinal=1e-8 tstep=2e-9
singleeventupset entry="22,42,22." exit="28,48,28" radius=5
   density=1e13
method halfimpl dt.min=5e-10
save outfile=PRF250seu.str
solve tfinal=1e-5 tstep=1e-7 outf=t.str
tonyplot PRF250seu.log


quit
```